INVESTIGATION OF ACTIVATION PRODUCTS IN MEDICAL LINEAR ACCELERATORS

By

Mohammed Khalil Saeed

A Dissertation Submitted to the School of Physics and Applied Physics
of the Faculty of Science, College of Graduate Studies, University of El-Neelain,
in fulfillment of the Requirements for the Degree

DOCTOR OF PHILOSOPHY
IN MEDICAL PHYSICS

KHARTOUM, SUDAN
JUNE 2009

University of El-Neelain

DEPARTMENT OF MEDICAL PHYSICS

The undersigned hereby certify that they have read and recommend to the Faculty of Graduate Studies for acceptance a thesis entitled "**Investigation of activation products in medical linear accelerators**" by **Mohammed Khalil Saeed** in fulfillment of the requirements for the degree of **Doctor of Philosophy in Medical Physics**.

Dated: June 2009

External Examiner: _____

Dr. Farouk Habbani

Research Supervisors: _____

Dr. Osman Moustafa

_____

Dr. Osama Ali Yasin

_____

Dr. Claudio Tuniz

Internal Examiner: _____

Dr Hassan H Hussien

University of El-Neelain

Date: **June 2009**

Author: **Mohammed Khalil Saeed**

Title: **Investigation of activation products in medical linear accelerators**

Department: **Medical Physics**

Degree: **Ph.D.** Year: **2009**

Permission is herewith granted to University of El-Neelain to circulate and to have copied for non-commercial purposes, at its discretion, the above title upon the request of individuals or institutions.

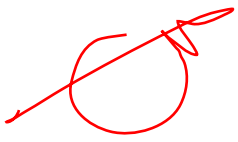

Signature of Author

I hereby dedicate this scientific research to very special people in my life as following: my father Mr. Khalil Saeed who played a pivotal role in opening new horizons for my career in medical physics, my mother, my wife and my son Mumen. I would like to dedicate this to my promoter Dr. Osman Moustafa who has greatly helped me in conducting this research successfully and to Prof. C. Tuniz.

Table of Contents

List of Tables

List of Figures

Abstract

Study of induced activity in a medical linear accelerator room was carried out on Clinac 2100C running 15 MV at Maggiore Hospital, Trieste, Italy. Mathematical model to calculate the induced dose rate has been derived and compared to measurements results. Both of experimental method and mathematical model present a good agreement. The experimental method was performed using filter papers and portable spectroscopy. The activation level reached its practical saturation value after a 30 min continuous irradiation, corresponding to 12000 MU at a dose rate of 240 MU/min. The filter paper method was first time used for the purpose of this measurement. Typical radionuclides produced in the treatment room were identified. The results obtained by this new method, consisting of filter paper, can represent a reliable tool. Moreover, the measurements uncertainty using portable spectrometer was decreased and determined to be 6.02%. In addition, the Clinac 2100C has been simulated with Monte Carlo code Geant4 and the neutron fluence, as a function of the neutron energy, has been calculated in the isocenter and outside the treatment room to estimate the equivalent dose to technologist and patients. The ambient dose equivalent for patient and radiotherapy technologist has been reported in this study using the above mentioned methods. The derived data using different field sizes have been used to evaluate the ambient dose equivalent from neutrons to a patient receiving radiation treatment. The maximum of annual ambient dose equivalent present for 15 MV photon beam is about 1.96 mSv for the technologists, in addition to 1.032 $mSv/year$ received by them in the control room. The maximum of ambient dose equivalent received by patients for minimum field size present 1.79 mSv/Gy for 20 MV photon beam. These values represent neglected doses for technologists, but at same time cannot be ignored for patients, where they can represent a risk for healthy tissues and contribute to secondary malignancy insurgence.

الخلاصة

تمت دراسة النشاط الاشعاعي المحرض في الغرفة العلاجية لجهاز المعجل الخطي C 2100 الذي يولد طاقة بمقدار 15 MV في مستشفي ماجوريا بمدينة تريستا بايطاليا. كما تم استخدام نموذج رياضي لحساب معدل الجرعة المحرض و مقارنتة مع النتائج المقاسة. اغلب النتائج التجريبية اظهرت تطابق جيد مع النموذج الرياضي. تم تنفيذ هذه القياسات باستخدام ورق ترشيح و جهاز قياس الطيف المحمول. ان مستوي النشاط الاشعاعي يصل الي مستوي التشبع بعد 30 دقيقة من التشعيع المتواصل و هذا يعادل 12000 MU باستخدام معدل جرعة 240 MU/min. ان طريقة ورق الترشيح تعتبر طريقة جديدة بغرض تنفيذ هذه القياسات. كما تم تحديد الاهوية المشعة داخل غرفة العلاج، حيث ان طريقة القياس الجديدة هذه، التي تتضمن ورق الترشيح، تمثل طريقة فعالة يمكن الاعتماد عليها. فضلا علي ذلك، ان نسبة عدم دقة القياسات بواسطة استخدام جهاز مقياس الطيف المحمول تعادل 6.02%. بالاضافة تم استخدام طريقة مونتي كارلو بمحاكات جهاز المعجل الخطي 2100 C بواسطة استخدام الكود جنت ٤ و تم حساب تدفق النيوترونات كدالة في طاقة النيوترون وذالك في نقطة التساوي المركزية للجهاز و خارج الغرفة و ذلك لتقدير الجرعة المكافئة للمرضي و التقنيين. تم تدويين نتائج الجرعة المكافئة للمرضي و تقني العلاج بالاشعة في هذه الدراسة باستخدام الوسائل و الطرق المذكورة اعلاه. تم تقييم الجرعة المكافئة القصوي بواسطة استخدام البيانات المشتقة لاحجام حقول مختلفة من النيوترونات الناتجة للمريض الذي يتلقي علاجا اشعاعيا. ان الجرعة المكافئة القصوي السنوية التي تصل الي تقني العلاج بالاشعة بواسطة استخدام حقل فوتوني بطاقة 15 MV تمثل 1.96 mSv بالاضافة الي 1.032 mSv/year كجرعة مضافة ناتجة عن تعرض التقنيين في غرفة التحكم و المراقبة. كما ان الجرعة المكافئة القصوي التي تصل الي المريض المعالج بواسطة ادني حجم حقل بطاقة 20 MV تمثل 1.79 mSv/year . تعتبر هذه القيم غير عالية لتقني العلاج بالاشعة و لكن في نفس الوقت لا يمكن اهمالها بالنسبة للمرضي، حيث يمكن ان تسبب خطراصابة الانسجة السليمة و المساهمة في اصابات ثانوية خبيثة.

Acknowledgements

This work was supported in part by United Nation Education, Scientific and Cultural Organization "UNESCO". Acknowledgment is made to Abdus Salam International Center for Theoretical Physics "ICTP", Trieste, Italy.

In promoting this research, I have been greatly helped by my supervisor Dr. Osman Moustafa and my co-supervisor Dr Osama Yasin. I wish to thank them for reviewing the research in its various stages of advancement. My great appreciation goes to Prof. C. Tuniz the assistance director of ICTP for devoting his time and effort in numerous discussions and invaluable guidance, resulting in the crystallization of this study.

I would like to thank all of my colleagues for advice and encouragement throughout this research.

I would like to express my gratitude to Dr. Rossella Vidimari and Dr. Maria Rosa Fornasier from Maggiore Hospital who provided me with necessary equipments for this research.

Acknowledgment is made to the head of the Medical Physics Department at Maggiore Hospital, Prof. Dr. Fabio De Guarrini for his encouragement and allowing me ample time to conduct this study.

I hereby wish to express my deepest gratitude to my wife, Amel, for sacrificing her time and invaluable encouragement that made this study worth while.

Khartoum, Sudan — Mohammed Khalil Saeed
June, 2009

Chapter 1

Introduction

In the 1930s, in accelerator production, scientists began to build machines which have a high degree of control. The earliest accelerators were simple vacuum tubes in which electrons were accelerated by the voltage difference between two oppositely charged electrodes [1]. Accelerators today are used not only for basic research purposes, but also for many other applications such as medical applications and this type of linear accelerators are the medical linear accelerators.

All medical accelerators that produce energies above 10 MeV can produce radioactivity. The process by which materials become radioactive is commonly referred to as "radioactivation" or simply "activation". All materials located within an accelerator enclosure have the potential to be radioactivated if subjected to primary or secondary beams. Materials that may become radioactive include any material within the accelerator enclosure, Beamline components, Air, and Cooling liquids.

Beamline components may become radioactive depending on nature of the material, proximity to the beam, and beam characteristics. Items that intercept a portion of the beam are most likely to be activated and contaminated. Among those items that have the highest probability for activation are targets, beam dumps or stops,

collimators, magnets, filters and cavities.

Air, dust, and other gases in the accelerator enclosure may be activated. Typically, the activation products are short-lived gaseous radionuclides of the elements in the air or particulary, in the case of dust particles.

The production of radioactivity can result by different types of nuclear reactions such as exothermic nuclear reactions and giant-resonance photonuclear reactions. These mechanisms have been described in details by Barbier [2] and IAEA protocol [3] and summarized by Swanson and Thomas [4].

The objectives of this research are summarized as follows:

∗ Investigate radioactive and toxic gas production in medical linear accelerators. The investigation of activation products include target, beam dumps, collimators, magnets, cavities and flattening filter.

∗ Estimate dose and induced radioactivity in the patient body.

∗ Comparison of activations for difference types of accelerators for energies less than 30 MeV.

∗ Study the theory of Cohen [5], who states that the target thickness exceeds the range of the incident ions and that the irradiation period greatly exceeds the half-life of the radionuclide of interest.

The largest cause of the radiation exposure incurred by accelerator workers arises from operations on and maintenance of radioactive components, handling and moving the activated items. An important aim of this research was the protection for workers to ensure that the staff are not unduly exposed when maintaining accelerator components and to control the dispersion of radioactive materials, in addition to the protection of patients.

Chapter 2

Fundamental principles

2.1 Radioactive transformation

Radioactive transformation of unstable nuclei is a major focus of the profession of radiation protection. The process of radioactive transformation was recognized by Rutherford as transmutation of one element to another. It is also quit common to use the term radioactive decay, but transformation is a more accurate description of what actually happens, decay suggests a process of disappearance, when what actually happens is that an atom with excess energy transforms itself to another atom that is either stable or one with more favorable conditions to proceed on to stability [15].

Atoms undergo radioactive transformation because constituents of the nucleus are not arrayed in the lowest potential energy states possible, therefore, rearrangement of the nucleus occurs in such a way that this excess energy is emitted and the nucleus is transformed to an atom of a new element. The transformation of a nucleus may involve the emission of alpha particles, negatron, positron, electromagnetic radiation in the form of x or gamma rays, and to a lesser extends neutron, proton, and fission fragments. Such transformation are spontaneous, and the Q-values are positive, if

the array of nuclear constituents is in the lowest potential energy states possible, the transformation yields a stable atom, if not, another transformation must occur.

2.1.1 Decay constant

The activity of a radioactive source is proportional to the number of radioactive atoms present, therefore, it can be written mathematically as a differential change in N in a differential unit of time as

$$Activity = |-\frac{dN}{dt}| = \lambda N \tag{2.1}$$

where the constant of proportionality ,λ, is the disintegration constant, and $-dN/dt$ is the rate of decrease of the number ,N, of radioactive atoms at any time ,t,. Rearranging the equation gives an expression that can be integrated directly between the limits N_0 at $t = 0$ and $N(t)$, the number of atoms for any other time t:

$$\int_{N_0}^{N(t)} \frac{dN}{N} = -\lambda \int_0^t dt$$

Integration and evaluation of the limits yields

$$\ln N(t) - \ln N_0 = -\lambda t$$

or

$$\ln N(t) = \ln N_0 - \lambda t$$

which is an equation of a straight line with slope of $-\lambda$ and a y-intercept of $\ln N_0$. By applying the logarithms law, this can also be written as follows:

$$\ln \frac{N(t)}{N_0} = -\lambda t$$

and since the logarithm of a number is the exponent to which the base (in this case e) is raised to obtain the number, the expression above is literally

$$\frac{N(t)}{N_0} = e^{-\lambda t}$$

or

$$N(t) = N_0 e^{-\lambda t} \tag{2.2}$$

If both sides are multiplied by λ, and recalling that activity = λN, then

$$A(t) = A_0 e^{-\lambda t} \tag{2.3}$$

In other words, the activity $A(t)$, at some time t, of a source of radioactive atoms, all of the same species with the disintegration constant λ, is equal to the initial activity A_0, multiplied by the exponential $e^{-\lambda t}$, where e is the base of the natural logarithm.

2.1.2 The half-life and the mean life

The half-life (or half-period) of radioactive substance is used to describe the exponential behavior of radioactive transformation since it is more meaningful than the disintegration constant with reciprocal units of time. The half-life is the amount of time it takes for half of the atoms in a radioactive source to undergo transformation, this special value of time, $t_{1/2}$, is calculated as the value of t that corresponds to $A(t)/A_0 = \frac{1}{2}$ as following [15]:

$$\frac{A(t)}{A_0} = \frac{1}{2} = e^{-\lambda t_{1/2}} \tag{2.4}$$

which can be solved by taking the natural logarithm of both sides, or

$$\ln 1 - \ln 2 = -\lambda T_{1/2}$$

such that

$$t_{1/2} = \frac{\ln 2}{\lambda} \tag{2.5}$$

The disintegration constant λ, which is required for calculating activity, follows directly from this relationship as

$$\lambda = \frac{\ln 2}{t_{1/2}}$$

The mean-life of each atom in a radioactive source can be useful for determining the total number of emission of radiation from the source. The mean life is the average time it takes each atom to transmute, recognizing that some will transmute right away, some will last an infinite time, and others will have lifetimes in between. The mean life, τ, of the atoms in a particular radioisotope is, therefore,

$$\tau = \frac{t_{1/2}}{\ln 2} \tag{2.6}$$

2.1.3 Series decay calculation

The number of atoms of each member of a radioactive series at any time ,t, can be obtained by solving a system of differential equations that relates each product, $N_1, N_2, N_3, \ldots, N_i$ with corresponding disintegration constants $\lambda_1, \lambda_2, \lambda_3, \ldots, \lambda_i$. Each series begins with a parent nuclide, N_1, which has a rate of transformation

$$\frac{dN_1}{dt} = -\lambda_1 N_1 \tag{2.7}$$

The second nuclide in radionuclide series will be produced at a rate of $\lambda_1 N_1$ due to the transformation of N_1, but as soon as atoms of N_2 exit, they too can undergo transformation if they are radioactive, thus the rate of change of atoms of N_2 is the rate of production minus the rate of removal of N_2 atoms, or

$$\frac{dN_2}{dt} = \lambda_1 N_1 - \lambda_2 N_2 \tag{2.8}$$

Similarly, for atoms of N_3, which are produced by transformation of N_2 atoms and subject to removable as a function of the disintegration constant λ_3,

$$\frac{dN_3}{dt} = \lambda_2 N_2 - \lambda_3 N_3 \tag{2.9}$$

and so on, up to the member of the series,

$$\frac{dN_i}{dt} = \lambda_{i-1} N_{i-1} - \lambda_i N_i \tag{2.10}$$

If the end product is stable, the atoms of the stable end product appear at the rate of the last radioactive precursor, and of course are not removed since they are stable. The number of atoms of N_1 is

$$N_1(t) = N_1^0 e^{-\lambda_1 t} \tag{2.11}$$

where N_1^0 is the number of atoms of the parent at $t = 0$. This expression for N_1 can be inserted into the equation for dN_2/dt to give

$$\frac{dN_2(t)}{dt} = \lambda_1 N_1^0 e^{-\lambda_1 t} - \lambda_2 N_2 \tag{2.12}$$

Collecting terms, we have

$$\frac{dN_2}{dt} + \lambda_2 N_2 = \lambda_1 N_1^0 e^{-\lambda_1 t} \tag{2.13}$$

This type of equation can be converted into one that can be integrated directly by multiplying through by an appropriate integrating factor, which for this form is always an exponential with an exponent that is equal to the constant in the second term multiplied by the variable in the denominator of the derivative, or in this case $e^{\lambda_2 t}$, thus

$$e^{\lambda_2 t}\frac{dN_2}{dt} + e^{\lambda_2 t}\lambda_2 N_2 = \lambda_1 N_1^0 e^{(\lambda_2 - \lambda_1)t} \tag{2.14}$$

Multiplying through by $e^{\lambda_2 t}$ converts the left side of the equation to the time derivative of $N_2 e^{\lambda_2 t}$, which can be demonstrated by differentiating the expression. It also yields an exponential expression multiplied by a constant on the right side, or

$$\frac{d}{dt}(N_2 e^{\lambda_2 t}) = \lambda_1 N_1^0 e^{(\lambda_2 - \lambda_1)t} \tag{2.15}$$

which can be integrated directly to give

$$N_2 e^{\lambda_2 t} = \frac{\lambda_1}{\lambda_2 - \lambda_1} N_1^0 e^{(\lambda_2 - \lambda_1)t} + C \tag{2.16}$$

where C, the constant of integration, is determined by stating the condition that when $t = 0, N_2 = 0$, thus

$$C = -\frac{\lambda_1}{\lambda_2 - \lambda_1} N_1^0 \tag{2.17}$$

Therefore, the solution for N_2 as a function of time is

$$N_2 = \frac{\lambda_1}{\lambda_2 - \lambda_1} N_1^0 (e^{-\lambda_1 t} - e^{-\lambda_2 t}) \tag{2.18}$$

The number of atoms of the third kind is found by inserting this expression for N_2 into the equation for the rate of change of N_3, which as before is the rate of production of N_3 by transformation of atoms of N_2 (or $\lambda_2 N_2$) minus the rate of removal of N_3 by radioactive transformation (or $\lambda_3 N_3$).

$$\frac{dN_3}{dt} = \lambda_2 N_2 - \lambda_3 N_3$$

After the integration is performed and the constant of integration is evaluated, the equation for the number of atoms of N_3 with time is

$$N_3(t) = \lambda_1 \lambda_2 N_1^0 [\frac{e^{-\lambda_1 t}}{(\lambda_2 - \lambda_1)(\lambda_3 - \lambda_1)} + \frac{e^{-\lambda_2 t}}{(\lambda_1 - \lambda_2)(\lambda_3 - \lambda_2)} + \frac{e^{-\lambda_3 t}}{(\lambda_1 - \lambda_3)(\lambda_2 - \lambda_3)}] \tag{2.19}$$

In similar fashion, for the number of atoms of the fourth kind, the expression for $N_3(t)$ is inserted into the equation for dN_4/dt, which is integrated to obtain the number of atoms of N_4 with time, or

$$N_4(t) = \lambda_1\lambda_2\lambda_3 N_1^0[\frac{e^{-\lambda_1 t}}{(\lambda_2-\lambda_1)(\lambda_3-\lambda_1)(\lambda_4-\lambda_1)} + \frac{e^{-\lambda_2 t}}{(\lambda_1-\lambda_2)(\lambda_3-\lambda_2)(\lambda_3-\lambda_2)} + \frac{e^{-\lambda_3 t}}{(\lambda_1-\lambda_3)(\lambda_2-\lambda_3)(\lambda_4-\lambda_3)} + \frac{e^{-\lambda_4 t}}{(\lambda_1-\lambda_4)(\lambda_2-\lambda_4)(\lambda_3-\lambda_4)}] \quad (2.20)$$

These equations yield the number of atoms of each of the first four members of a radioactive series that begins with a pure radioactive parent (i.e., there are no transformation products at $t = 0$).

A radioactive series typically ends at a stable nuclide or one with a very large half-life such that it is not unreasonable to terminate the production of radioactive atoms [15].

2.1.4 Methods of determination half-lives

The measurements of one short - half live radionuclide can be measured directly using basic nuclear counting, the presence of two or three radionuclides with different half-lives presents quite a masking effect.

Using conventional counting and taking a series of activity measurements over several time intervals and plotting the data can determine the half-life of an unknown radioactive substance. If the data are plotted as ln $A(t)$ versus t and a straight

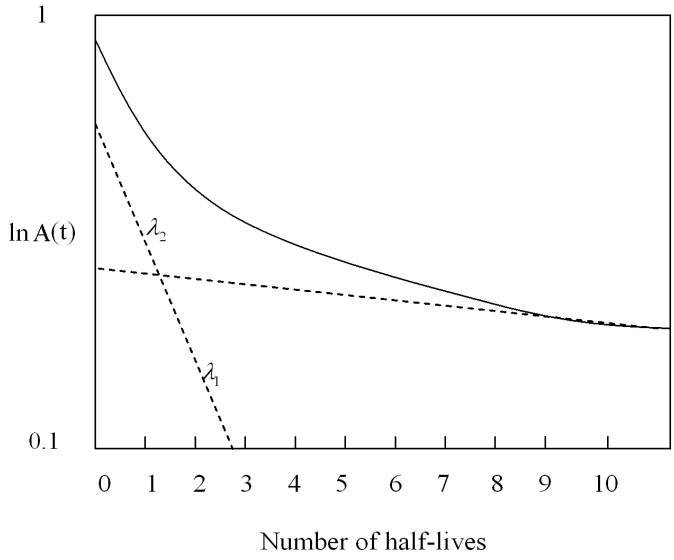

Figure 2.1: The ln $A(t)$ plotted as a function of time for two radionuclides with two different half-lives.

line is obtained, we can be reasonably certain that the source contains only one radioisotope. The slop of the straight line provides the disintegration constant, and once disintegration constant is known, the half-life can be determined directly.

This technique can also applicable to a source that contains more than one radionuclide with different half-lives. This can be readily be determined by plotting the ln $A(t)$ of a series of activity measurements with time as shown in Fig 2.1 for two radio nuclides. If only one radionuclide were present, the semilog plot would be a straight line, however, when two or more are present, the line will be curved as in Fig 1.1. The straight-line portion at the far end represent the longer-lived component, and thus can be extrapolated back to time zero and subtracted from the total curve to yield a second straight line. The slopes of these two lines establish the disintegration

constant, λ_1 and λ_2 , from which the half-life of each can be calculated for possible identification of the two radionuclides in the source.

2.1.5 Modes of radioactive decay

The possible modes of radioactive decay summarized as follows: α, β^-, β^+, electron capture, γ, and internal conversion.

Alpha particles are emitted from unstable nuclei and structurally equivalent to the nucleus of a helium atom, consists of two protons and two neutrons. It is emitted as a decay product of many radionuclides predominantly of atomic number greater than 82. This mode of decay yield by the following equation:

$$ {}^{A}_{Z}X \longrightarrow {}^{A-4}_{Z-2}Y + {}^{4}_{2}He(\alpha) \tag{2.21} $$

where X is the radioactive parent, Z is atomic number, A is atomic mass number and Y is the daughter decayed from parent.

Negative beta particle β^- or negatron is an electron emitted from the nucleus of a decaying radionuclide. This decay yield by the following equation:

$$ {}^{A}_{Z}X \longrightarrow {}^{A}_{Z+1}Y + \beta^- + \bar{\nu}_e \tag{2.22} $$

where $\bar{\nu}_e$ is antineutrino which is a particle of zero charge, accompanies beta-particle emission.

Positrons consist of positively charged electrons (positive beta particles, β^+), and emitted from nuclei having neutron/proton ratios too small for stability, that is, those which have an excess of protons. Positive beta decay yield by the following equation:

$$ {}^{A}_{Z}X \longrightarrow {}^{A}_{Z-1}Y + \beta^+ + \nu_e \tag{2.23} $$

Another mode of radioactive decay is via mechanism by which an unstable nucleus can increase its neutron/proton ratio via the capture by the nucleus of a proximate atomic electron. This decay process is known as electron capture (EC), or sometimes referred to as K capture, because most of the electrons are captured from the K shell. This decay occur using the following equation:

$$ {}^{A}_{Z}X + e^{-}_{K} \longrightarrow {}^{A}_{Z-1}\,Y + \nu_e \tag{2.24} $$

The capture of an atomic electron by the nucleus leaves a vacancy in an electron shell, and this is usually filled by an electron from an outer shell, resulting in the production of characteristic photons or Auger electrons.

Gamma radiation it is emitted from excited nucleus ${}^{A}_{Z}X^{*}$ only when the daughter nuclide is left at an unstable elevated energy state. Gamma decay occur by the following equation:

$$ {}^{A}_{Z}X^{*} \longrightarrow {}^{A}_{Z}\,X + \gamma \tag{2.25} $$

Decay by internal conversion results in the emission of an atomic electron. This electron, called the internal conversion electron, is emitted from an atom after absorbing the excited energy of a nucleus. Internal conversion occur by the following equation:

$$ {}^{A}_{Z}X^{*} \longrightarrow {}^{A}_{Z}\,X + e^{-}_{K} \tag{2.26} $$

2.2 Nuclear reactions

Atypical nuclear reaction is written as follows:

$$A + a \longrightarrow B + b \quad or \quad A(a,b)B,$$

where A is accelerated projectile, a is the target and B and b are the reaction products.

Usually, B will be a heavy product that stops in the target and is not directly observed, while b is a light particle that can be detected and measured. The projectile undergoes one of three possible interactions: (i) elastic scattering - no energy transfer occurs, however, the projectile changes trajectory; (ii) inelastic scattering - the projectile enters the nucleus and is re-emitted with less energy and in a different direction; and (iii) nuclear reaction - the projectile a enters the nucleus A which is transformed into nucleus B and a different particle b is emitted.

Threshold energy for a nuclear reaction is defined as the smallest value of projectile's kinetic energy at which a nuclear reaction can take place. The threshold kinetic energy of projectile a is derived from relativistic conservation of energy and momentum as:

$$KE_{thr}(a) = \frac{(m_B c^2 + m_b c^2)^2 - (m_A c^2 + m_a c^2)^2}{2\ m_A c^2} \tag{2.27}$$

with m_B, m_A, m_a and m_b the rest masses of the target A, projectile a, and products B and b , respectively [16].

2.2.1 Photonuclear reaction (γ, n)

Many nuclides undergo photonuclear reactions emit neutrons upon irradiation with gamma or x-radiation; however, most elements require high-energy electromagnetic radiation in the range 1019 MeV. The gamma or x-ray energy threshold for the production of neutrons is of the order of 10 MeV [16].

While photonuclear reactions do not play an active role in photon attenuation considerations, they are of concern in high-energy radiotherapy treatment rooms because of the neutron production through the (γ, n) reactions and because of the radioactivity that is induced in the treatment room air and in machine components through the (γ, n) reaction. Both the neutrons and the radioactivity present a health hazard to personnel and must be dealt with in treatment room and treatment machine design. The neutron problem is handled with special treatment room doors incorporating borated hydrogenous materials to thermalize and absorb the neutrons; the radioactivity with adequate room ventilation (6 to 8 air changes per hour) and use of machine components with low reaction cross-section and short half-life of the reaction product [16].

The photonuclear reactions reaction expressed by the following equation:

$$X + {}^{A}_{Z}T = n + {}^{A-1}_{Z}D \tag{2.28}$$

where ${}^{A}_{Z}T$ is the target nuclide with atomic number Z and atomic mass number A; D is the daughter nuclide with the same Z as the target, but an atomic mass number equal to $A-1$ for photodisintegration; X is the x-ray photon with an energy sufficiently high to induce photodisintegration; and n is the neutron produced through photodisintegration by high-energy x-ray photons or electrons.

In the photodisintegration of the target nuclide ${}^{A}_{Z}T$ producing a neutron and daughter nuclide, the resulting ${}^{A-1}_{Z}D$ may be radioactive and may subsequently decay through β^+ and γ decay. Not all residual daughter nuclei will be radioactive after photodisintegration.

2.2.2 Giant Photonuclear Resonance

Approximately at 30 MeV the production mechanism of neutron is known as the giant photonuclear resonance. IAEA (TRS-188) [3] has given a detailed description of this process that is summarized here. A simple picture of this phenomenon is that the electric field of the photon produced by bremsstrahlung transfers its energy to the nucleus by inducing an oscillation in which the protons as a group move oppositely to the neutrons as a group. This process has a broad maximum cross section at photon energies, k_0, between about 20-23 MeV for light nuclei for materials having mass numbers A less than about 40. For heavier targets, the peak is at an energy of approximately $k_0 = 80A^{-1/3}$ MeV. Schopper *et al* [41] have provided a great deal of data on the relevant cross sections. It turns out that the yield, Y, of giant resonance neutrons at energies above approximately $2k_0$ is nearly independent of energy and nearly proportional to the beam power.

This process may be thought of as one in which the target nucleus is excited by the electron and then decays somewhat later by means of neutron emission. It is a (γ, n) nuclear reaction, written in the scheme of notation in which the first symbol in the parentheses represents the incoming particle in a reaction while the second represents the outgoing particle. In this process the directionality of the incident electron or photon is lost so that these emissions are isotropic. Because of this isotropicity, the

inverse square law may be used to estimate the flux density at any given distance r.

2.2.3 Neutron Capture

The neutron capture reaction expressed by the following equation:

$$n + {}^{A}_{Z}T = {}^{A+1}_{Z}D + \gamma \tag{2.29}$$

where ${}^{A}_{Z}T$ is the target nuclide with atomic number Z and atomic mass number A; D is the daughter nuclide with the same Z as the target, but an atomic mass number equal to $A+1$ for neutron capture; and n is the neutron with energy sufficiently high to induce neutron capture; and γ is emitted gamma ray.

${}^{A+1}_{Z}D$ may be radioactive and may subsequently decay through β_- and γ decay. Not all residual daughter nuclei will be radioactive after neutron capture.

2.2.4 Quasi - Deuteron Neutrons

At energies above the giant resonance, the dominant neutron production mechanism is one in which the photon interacts with a neutron-proton pair within the nucleus rather than with the whole nucleus. The quasi-deuteron effect is so-named because for $E_0 \approx 30$ MeV the photon wavelength is near resonance with the average inter-nucleon distance so that the photon interactions tend to occur with "pairs" of nucleons. Only neutron-proton pairs have a nonzero electric dipole moment, which makes interactions of photons with such pairs (pseudo-deuterons) favorable. This mechanism is important for $30 < E_0 < 300$ MeV and has been described by Swanson [42].

2.3 Secular equilibrium

The phenomenon of radioisotope decay equilibrium was first observed by Ernest Rutherford and Frederick Soddy in 1902, which they reported in their classic paper on *The Cause and Nature of Radioactivity*. They reported their observations as follows:

Radioactivity is shown to be accompanied by chemical changes in which new types of matter are being continuously produced. These reaction products are at first radioactive, the activity diminishing regularly from the moment of formation. Their continuous production maintains the radioactivity of the matter producing them at a definite equilibrium value.

Secular equilibrium is a steady-state condition of equal activities between a long-lived parent radionuclide and its short-lived daughter. The important criteria upon which secular equilibrium depends are:

- The parent must be long-lived; that is, negligible decay of the parent occurs during the period of observation, and
- The daughter must have a relatively short half-life. The relative difference in halflife in this latter criterion is further clarified by

$$\frac{\lambda_A}{\lambda_B} \leq\sim 10^{-4} \tag{2.30}$$

where λ_A and λ_B are the respective decay constants of the parent and daughter nuclides. The importance of these two requirements can be clearly seen if the ^{90}Sr(^{90}Y) equilibrium is taken as an example. The nuclide ^{90}Sr is the parent in the decay scheme

$$^{90}_{38}Sr \xrightarrow{t_{1/2}=28.8\text{years}} {}^{90}_{38}Y \xrightarrow{t_{1/2}=2.7\text{days}} {}^{90}_{40}Zr \text{ Stable} \tag{2.31}$$

The long half-life of ^{90}Sr definitely satisfies the first requirement for secular equilibrium, because over a quarter of a century is needed for it to lose 50% of its original activity. As will be seen, less than 3 weeks are required for secular equilibrium to be attained and, in this interim period, negligible decay of ^{90}Sr occurs.

To satisfy the second requirement the decay constants for ^{90}Sr and ^{90}Y, λ_A and λ_B, respectively, must be compared. The decay constants for ^{90}Sr and ^{90}Y are easily calculated from their half-lives , and the values are 6.60×10^{-5} and 2.57×10^{-1} day^{-1}, respectively. Consequently, in the comparison $\frac{\lambda_A}{\lambda_B} = 2.57 \times 10^{-4}$, and this is in agreement with the order of magnitude required for secular equilibrium.

$$N_B = \frac{\lambda_A}{\lambda_B - \lambda_A} N_A^0 (e^{-\lambda_A t} - e^{-\lambda_B t}) + N_B^0 e^{-\lambda_B t} \tag{2.32}$$

An equation for the growth of daughter atoms from the parent can be obtained from equation 2.32 by consideration of the limiting requirements for secular equilibrium. Since $\lambda_A \approx 0$ and $\lambda_A \ll \lambda_B$, $e^{\lambda_A t} = 1$ and λ_A falls out of the denominator in the first term. If the daughter nuclide is separated physically from the parent [43], $N_B^0 = 0$ at time $t = 0$ (time of parentdaughter separation) and the last term would fall out of equation 2.32. Thus, in the case of secular equilibrium, the expression of the ingrowth of daughter atoms with parent can be written as

$$N_B = \frac{\lambda_A N_A^0}{\lambda_B} (1 - e^{-\lambda_B t}) \tag{2.33}$$

If the observation of the ingrowth of the daughter is made over many half-lives of the daughter, it is seen that the number of atoms of daughter approaches a maximum

value, $\lambda_A N_A^0/\lambda_B$ which is the rate of production of daughter divided by its decay constant. The final form of equation 2.33 to be used for the calculation of the ingrowth of daughter can be expressed as following

$$N_B = (N_B)_{max}(1 - e^{-\lambda_B t}) \tag{2.34}$$

Since the activity of the daughter atoms, A_B, is proportional to the number of daughter atoms, or $A_B = k\lambda_B N_B$, where k is the coefficient of detection of the daughter atoms, equation 2.34 may also be written as

$$A_B = (A_B)_{max}(1 - e^{-\lambda_B t}) \tag{2.35}$$

Rutherford and Soddy [44] were the first to write and interpret equations 2.34 and 2.35 when they studied the equilibrium existing between radioactive Thorium and a daughter radionuclide. They noted the following:

The radioactivity of Thorium at any time is the resultant of two opposing processes: 1. The production of fresh radioactive material at a constant rate by the Thorium compound, and 2. The decay of the radiating power of the active material with time. The normal or constant radioactivity possessed by Thorium is an equilibrium value, where the rate of increase of radioactivity due to the production of fresh active material [daughter nuclide] is balanced by the rate of decay of radioactivity of that already formed. The experimental curve obtained with the hydroxide [this was the chemical form they used to separate the parent nuclide from the daughter] for the rate of rise of its activity from a minimum to a maximum value will therefore be approximately expressed by the equation $I_t/I_0 = 1 - e^{-\lambda t}$, where I_0 represents the amount of activity recovered when the maximum is reached, and I_t the activity

recovered after time t, λ being the same constant as before.

Let us take an arbitrary example of equal activities of 100 dpm of parent ^{90}Sr and 100 dpm of daughter ^{90}Y in secular equilibrium and calculate and graphically represent the ingrowth of ^{90}Y with its parent and also the decay of ^{90}Y subsequent to the separation of parent and daughter nuclides [43]. Identical activities of ^{90}Sr and ^{90}Y are arbitrarily chosen, because their activities are equal while in secular equilibrium prior to their separation.

Ernest Rutherford and Frederick Soddy in their classic paper on *The Cause and Nature of Radioactivity* in 1902 in the *Philosophical Magazine* made the first published observation of what is now known as secular equilibrium. They were studying the radioactivity of an isotope of Thorium and a daughter isotope, which they called ThX. The term "daughter isotope for an isotope decay product was not then established, because knowledge of radioactivity was only then at its infancy. They summarized their findings with the following:

The foregoing experimental results may be briefly summarized. The major part of the radioactivity of Thoriumordinarily about 54 percent is due to a non-thorium type of matter, ThX, possessing distinct chemical properties, which is temporarily radioactive, its activity falling to half value in about four days. The constant radioactivity of Thorium is maintained by the production of this material at a constant rate. Both the rate of production of the new material and the rate of decay of its activity appear to be independent of the physical and chemical condition of the system.

(We now know that the activity of parent and daughter nuclides are equal in secular equilibrium and the value of "about 54%" reported by Rutherford and Soddy was precisely 50%.)

2.4 Transient equilibrium

Like secular equilibrium, transient equilibrium is a steady-state condition between the parent and daughter nuclides. However, in transient equilibrium the parent daughter nuclides do not possess the same activities, but rather they decay at the same half-life, that of the parent nuclide.

The criterion upon which transient equilibrium rests is that the parent nuclide must be longer lived than its daughter, but not of the order of magnitude described by equation 2.30; that is, it is necessary that $\lambda_A < \lambda_B$. However, the ratio λ_A/λ_B should fall within the limits $10^{-4} < \lambda_A/\lambda_B < 1$.

The decay chain of ^{100}Pd serves as an example of parent daughter nuclides that may attain transient equilibrium. ^{100}Pd decays by electron capture to ^{100}Rh with a half-life of 96 h. The daughter nuclide ^{100}Rh decays by electron capture and positron emission to the stable nuclide ^{100}Ru. The half-life of the daughter nuclide is 21 h. The decay scheme may be represented as

$$^{100}_{46}Pd \xrightarrow{t_{1/2}=96\text{h}} ^{100}_{45}Rh \xrightarrow{t_{1/2}=21\text{h}} ^{100}_{44}Ru \text{ Stable} \tag{2.36}$$

The first criterion for transient equilibrium is satisfied in this case; the half-life of the parent nuclide is greater than that of the daughter. If the decay constants λ_A and λ_B are now calculated, we can determine whether or not the second criterion ($10^{-4} < \lambda_A/\lambda_B < 1$) is satisfied.

The value of λ_A, given by 0.693/96 h, is $7.2 \times 10^{-3}h^{-1}$, and that of λ_B, given by 0.693/21 h, is $3.3 \times 10^{-2}h^{-1}$. Consequently, the ratio $\lambda_A/\lambda_B = 2.2 \times 10^{-1}$ and lies within the limits of the second criterion.

If the general decay equation 2.32 of the daughter nuclide is considered, the term

$e^{-\lambda_B t}$ is negligible compared with $e^{-\lambda_A t}$ for sufficiently large values of t. Thus, the terms $e^{-\lambda_B t}$ and $N_B^0 e^{-\lambda_B t}$ may be dropped from equation 2.32 to give

$$N_B = \frac{\lambda_A}{\lambda_B - \lambda_A} N_A^0 e^{-\lambda_A t} \tag{2.37}$$

for the decay of the daughter nuclide as a function of time. Because $N_A = N_A^0 e^{-\lambda_A t}$, equation 2.37 may be written as

$$\frac{N_B}{N_A} = \frac{\lambda_A}{\lambda_B - \lambda_A} \tag{2.38}$$

From equation 2.38, it can be seen that the ratio of the number of atoms or the ratio of the activities of the parent and daughter nuclides is a constant in the case of transient equilibrium.

Since $A_A = K_A \lambda_A N_A$ and $A_B = K_B \lambda_B N_B$, where A_A and A_B are the activities of the parent and daughter nuclides, respectively, and k_A and k_B are the detection coefficients of these nuclides, equation 2.38 may be written in terms of activities as

$$\frac{A_B}{k_B \lambda_B}(\lambda_B - \lambda_A) = \frac{A_A}{k_A \lambda_A} \lambda_A \tag{2.39}$$

or

$$\frac{A_B}{A_A} = \frac{k_B \lambda_B}{k_A(\lambda_B - \lambda_A)} \tag{2.40}$$

If equal detection coefficients are assumed for the parent and daughter nuclides, equation 2.40 may be written as

$$\frac{A_B}{A_A} = \frac{\lambda_B}{(\lambda_B - \lambda_A)} \tag{2.41}$$

Thus, for transient equilibrium equation 2.41 indicates that the activity of the daughter is always greater than that of the parent by the factor $\lambda_B/(\lambda_B - \lambda_A)$. Equation 2.41 may likewise be written as

$$\frac{A_A}{A_B} = 1 - \frac{\lambda_A}{\lambda_B} \tag{2.42}$$

whereby the ratio A_A/A_B falls within the limits $0 < A_A/A_B < 1$ in transient equilibrium.

If an activity of 100 dpm is arbitrarily chosen for the daughter nuclide ^{100}Rh in transient equilibrium with its parent ^{100}Pd, the activity of ^{100}Pd can be found using either equation 2.41 or 2.42. Equation 2.41 gives

$$\frac{100dpm}{A_A} = \frac{3.3\times10^{-2}h^{-1}}{3.3\times10^{-2}h^{-1} - 7.2\times10^{-3}h^{-1}}$$

or

$$A_A = 78\ dpm$$

With the use of equation 2.41 or 2.42, the decay of the daughter nuclide may be calculated as a function of parent decay in transient equilibrium [45].

2.5 Neutron flux, cross-section and interaction rates

In this section the ideas of neutron flux and neutron cross sections will be introduced in order to express interaction rates quantitatively. Neutron interaction rates do not depend on the direction of neutron motion within the target material so we may visualize for simplicity a situation, which seldom occurs in practice, in which all neutrons are moving in the same direction in a parallel beam. The neutron flux, ϕ,

maybe define as the total number of neutrons which pass through a unit area normal to their direction per second [10].

If all the neutrons have the same speed, υ, and if the neutron density is, n, neutrons per unit volume, then:

$$\phi = n\upsilon$$

If in the more likely event the neutrons have a spectrum of speeds such that $n(\upsilon)d\upsilon$ is the number of neutrons per unit volume whose speed is in the range υ to $\upsilon + d\upsilon$, then:

$$\phi = \int_{\text{all speeds}} \upsilon n(\upsilon) \quad d\upsilon$$

For the case in which neutrons are moving in all directions the neutron flux can be define as the total track length of all neutrons in a unit volume per second. This definition consistent with the one given a view lines above for a parallel beam of neutrons, but it dose not depend on that condition. Being applicable to neutrons moving randomly in all directions without reference to there directions of motions, it emphasizes the scalar (as opposed to vector) nature of the neutron flux.

The interaction rate between a beam of neutrons and the nuclei in a target material has been experimentally observed to be proportional (a) to the neutron flux, and (b) to the number of atoms in the target, which is assumed to consist of a single isotope.

Consider a beam of neutrons, all of a speed, υ cm/s and density n neutrons/cm^3, incident on a target of area A cm^2 and thickness dx cm containing N $nuclie/cm^3$.

Now we can express the interaction rate F in the target material thus:

$$F \propto \phi NV$$

$$F = \sigma\phi NV \tag{2.43}$$

where $V = Adx$, the volume of the target, and NV is the total number of atoms of the isotope in the target in which the reaction is taken place.

The constant σ in equation 2.43 is known as the macroscopic cross section of the isotope concerned. Its units are cm^2/nucleis, and it can be regarded as the area presented by each nucleus to neutrons to cause a reaction. (This area is not the same as the actual size of the nucleus, in some cases it may be larger, in others it may be smaller.) The values of σ for most isotopes lie between 10^{-22} and $10^{-26} cm^2$, and the usual unit in which values of σ are quoted is the barn.

$$1 \quad barn = 10^{-24} cm^2$$

The total cross section of all the nuclei in unit volume of a material is called the macroscopic cross section, Σ, and has units cm^2/cm^3 or cm^{-1},

$$\Sigma = N\sigma$$

and the interaction rate per unit volume,

$$F = \Sigma\phi \tag{2.44}$$

The probability that a neutron entering the target will interact within a distance dx is:

$$\frac{\begin{array}{c}\text{Number of neutrons interacting per} \\ \text{second in a target of thickness dx}\end{array}}{\begin{array}{c}\text{Number of neutrons per second} \\ \text{incident on the target}\end{array}} = \frac{\sigma\phi NAdx}{\phi A} = \sigma N dx = \Sigma dx \tag{2.45}$$

It follows that the macroscopic cross section can be interpreted as the probability per unit track length that a neutron will interact.

The attenuation of a beam of neutrons in a target material can be found by equating the rate of interaction in an element of thickness dx to the difference between the number of neutrons entering and leaving the element per second:

$$\text{Interaction rate} = (\text{Flux in} - \text{Flux out}) \times A$$

$$\sigma\phi N A dx = -A d\phi$$

(the negative sign indicates a decreasing flux).

Rearranging:

$$\frac{d\phi}{\phi} = -\sigma N dx = -\Sigma dx$$

The solution of this equation for $\phi(x)$, the flux which penetrates to a distance x without interacting, is:

$$\phi(x) = \phi_0 e^{-\Sigma x} \tag{2.46}$$

where ϕ_0 is the incident neutron flux.

The average distance that a neutron travels without interacting is known as the mean free path, λ. Considering a number of neutrons, n, we may write:

$$\lambda = \frac{1}{n} \sum_{\text{all neutrons}} \left(\begin{array}{c} \text{Number of neutrons} \\ \text{which travel a distance} \\ \text{x without interacting} \end{array} \right) \times \left(\begin{array}{c} \text{Probability of} \\ \text{interaction in} \\ \text{distance dx} \end{array} \right) \times x \ .$$

The quantity on the right of the summation is the total distance traveled by all neutrons without interaction. Using equations 2.45 and 2.46 and alerting the right-hand side to an integral over all possible values of x, namely 0 to ∞, the equation for λ is:

$$\lambda = \frac{1}{n} \int_0^\infty n e^{-\Sigma x} \Sigma x dx = \frac{1}{\Sigma} \tag{2.47}$$

Thus the mean free path is seen to be the reciprocal of the macroscopic cross section.

The preceding discussion in this section has made no distinction between the different types of neutron interaction such as scattering, capture of fission, and all the statements and results obtained so far apply to any type of interaction.

Thus the rates at which elastic scattering, inelastic scattering, capture and fission take place are characterized by the elastic scattering cross section, σ_s, the inelastic scattering cross section, σ_i, the capture cross section, σ_c, and the fission cross section, σ_f, (which is zero for all non-fissionable isotopes). The total cross section, σ_t, is the sum of these cross section, and measures the rate at which any type of interaction takes place:

$$\sigma_t = \sigma_s + \sigma_i + \sigma_c + \sigma_f$$

Chapter 3

Radioactivity of accelerator

3.1 Medical linear accelerators: classification and components

Medical Linear Accelerators (linac) have been in clinical use since the early 1950s, either to produce fast electrons or to generate x-rays for radiation therapy, and machines of this type have become the mainstay of most radiotherapy departments [14]. The Betatron was the first accelerator to be developed and used for electron therapy [53] and photon therapy [54].

Fig 3.1 shows the component system of a linac. Medical linacs are cyclic accelerators which accelerate electrons to kinetic energies from 4 MeV to 25 MeV using non-conservative microwave radiofrequency (RF) fields in the frequency range from 1000 MHz to 10000 MHz, with the vast majority running at 2856 MHz.

In a linear accelerator the electrons are accelerated following straight trajectories in special evacuated structures called accelerating waveguides. Electrons follow a

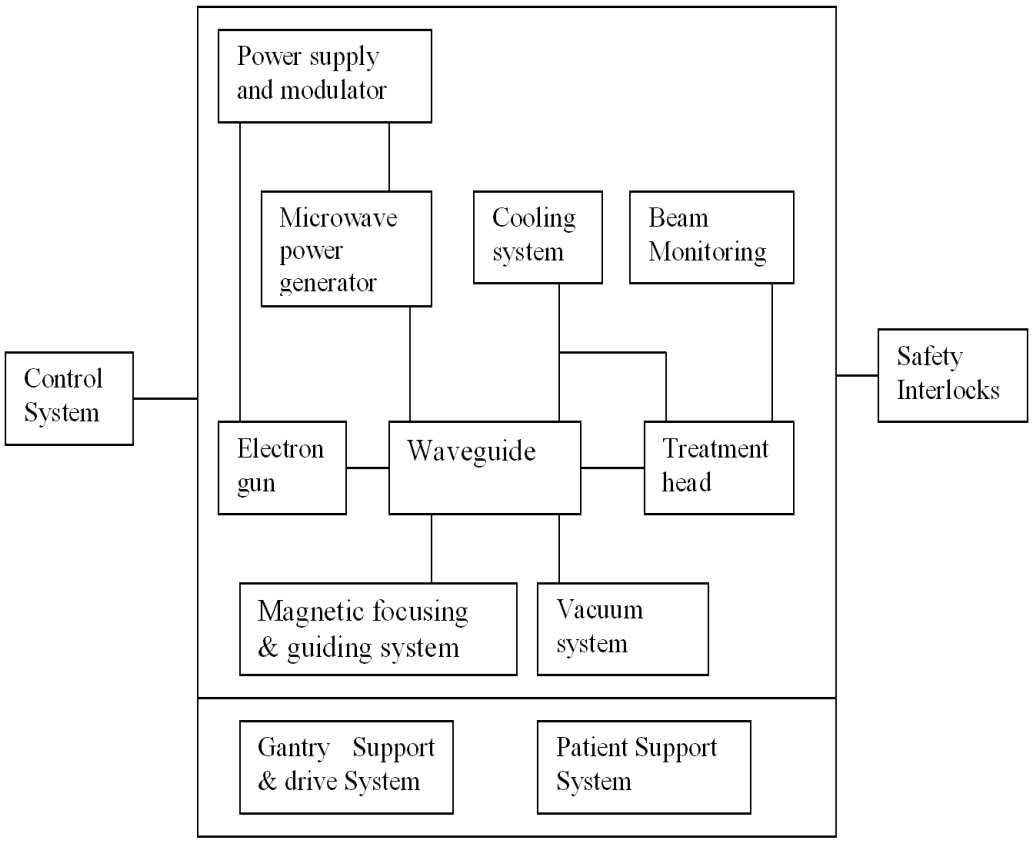

Figure 3.1: Block diagram showing the component system of linear accelerators.

linear path through the same, relatively low, potential difference several times; hence, linacs also fall into the class of cyclic accelerators just like the other cyclic machines that provide curved paths for the accelerated particles (e.g., Betatron)

The high power RF fields, used for electron acceleration in the accelerating waveguides, are produced through the process of decelerating electrons in retarding potentials in special evacuated devices called magnetrons and klystrons.

Various types of linacs are available for clinical use. Some provide x-rays only in the low megavoltage range (4 MV or 6 MV) others provide both x-rays and electrons at various megavoltage energies. A typical modern high-energy linac will provide two photon energies (6 MV and 18 MV) and several electron energies (e.g., 6, 9, 12, 16, 22 MeV) [16].

During the past 40 years, medical linacs have gone through five distinct generations, making the contemporary machines extremely sophisticated in comparison with the machines of the 1960s. Table 3.1 shows the classification of the five generations with their new features.

The linacs are usually mounted isocentrically and the operational systems are distributed over five major and distinct sections of the machine: gantry; gantry stand or support; modulator cabinet; patient support assembly, i.e., treatment couch and control console.

The length of the accelerating waveguide depends on the final electron kinetic energy, and ranges from 30 cm at 4 MeV to 150 cm at 25 MeV.

The main beam-forming components of a modern medical linac are usually grouped into six classes: injection system; RF power generation system; accelerating waveguide; auxiliary system; beam transport system; and beam collimation and beam

Table 3.1: The classification of the five generations of medical linear accelerators with new features [16].

No.	**Energy**	**Particles**	**Features**
1	4-8 MV	Photons	Straight through beam; fixed flattening filter; external wedges; symmetric jaws; single transmission ionization chamber; isocentric mounting.
2	10-15 MV	Photons and electrons	Bent beam; movable target and flattening filter; scattering foils; dual transmission ionisation chamber; electron cones.
3	18-25 MV	Photons and electrons	Dual photon energy and multiple electron energies; achromatic bending magnet; dual scattering foils or scanned electron pencil beam; motorized wedge; asymmetric or independent collimator jaws.
4	High energy	Photons and electrons	Computer-controlled operation; dynamic wedge; electronic portal imaging device; multileaf collimator (MLC).
5	High energy	Photons and electrons	Photon beam intensity modulation with MLC; full dynamic conformal dose delivery with intensity modulated beams produced with a MLC.

monitoring system.

The injection system is the source of electrons, essentially a simple electrostatic accelerator called an electron gun. Two types of electron guns are in use as sources of electrons in medical linacs: Diode type and Triode type.

Both electron gun types contain a heated filament cathode and a perforated grounded anode; in addition, the triode electron gun also incorporates a grid. Electrons are thermionically emitted from the heated cathode, focused into a pencil beam by a curved focusing electrode, and accelerated toward the perforated anode through which they drift to enter the accelerating waveguide.

The electrostatic fields, which are used to accelerate the electrons in the diode gun, are supplied directly from the pulsed modulator in the form of a negative pulse delivered to the cathode of the gun.

The microwave radiation, used in the accelerating waveguide to accelerate electrons to the desired kinetic energy, is produced by the RF power generation system, which consists of two major components: RF power source and Pulsed modulator.

The RF power source is either a magnetron or a klystron. Both are devices using electron acceleration and deceleration in vacuum for production of the high power RF fields. Both types use a thermionic emission of electrons from a heated cathode and accelerate the electrons toward an anode in a pulsed electrostatic field; however, their design principles are completely different.

The high voltage (100 kV), high current (100 A), short duration (1 μs) pulses are required by the RF power source (magnetron or klystron) and the injection system (electron gun) are produced by the pulsed modulator. The circuitry of the pulsed modulator is housed in the modulator cabinet that, depending on the particular linac

installation design, is located in the treatment room, special mechanical room next to the treatment room, or in the linac control room.

A magnetron is a source of high power RF required for electron acceleration, while a klystron is an RF power amplifier that amplifies the low power radiofrequency generated by an RF oscillator commonly called the RF driver.

Waveguides are evacuated or gas-filled metallic structures of rectangular or circular cross-sections used in transmission of microwaves. Two types of waveguides are used in linacs: RF power transmission waveguides and accelerating waveguides. The power transmission waveguides transmit the RF power from the power source to the accelerating waveguide in which the electrons are accelerated.

The electrons are accelerated in the accelerating waveguide by means of an energy transfer from the high power RF fields, which are set up in the accelerating waveguide and are produced by the RF power generators.

The simplest kind of an accelerating waveguide is obtained from a cylindrical uniform waveguide by adding a series of disks (irises) with circular holes at the center, placed at equal distances along the tube. These disks divide the waveguide into a series of cylindrical cavities that form the basic structure of the accelerating waveguide in a linac. The cavities serve two purposes: To couple and distribute microwave power between adjacent cavities and to provide a suitable electric field pattern for acceleration of electrons.

Two types of accelerating waveguides have been developed for acceleration of electrons: Traveling wave structure and standing wave structure.

The microwave power produced by the RF generator is carried to the accelerating

waveguide through rectangular uniform S-band waveguides, which are either evacuated or, more commonly, pressurized with a dielectric gas (freon or sulfur hexafluoride, SF_6) to twice the atmospheric pressure.

An important component, which must be inserted into the RF power transmission circuit between the RF generator and the accelerating waveguide, is a circulator (sometimes referred to as an isolator) which transmits the RF power from the RF generator to the accelerating waveguide but is impervious to reflected radiation moving in the opposite direction, thereby protecting the RF source from the reflected power.

The linac auxiliary system consists of several services, which are not directly involved with electron acceleration, yet they make the acceleration possible and the linac viable for clinical operation. The linac auxiliary system comprises four systems: Vacuum pumping system producing a vacuum pressure of 10^{-6} tor in the accelerating guide and the RF generator; Water cooling system used for cooling the accelerating guide, target, circulator, and RF generator; Optional air pressure system for pneumatic movement of the target and other beam shaping components; and Shielding against leakage radiation.

In low energy linacs the target is embedded into the accelerating waveguide and no beam transport between the accelerating waveguide and target is required.

Bending magnets are used in linacs operating at energies above 6 MeV where the accelerating waveguides are too long for straight-through mounting. The accelerating waveguide is usually mounted parallel to the gantry rotation axis and the electron beam must be bent to make it strike the x-ray target or be able to exit through the beam exit window. Three systems for electron bending have been developed: 90^o

bending; 270^o bending; and 112.5^o bending.

In medium (10 MV) and high-energy linacs (above 15 MV) an electron beam transport system is used for transporting the electron beam from the accelerating waveguide to the x-ray target or to the linac exit window for electron beam therapy. The system consists of evacuated drift tubes and bending magnets. In addition, steering coils and focusing coils, used for steering and focusing of the accelerated electron beam, also form components of the beam transport system.

The linac head contains several components, which influence the production, shaping, localizing, and monitoring of the clinical photon and electron beams.

Electrons, originating in the electron gun, are accelerated in the accelerating waveguide to the desired kinetic energy and then brought, in the form of a pencil beam, through the beam transport system into the linac treatment head, where the clinical photon and electron beams are produced.

The important components found in a typical head of a fourth or fifth generation linac include: Several retractable x-ray targets; Flattening filters and electron scattering foils (also called scattering filters); Primary and adjustable secondary collimators; Dual transmission ionization chambers; Field defining light and range finder; Optional retractable wedges; Optional multileaf collimator (MLC).

Special cones (applicators) are used to collimate the electron beams. Each clinical photon beam has its own target/flattening filter combination. The flattening filters and scattering foils (if used for electron beams) are mounted on a rotating carousel or sliding drawer for ease of mechanical positioning into the beam, as required. The primary collimator defines a maximum circular field which is then further truncated with

an adjustable rectangular collimator, consisting of two upper and two lower independent jaws, and producing rectangular and square fields with a maximum dimension of $40 \times 40\ cm^2$ at the linac isocenter.

The field defining light and range finder provide convenient visual methods for correctly positioning the patient for treatment using reference marks. The field light illuminates an area that coincides with the radiation treatment field on the patient's skin, while the range finder is used to place the patient at the correct treatment distance; by projecting a centimeter scale whose image on the patient's skin indicates the vertical distance from the linac isocenter.

3.2 Fundamental principle of induced radioactivity in accelerator

In principle, induced radioactivity can be produced at all accelerators capable of liberating neutrons and other hadrons [9, 17]. When the accelerated beam strikes a nucleus, it converts it into a different nuclide, which may be radioactive. In this research, the activity of a given radionuclide refers to the number of atoms that decay per unit time.

The number of atoms of the radionuclide of interest per unit volume will thus be governed by the following differential equation during the period of the irradiation [17]:

$$\frac{dn(t)}{dt} = -\lambda n(t) + N\sigma\phi \tag{3.1}$$

where $n(t)$ is the atoms of the radionuclide per cm^3 at time t. N is the number

of "target" atoms per cm^3, σ is the interaction cross section in unit of cm^2, and ϕ is the flux density ($cm^{-2}.sec^{-1}$) of incident particles. On the right hand side of equation 3.1, the first term represents the loss of radionuclides through decay during the irradiation while the second term represents the gain of radionuclides through the production reaction under consideration.

The equation 3.1 has the following solution for $t = t_i$:

$$n(t_i) = \frac{N\sigma\phi}{\lambda}(1 - e^{-\lambda t_i}) \tag{3.2}$$

where t_i is the irradiation time. After the irradiation has ceased ($t > t_i$), the specific activity as a function of the "cooling time or decay period", t_c, will obviously decay exponentially and be given by:

$$a(t_c) = N\sigma\phi[1 - e^{-\lambda t_i}]e^{-\lambda t_c} \tag{3.3}$$

where t_c is the cooling time.

3.3 Activation of accelerators components

In the last years, a lot of work has been done on the measurements of induced radioactivity by different techniques from linear accelerators [12, 13, 19, 20, 22, 25, 26, 27, 28, 29, 33, 34, 35, 36]. In addition, some of the investigators identified the typical radionuclides produced in the treatment room by the activation from the air [30, 31, 32]. The activation arises primarily from photonuclear reaction and neutron capture. In some special cases, radioactivity can be produced at much lower energies by exothermic nuclear reaction that either produce radionuclides directly or that emit neutrons capable of inducing radioactivity through their secondary interactions.

Alan Rawlinson *et al* [12] estimated the dose to radiation therapists from activation at high-energy accelerators. This study was conducted at a new Varian Clinac 21EX linear accelerator at Princess Margaret Hospital, Toronto. Gamma ray spectrometry was used by Alan Rawlinson to identify the major isotopes responsible for activation at a representative location in the treatment room of an 18 MV accelerator. He developed formalism to estimate the activation dose (μSv/week) due to successive patient irradiation cycles. His results for conventional therapy represents about 60 μSv/week for an 18 MV workload of 60 000 MU/week.

Yi Zhen Wang *et al* [13] studied the induced activity on several linac installations. The study of these investigators was conducted at a Clinac 2300C/D linac (6 and 18 MV), Clinac 6EX (6 MV photon beam), a Clinac 18 (10 MV photon beam), and a Clinac 21EX (6 and 18 MV photon beams). A calibrated ionization chamber survey meter was used in the measurements of the induced activity. The theoretical and experimental studies of Yi Zhen Wang reveal that the activation level in the morning before any clinical work increases from Monday to Saturday and then decreases during the weekend. They found that the activation level reaches its practical saturation value after a 30 min continuous irradiation, corresponding to 12000 MU at a "dose rate" of 400 MU/min. Determination of the trends in the activation level in a typical clinical mode was carried out by them using "dose" of 300 MU which is given 20 times in 15 min intervals.

Almen *et al* [22] estimated the absorbed dose to technicians due to induced activity in linear accelerators. The study of these investigators was conducted at Clinac 1800 - Varian (16 MV), SL 75/20 - Philips (15 MV), SL 75/20 - Philips (14 MV), Dynaray LA20 - Brawn Boveri (13 MV), SL 75/20 - Philips (17 MV), Microtron,

MM22 - Scanditronix (13 MV) and Racetrac microtron, MMSO - Scanditronix (15 MV). Thermoluminescent (TL) dosimeters were been used by these investigators to measure the absorbed dose to the trunk and to the hands of technicians working with accelerators for radiotherapy. Also they compared the readings of TL dosimeters with a plastic scintillator radiation survey meter (Gammameter 2414, Studsvik Energiteknik AB, Sweden). They found that, total annual absorbed dose to the trunk and to the hands estimated to be 2 mGy, of which the induced activity contributes one-third (0.7 mGy).

Powell *et al* [26] estimated the dose rates due to the activation of the treatment room and various parts of the accelerator. They measured the neutron equivalents dose using the standard NRPB neutron badges and also with the developed CR-39 dosimeters. They measured the photon dose rates with a Victoreen 470A survey meter and outside the actual treatment room they measured the neutron dose rates with a Nuclear Enterprises NM2 remmeter, which is a standard Anderson-Braun moderator containing a boron trifluoride proportional counter. The estimation of the daily dose made by these investigators was found to be between 3 and 11 μSv with a mean of 6 μSv.

Loi *et al* [21] published paper reports the measured neutron production from a Mobetron mobile electron linac, operated at 12 MeV, and compares the results with those from a conventional linac, also operated at 12 MeV in electron mode. They used passive bubble detectors in the scattering foil Neutron leakage measurements. The investigators estimation of neutron dose equivalent rates per unit of electron dose delivered by the Mobetron at its normal treatment distance (50 cm Source Skin Distance "SSD") were found to be 0.33 $\mu Sv.Gy^{-1}$ at the accelerator head, 0.18

$\mu Sv.Gy^{-1}$ in the patient plane at 15 cm from the beam axis and 0.31 $\mu Sv.Gy^{-1}$ at the floor plane, on the beam axis and under the beam stopper.

A model to calculate the induced dose rate around an 18 MV ELEKTA linear accelerator was developed by Bruce Perrin *et al* [25]. From this model, the dose received by the staff using the machine can be estimated. All measurements of this investigator for the derivation of the activation model were made with a calibrated ionization dose rate meter reading down to 0.1 $\mu Sv.h^{-1}$. The calculations of dose rates were found to be 4.5 $\mu Sv.h^{-1}$ after the beam was stopped. This group estimate the maximum annual whole body dose for a treatment therapist, for 60 000 MUs per week to be 2.5 mSv.

A lot of works has been done on the measurements of induced radioactivity by different techniques from linear accelerators. Table 3.2 shows summary of these works during the last years.

The goal of the present study was to investigate the induced activity produced in a medical linear accelerator using new techniques (filter paper and portable spectroscopy) and to compare the results with the mathematical model.

3.4 Production of airborne radioactivity

Thomas and Stevenson have presented a very useful synopsis of the production of radioactivity in air [38]. Swanson and Thomas [39] reprised this discussion. The principal source of radioactivity in air at accelerators is due to the interaction of primary and secondary particles directly with the constituent target nuclei in the air in accelerator room. Activated dust and gaseous emission from activated liquids are of much less importance. Table 3.3 [37] gives the abundances and number densities of

atoms of the most common stable isotopes found in the atmosphere both by volume percentage and in terms of the atomic density, N_j.

Patterson and Thomas [40], have expanded the general activation equation, equation 3.3, to derive the total specific activity, S (typically in units of $Bq.cm^{-3}$), of an enclosed volume of radioactive air;

$$S = C \sum_i \{ \sum_j N_j \bar{\sigma}_{ij\gamma} \phi_\gamma + \sum_j N_j \bar{\sigma}_{ij_{th}} \phi_{th} + \sum_j N_j \bar{\sigma}_{ij_{HE}} \phi_{HE} \} \{ 1 - e^{-\lambda_i t_i} \} e^{-\lambda_i t_c} \quad (3.4)$$

where ϕ_γ, ϕ_{th} and ϕ_{HE} represent the average photon, thermal neutron, and high energy particle flux densities, respectively. While t_i is the irradiation time and t_c represents the decay time. The $\bar{\sigma}_{ij}$ values are the corresponding cross sections averaged with the energy-dependent flux density over energy. The constant C is the conversion to specific activity and is equal to unity for activity in Becquerels cm^{-3} if all the units of length implicit in the quantities in equation 3.4 are expressed in cm. The outer sum over index i include all possible radionuclides produced and the sum over the index ,j, is over the parent atoms found in air. The flux densities are, without further information, the average over some relevant spatial volume.

In other hand in the electron accelerators, significant air activation will not occur without bremsstrahlung because the nuclear cross sections of electrons are about two orders of magnitude smaller than those of photons [3]. This airborne radioactivity is generally short-lived and the concentrations are usually quickly reduced to levels where the exposure rates ($R.h^{-1}$), or equivalently the absorbed dose rates ($Gy.h^{-1}$) are small compared to those due to the accelerator components. This result is because the radiation length of air is so much longer than that of any solid material.

3.5 Radiological protection standard

The basic consideration of radiation protection were stated by International Commission on Radiological Protection (ICRP) in Publication 26, and reiterated in Publication 60 [6, 7]. ICRP Publication 26 recommended a system of dose limitation that has three interrelated components:

- justification−no practice shall be adopted unless its introduction produces a positive net benefit
- optimization *maximum permissible to one of as low as reasonably achievable* (ALARA)−all exposures shall be kept as low as reasonably achievable, economic and social factors being taken into account
- compliance with dose limits−the dose equivalent to individuals shall not exceed the appropriate limits recommended by ICRP

When the process of justification and optimization have been implemented to demonstrate that there is a net benefit from the use of ionizing radiation and that result from the operation must be compared with the appropriated dose limits to ensure that no unacceptable doses occur. The present dose limits recommended by National Council on Radiation Protection and Measurements (NCRP) for different segments of the population are listed in NCRP report No. 116, *Limitation of exposure to ionizing radiation* [8].

When ICRP, in its publication 26 [6], presented new radiation protection recommendations, the whole philosophy of radiation protection changed in emphasis from one of ALARA below an administratively or legally prescribed limit. The limit is to

be considered as legally acceptable ceiling above which there maybe a penalty, but management must review operations to maintain radiation exposure ALARA below the limit. The degree attainable below the limit is a judgment based on many factors that can be different for the same situation at different organizations.

Recommendations of the ICRP [7] states in Paragraph S26:"Subject to medical advice in individual cases, there need be no special restrictions applied to the exposure of an individual following a control period in which the exposure of the individual has exceeded a dose limit. Such events should call for a thorough examination, usually by the regulatory agency, of the design and operational aspects of protection in the installation concerned, rather than for restrictions or penalties applied to the exposed individual."

It is clear from the above that both ICRP and NCRP consider control of exposure at the source and not at the individual to be most important. This is particularly true in the design of anew facility. For example, the dose criteria for shielding design in anew facility should be placed at a small fraction of the dose limit. For facilities already in operation, the inclusion of additional shielding or other methods for controlling the source will fall under the "as reasonably achievable" portion of the ALARA principle [9].

Table 3.2: The summary of some works during the last years on the induced radioactivity form linear accelerators using different techniques.

No.	Author name	Date	Linear model	Linear energy	Method of investigation	Estimated dose
1	Loi *et al*	2006	Mobetron mobile electron linac	12 MeV	Passive bubble detectors	The neutron dose is 0.33 $\mu Sv.Gy^{-1}$ at the accelerator head.
2	Yi Zhen Wang *et al*	2005	Varian, Clinac 2300C/D ,Clinac 6EX, Clinac 18 and Clinac 21EX	6,18,10 MV 22 MeV	Math. Model and survey meter	Activation level for a 22 MeV is essentially negligible.
3	Bruce Perrin *et al*	2003	Elekta	18 MV	Math. Model and ionization dose rate meter	The max annual whole body dose for a therapist, for 60 000 MUs per week is 2.5 mSv
4	Alan Rawlinson *et al*	2002	Varian Clinac 21EX	18 MV	Portable Gamma ray spectrometer and Math. Model	$60\mu Sv/w$ for therapist workload of 60 000 MU/week".
5	Almen *et al*	1991	Clinac 1800 - Varian and , SL 75/20 - Philips, SL 75/20 Philips, Dynaray LA20 - Brawn Boveri, SL 75/20 Philips, Microtron, MM22 Scanditronix Racetrac microtron, MMSO Scanditronix	13, 14, 15, 16 and 17 MV	TLD and survey meter	Total annual absorbed dose to the trunk and to the hands estimated to be 0.7 mGy
6	Powell *et al*	1987	Clinac 20	18 MV	NRPB neutron badges , proportional counter and survey meter	Daily dose between 3 and 11 μSv with a mean of $6\mu Sv$.
7	Brien *et al*	1985	Therac-25	25 MeV	Remotely controlled Scanner	Max. 250 $\mu Sv/h$

Table 3.3: Abundances of the most prominent stable nuclides in the atmosphere at sea level [37].

Isotope	**Percentage by volume in the atmosphere (atoms)**	N_j **(atoms cm^{-3}) at room temperature**
^{14}N	78.16	4.199 x 10^{19}
^{16}O	20.00	1.075 x 10^{19}
^{40}Ar	0.467	1.558 x 10^{17}
^{15}N	0.29	2.149 x 10^{16}
^{18}O	0.04	1.255 x 10^{17}

Chapter 4

Materials and Methods

4.1 Introduction

In this medical study for radionuclides, most of experiments were carried out on a Clinac 2100C Linac (15 MV photon beams) installed at the Maggiore Hospital, which located in Trieste, Italy.

Several methods were used for the determination of induced radioactivity of Clinac 2100C. Each of these methods will be discussed in this chapter. The methods which were used in this work were:

1. Filter paper
2. Portable spectrometer
3. Mathematical model
4. Monte Carlo Simulation

Most points of interest in the treatment room of Clinac 2100C in our experiments are shown in Fig. 4.1. Measurements of induced activity were carried out for the

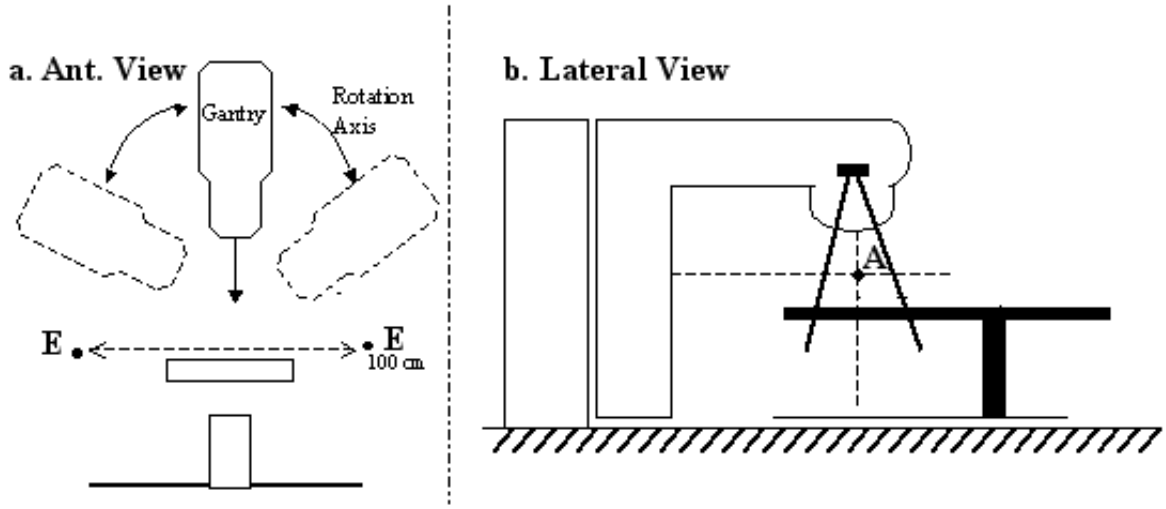

Figure 4.1: Schematic diagram of a linac and the location of the four points of interest. (a) The ant. view shows points E which relevant for the equivalent dose to RTT. (b) The Lateral view shows point A, which relevant for patient dose.

most part at the machine isocenter (point A) and at the point on patient plane 100 cm laterally to the isocenter (point E). The activation levels at point E are relevant for the equivalent dose to radiotherapy technologist (RTT). Additional point ,D, of interest located outside the treatment room "control room" and not shown in Fig 4.1 relevant for the additional equivalent dose to RTT. This equivalent dose not from induced activity but from the contribution of x-ray scattered and transmitted through the walls of treatment room.

We define the linac setup for a reference experimental setup and relative experimental setup. The Clinac 2100C reference experimental setup used most often in our experiments was as follows: (1) photon mode: 15 MV; (2) source-axis distance (SAD): 100 cm; (3) field size: 10 x 10 cm^2 at the isocenter; (4) dose: 400 MU, (5) dose rate: 240 MU/min; (6) Gantry angle: zero degree; and (7) patient couch height: 110

cm from the linac target. The setup of the measurements carried out with different filed sizes and doses were defined as relative experimental setup.

The machine workload is defined as follows: in a typical treatment workday of 7 h, 400 MU are delivered to each patient with a dose rate of 240 MU/min, and four patients are treated per hour.

The year of installation of Clinac 2100C linac, its manufacturer and other characteristics was shown in Table 4.1.

4.2 Filter paper method

Air is made radioactive by electron accelerators operating above approximately 10 MeV by photoneutron reaction with oxygen and nitrogen [32] as mentioned in section 3.4. To examine this activation of air and other nuclides, filter papers were used. After the end of collection time, spectrum was measured from the filter papers using special detector.

The detector used was high-purity germanium (HPGE) spectrometer, while the filter paper method is considered for first time for the determination of induced activity and radionuclides in the linear accelerators.

4.2.1 Gamma spectrometry

Today large Ge crystals of either p or n type are grown with the low impurity levels needed. The detectors fabricated from these crystals are called intrinsic or high-purity detectors. They can be stored indefinitely at room temperature. Detectors of different size or geometry are available, such as planar detectors, coaxial detectors,

Table 4.1: The characteristics of Clinac 2100C linac.

No.	Characteristics	Details/Description
1	Linear accelerator model	Clinac 2100C
2	Manufacturer	Varian Oncology System
3	Year of installation	2002
4	Electron energy (MeV)	6, 9, 12, 15, and 18
5	Photon energy (MV)	6 and 15
6	Target to skin distance (cm)	100
7	Target to flattening filter distance (cm)	12.5
8	Target to top/bottom jaws (cm)	28.9
9	Target to block tray (cm)	65.4
10	Target material	${}^{184}_{74}W$ Tungsten
11	Target thinness (cm)	0.5
12	Collimator material	${}^{184}_{74}W$ Tungsten
13	Flatting filter material	Stainless Steel
14	Maximum field size (cm^2)	40×40
15	Minimum field size (cm^2)	1×1
16	MLC providing	Yes
17	Treatment room dimension (m^2)	4 x 4

and well-type detectors. Others differ in the choice of contacts, of the choice of the entrance window (Al, Be, . . .), the selection of the cryostat construction materials, and so on [46].

The equipment used for gamma ray measurement is a gamma spectrometer system consisting of the following (see Fig. 4.2):

1. Detector system (including preamplifier and high-voltage filter),
2. High-voltage bias supply,
3. Spectroscopy amplifier (shaping amplifier),
4. Pulse height analyzer (PHA),
5. Printer.

4.2.2 The detector system

The detector element absorbs the energy from an incident gamma ray or x-ray and produces a current pulse whose integral is proportional to the absorbed energy. The type of detector used was high purity Germanium coaxial detector p-Type. The crystal diameter is 50.2 mm.

4.2.3 Detector configuration

The detector assemble consists of three parts as following:

1. Liquid nitrogen dewar
2. Cryostat

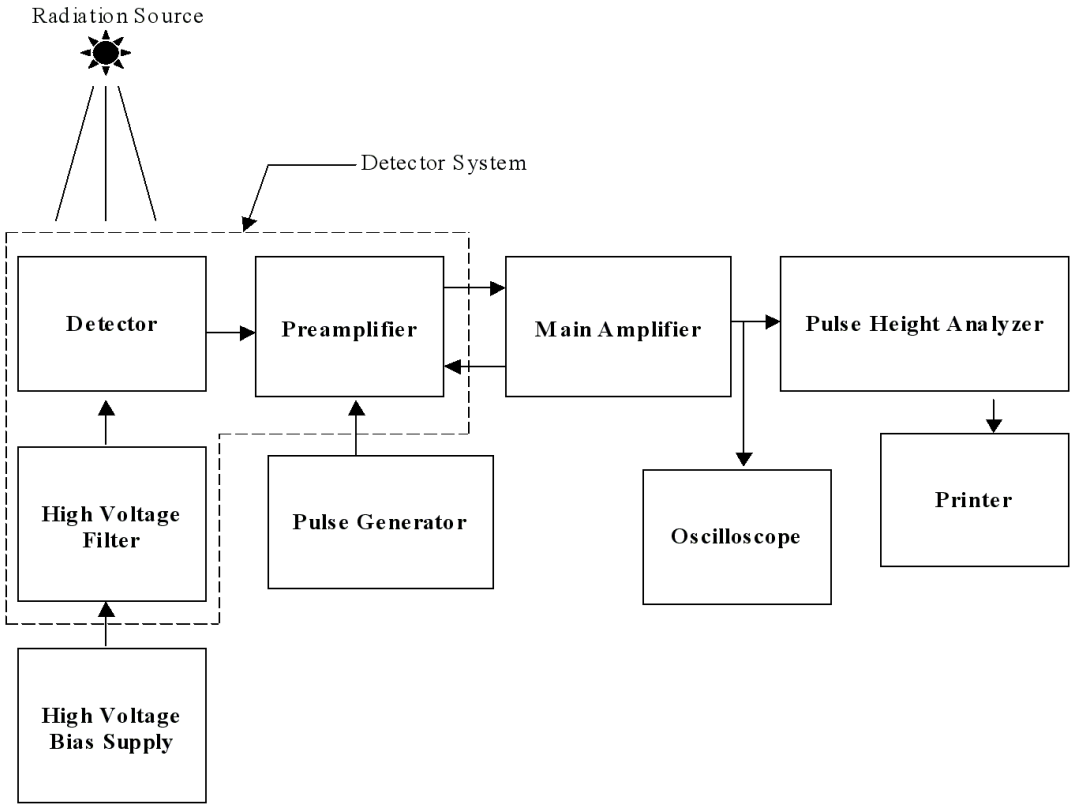

Figure 4.2: Block diagram of Spectroscopy System.

3. Electronic package

Liquid nitrogen dewar was used with pure Germanium detector for cooling purpose. The detector was cooled to reduced leakage current to avoid spoil their excellent energy resolution [47]. The temperature was reduced to 77 K through the use of an insulated dewar in which a reservoir of liquid nitrogen is kept in thermal contact with the detector.

The detector was housed in a vacuum-tight cryostat to inhibit thermal conductivity between the crystal and the surrounding air. The cryostat is evacuated and sealed by the manufacturer, although a pumping port provided to facilitate unusual operation such as high-temperature annealing. A molecular sieve was also provided within the sealed volume in the detector in order to provided some passive pumping inside the vacuum space. Thin end window was located near the crystal to minimize the attenuation of gamma rays before they enter the germanium. The cryostat mounted vertical on the liquid nitrogen dewar as shown in Fig. 4.3. The dewar capability to hold nitrogen was 30 liters.

The detector was fitted with an interlock that prevents application of high voltage to the detector unless it has reached a low temperature. This interlock is necessary since any inadvertent application of high voltage at room temperature leads to excessively high leakage current that will likely destroy the input of the preamplifier.

The preamplifier is one of the electronic part of the cryostat package in our HPGE system. The input stages of the preamplifier are also cooled along with the detector to reduce electronic noise.

The distance from end cap to Crystal was 3 mm and other technical specification can be shown in Table 4.2.

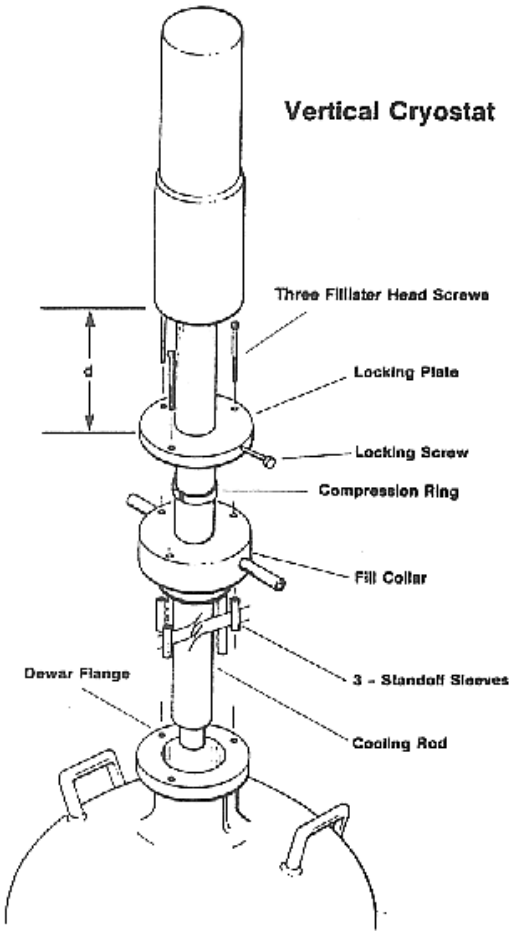

Figure 4.3: The components of Intrinsic Germanium Coaxial Detector p-Type.

4.2.4 Standard characteristics of the detectors

- **Energy resolution**

  From the spectra created by HPGE detector, observed peaks have a finite width. Peak broadening is due to the statistical fluctuations in the number of electron-hole pairs created in the active detector volume $(FWHM)_{det}$ and to the electronic noise of the different elements of the amplification chain. The resolution is expressed by full width at half-maximum (FWHM), and it can be readily obtained from the spectra. The different noise contributions add quadratically according to the equation

$$FWHM = \sqrt{(FWHM)^2_{det} + (FWHM)^2_{elect}} \tag{4.1}$$

  $(FWHM)_{det}$ and $(FWHM)_{elect}$ represent the detector and the electronic contribution in the total FWHM.

  The energy E released in the detector is shared by two processes, namely direct

Table 4.2: Technical specification of HPGE coaxial photon detector system.

Specification	**Values**
Detector Model	GMX20P
Crystal diameter	50.2 mm
Crystal length	79.8 mm
End Cap to Crystal	3 mm
Detector window thickness	0.5 mm
Leakage current	< 50 Pa

ionization and lattice vibrations. Both processes may lead to the generation of electronhole pairs.

$$N = \frac{E}{\varepsilon} \tag{4.2}$$

where ε is average energy required to create one ion-electron pair.

The second process obeys a Gaussian distribution and, if direct ionization would be negligible, the variance σ_N of the number of charge carriers N would be given by the equation

$$\sigma_N = \sqrt{N} = \sqrt{\frac{E}{\varepsilon}} \tag{4.3}$$

When the variance σ is expressed in energy units (eV), equation 4.3 becomes

$$\sigma = \varepsilon\sqrt{N} = \sqrt{E\varepsilon} \tag{4.4}$$

and the intrinsic $(FWHM)_{det}$ is calculated as

$$(FWHM)_{det} = 2.35\sqrt{E\varepsilon} \tag{4.5}$$

where the factor 2.35 is a statistical property of the Gaussian distribution and gives the ratio between FWHM and the variance of a Gaussian distribution. In practice, however, direct ionization is not negligible at all, justifying the introduction of a correction factor F, the so-called Fano factor:

$$(FWHM)_{det} = 2.35\sqrt{FE\varepsilon} \tag{4.6}$$

The Fano factor has an approximate value of 0.1 for Ge.

- **The Peak-to-Compton Ratio**

  Following the Institute of Electrical and Electronics Engineers (IEEE) standards the peak-to- Compton ratio is defined as the ratio between the maximum number of counts in the channel at the top of the 1332.5-eV peak of ^{60}Co and the average channel count between 1040 and 1096 keV. It depends on the resolution and efficiency, and also on the presence of material in the vicinity of the active detector region, as these materials may backscatter γ-rays into the detector. It plays a role in the background due to the presence of the source.

- **The Detector Efficiency**

  The efficiency ε_γ is a measure of the probability (expressed in absolute values or in per cent) that a γ-ray of energy E_γ is fully absorbed in the active volume of the detector or, in other words, the probability that it contributes to the full-energy peak. It depends basically on the solid angle Ω under which the source is seen by the detector and on intrinsic factors characteristic of the detector.

4.2.5 Pulse shape

The preamplifier was connected with the detector as mention previously and between the high-voltage filter and the detector are made through the cryostat vacuum feedthroughs within the electronic shield.

The detector element absorbs the energy from an incident gamma ray or x-ray and produces a current pulse whose integral is proportional to the absorbed energy. This pulse is integrated, converted to a voltage pulse, and shaped by the preamplifier.

The shape of the output pulse depend on the position at which the charge carriers are formed within the active volume. The simplest case is that of a very short - range particle, which, to first approximation creates all the electron-hole pairs at one location within the detector. If that location lies within the interior of the active volume, there will be unique and separate collection times for holes and electrons because each species must travel a fixed distance before being collected. If the point of interaction is near either edge of active volume, the observed pulse rise will then be due primarily to the motion of only one type of charge carrier. For charge radiations whose range is not small compared with the active volume, distribution of collection times will result from the corresponding spatial distribution of the points at which holes and electrons are formed. If the orientation of the particle track can change significantly from the event to event, an additional variation in the pulse rise time will be introduced [47].

4.2.6 System calibration

GammaVision-32 is the system provided for Gamma-Ray Spectrum analysis within the detector. The GammaVision offers four analysis engines and three major analysis methodologies. In the primary analysis method, a library-directed peak search delivers lower detection limits than can be achieved by "unguided" peak searches. This method is ideally suited for the determination of low-level and ultra-low-level samples (where statistics might be poor) for a specified list of nuclides. For analysis of true unknowns (e.g., emergency-response samples), an "Auto Isotope Identification" mode allows efficient, accurate use of large libraries while maintaining reasonable analysis times. The interactive re-analysis mode lets you repeatedly re-fit the spectrum while

monitoring the fit residuals. This is invaluable for highly complex spectral analysis such as certain neutron-activation and reactor-coolant spectra. A "directed fit" option report negative activity values if calculated, as required for some effluent analysis requirements. An enhancement to directed fit allows this option to be used in the deconvolution of overlapping peak areas.

The calibration of the system defines four relations:

1. Spectrum channel numbers and energy,

2. FWHM of the peak and energy,

3. Spectrum count rate and activity in becquerels or other units,

4. True coincidence summing factor and energy

These relationships are calculated from spectra, user inputs, and inputs from libraries and tables.

The energy calibration function in the system used for analysis calculates two sets of parameters: the energy vs. channel number, and the peak shape or FWHM vs. energy. The inputs to this function are a spectrum or series of spectra with isolated peaks distributed over the energy range of interest, and either a library or table of peak energies. The formula for energy vs. channel number is:

$$E = a_1 + a_2 C + a_3 C^2 \tag{4.7}$$

where,

E = energy,

a_i = coefficients,

C = channel number.

The formula for FWMH vs. channels is given as following:

$$F = b_1 + b_2 C + b_3 C^2 \tag{4.8}$$

where,

F = energy,

b_i = coefficients.

The calculation of the FWHM in energy, the following equation can be used:

$$F(e) = F(c)(a_2 + 2a_3 \times C) \tag{4.9}$$

where,

$F(e)$ = FWHM in energy,

$F(c)$ = FWHM in channels at channel C,

a_2 = energy calibration slope,

a_3 = energy calibration quadratic coefficient,

C = channel number.

When the FWHM fit is made, the fit is automatically checked for validity. If the FWHM curve is negative at any part of the spectrum or the curve bends over (has a maximum and then goes down), a warning message, Non-physical FWHM fit, is displayed in the system monitor.

Energy calibration setup

The first step in the calibration was carried out by collected a spectrum of a multi-gamma standard solution. The spectrum peaks was been well-defined with a small statistical uncertainty. The system of spectroscopy provide automatic calibrate program to perform a complete energy and FWHM calibration on the displayed spectrum using the working library as mention above. The simplest form is the linear relationship between the two quantities.

Efficiency calibration

The efficiency calibration function calculates the detection efficiency of the HPGE detector system as a function of energy. The efficiency of the detector system is the relation between the number of gamma rays emitted from the source to the number of gamma rays collected in the full-energy peak. Various kinds of efficiency definitions are in common use for gamma ray detectors:

- Absolute Efficiency:

  The ratio of the number of counts produced by the detector to the number of gamma rays produced by the source (into all directions). This depending upon the source-to-detector distance.

- Intrinsic Efficiency:

  The ratio of the number of pulses produced by the detector to the number of gamma rays striking the detector.

- Relative Efficiency:

  Efficiency of one detector relative to another; commonly that of germanium

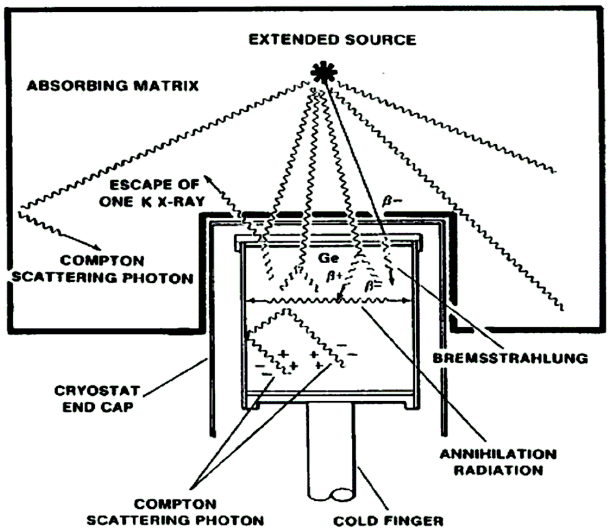

Figure 4.4: Detector with Extended Source.

detector relative to a 3 in diameter by 3 in long Nal crystal, each at 25 cm from a point source, and specified at 1.33 MeV only.

- Full-Energy Peak Efficiency:

  The efficiency for producing full-energy peak pulses only, rather than a pulse of any size for the gamma ray.

The HPGE detector system efficiency includes effects from the detector itself, the detector source geometry, the materials surrounding the detector, and absorption in the source material or matrix (Fig. 4.4 present these effects).

In general, it is not good practice to use efficiency calibrations from one detector-source geometry for other geometries. Since the efficiency is defined as a function of energy, the energy calibration must be done first.

The relative efficiency measurement was performed using multigamma standard solution provided by LEA Laboratories, France. The Multigamma standard solution has volume of 5 cm^3 and density equal 1.016 $g.cm^{-3}$. The reference activity date of the solution was been on 29 Oct 2007 and Table 4.3 present the radionuclides and activity concentration of the solution.

The energy-calibrated spectrum of the radionuclides and their source strengths and calibration date are entered into GammaVision in convenient menu-type forms.

The ratio of relative Efficiency expressed by the following equation:

$$\textit{Relative Efficiency} = \frac{(\textit{peak area})/[(\textit{activity})(\textit{live time})]}{1.2 \times 10^{-3}} \times 100 \tag{4.10}$$

where,

peak area = number of counts in peak,

activity = disintegrations/second,

live time = real time minus total system dead time in seconds.

There are several options provide by the detector system for the type of fit used to describe the efficiency energy relationship. These are:

1. Interpolative fit.

2. Linear fit of the natural logarithm of the efficiency to the natural logarithm of the energy.

3. Quadratic fit of the natural logarithm of the efficiency to the natural logarithm of the energy.

4. Six-order Polynomial fit of the natural logarithm of the efficiency to the energy.

Table 4.3: Summary of nuclides of Multigamma standard solution (as was provided by manufacturer brochure attached to the shipment).

Radionuclide	Half life	Energy (keV)	Number of photons per 100 disintegrations	Activity concentration ($kBq.g^{-1}$)
Am-241	432.6 y	59.54	35.78	1.93
Cd-109	461.4 d	88.033	3.63	9.13
Co-57	271.8 d	122.06	85.51	0.494
Co-57	271.8 d	136.47	10.71	
Ce-139	137.641 d	165.86	79.9	0.469
Cr-51	27.703 d	320.08	9.87	19.1
Sn-113	115.09 d	391.69	64.97	2.92
Sr-85	64.850 d	514	98.5	1.58
Cs-137	30.05 y	661.66	84.99	2.84
Co-60	5.271 y	1173.23	99.85	2.9
Co-60	5.271 y	1332.49	99.98	
Y-88	106.626 d	898.04	93.9	2.86
Y-88	106.626 d	1836.05	99.32	

5. TCC Polynomial, a different six-order polynomial fit of the natural logarithm of the efficiency to the natural logarithm of the energy.

Options 1, 2, and 3 can be selected separately for two separate energy regions. Either of the two regions might be left uncalibrated by not including any points in the region, but the analysis will report zero intensity (in the library peak output) for peaks in the uncalibrated region. If both regions are calibrated, the above-the-knee energy region is fitted first, and the calculated efficiency at the knee is included as a data point in the below-the-knee fit. This means that only one point need be below the knee, but two points are the minimum above the knee for a calibration to be done. Option 4 fits the entire energy range with one function and is best suited to p-type detectors. Option 5 fits the entire energy range with different functions over three energy regions and can be used for p- or n-type detectors.

An efficiency standard table file contains all the data needed using the standard source was created by the system. Fig 4.5 present the efficiency curve and the generated table contains the following information (by columns):

1. Isotope name (same as library).
2. Gamma-ray energy (keV).
3. Efficiency (used for manual efficiency inputs, ignored if remainder of line is valid).
4. Activity in Bq or μCi at the date and time specified in column 7.
5. Gammas/sec for this energy, at the specified date and time.
6. Uncertainty for this nuclide.

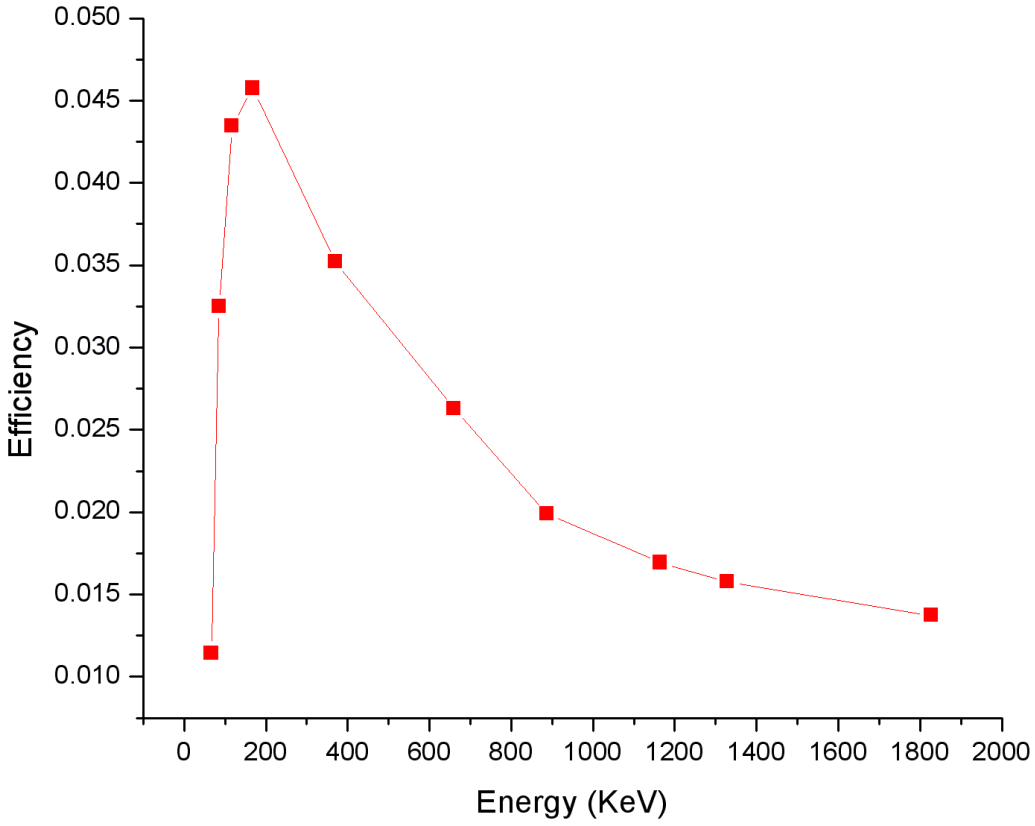

Figure 4.5: The efficiency calibration curve.

7. Calibration date and time for the gammas/sec calibration. The gammas/sec are automatically decay corrected from the date/time in column 5 to the date/time of the spectrum acquisition.

8. Half-life of this nuclide in days.

9. Branching ratio as gammas/100 disintegrations.

Calculation details for peaks

For all library peaks in the analysis energy range, the program attempts to calculate the net peak area and centroid of a peak at that channel. At this step in the analysis, each peak is considered to be a singlet. A singlet is a single, isolated peak; that is, it is far enough away from other peaks in the spectrum so that the spectrum is background on both sides of the peak (does not overlap another peak). The steps are to calculate the background, then the net area, then the centroid.

Background calculation methods

Using our detector system, we can select the method from among these types: automatic, 5-point average, 3-point average, and 1-point minimum.

The first pass background was calculated on the low-energy side of the peak, the 5-point average of the channel contents was calculated for the region from the peak-centroid channel to the channel which is 6 times the library match width (normally 0.5) times the calculated FWHM (from the calibration) below the centroid. The 5-point average data at a given point is the sum of the data from two channels below the point to two channels above the point divided by 5. This is the same as smoothing the data with a smoothing width of 5 and coefficients of 0.2 for all points.

The background value is the minimum value of the moving 5-point average and the background channel number is the center channel of the 5. If the minimum average value is within one sigma (counting statistics) of the actual channel value at the assigned channel point, this 5-point average is the low energy background value for this peak. If the average value is not within one sigma of the actual data, a 3-point average is used instead of the 5-point average to calculate a new minimum

value. This 3-point average minimum value is compared with the actual data at the assigned channel and is accepted if it is within 1 sigma of the actual data. If the 3-point average also fails this test, the data value at the assigned channel is used for the background.

The same process was repeated for the high-energy side of the peak to calculate the background value above the peak. The background under the peak is the straight line between these two values.

The net peak area and background are calculated from this first pass. Next, the width was reduced or increased depending on the peak-area-to-background ratio and the library match width. This adjustment makes two improvements: (1) it reduces the number of channels in the peak for small peaks (decreasing the uncertainty), and (2) it improves the area calculation for peaks moved from the library energy. This background calculation method has advantages, when there are closely spaced peaks, over other methods. For example, because the 1-point method will be used when a small peak is very near a large peak, a more accurate measure of the background will be obtained as compared to the 5- or the 3-point average.

The background of the small peak is less affected by the other peak because the automatic method will tend toward the smaller values. The background area A_b was calculated by GammaVision software using the following equation:

$$A_b = \frac{B_l + B_h}{2} \times W \tag{4.11}$$

where,

B_l = the background on low side of peak,

B_h = the background on high side of peak,

W = the peak width.

In addition the background error ,A_{er}, and net area error ,A_{net}, calculated by GammaVision software using equations 4.12 and 4.13 respectively as following:

$$A_{er} = (\frac{A_b \times W}{W_l + W_h})^{1/2} \tag{4.12}$$

$$A_{net} = \sqrt{G_{er}^2 + A_{er}^2} \tag{4.13}$$

where,

G_{er} = the gross area error = square root of gross area,

W_l = the width of low average,

W_h = the width of high average.

The background was measured routinely to check the presence of any contamination. The system was cleaned routinely using cotton wool and alcohol for any other measurements perform in the system. To avoid the surface contamination of the samples with the detector and increase the leakage current from it, we placed the sample in plastic pack.

4.2.7 Activity calculation

The nuclide activity (in becquerels or curies), based on the peak at energy, E, is given by the following equation:

$$A_{Ei} = \frac{N_{Ei}}{\varepsilon_E \times t \times \gamma_d} \tag{4.14}$$

where,

A_{Ei} = the activity of nuclide i based on energy E,

N_{Ei} = the net peak area for peak at energy E,

ε_E = the detector efficiency at energy E,

t = the livetime,

γ_d = the gammas/disintegration for energy E of this nuclide.

This "peak activity" was reported in the nuclide peak matrix. If there is more than one peak in the energy analysis range for a nuclide, then an attempt to average the peak activities is made. The result of the average is the average nuclide activity.

The average activity for the nuclide is calculated by first doing a gammas/disintegration weighted average of the first and second library peak activity, if the activity of the second peak is within two times the uncertainty of the first peak activity. The uncertainty in the first peak activity includes counting uncertainty of the first peak, uncertainty in the library entries, and uncertainty in the calibration. Subsequent peaks are likewise included in a running average if their activity is within two times the uncertainty of the current average activity (A_{AVE}). That is:

$$A_{AVE} = \frac{\sum_{i=1}^{n} I_i}{\sum_{i=1}^{n} G_i} \tag{4.15}$$

where,

I_i = the corrected (for all factors) intensity of the ith peak,

G_i = the gamma/disintegration of the ith peak,

n = the number of peaks included in the activity.

4.2.8 Minimum detectable activity

The Minimum Detectable Activity (MDA) is a measure of how small an activity could be present and not be detected by the analysis. There are many factors affecting the MDA, which is reported in activity units such as becquerels. The calibration geometry, the backgrounds (system and source-induced), the detector resolution and the particular nuclide all substantially affect the MDA reported. Except for the MDA formula chosen and the sensitivity threshold, the MDA is not affected by the analysis software.

For all peaks, the MDA value is calculated based on the background value of the peak. If the peak area was not used in the activity calculation because it failed the sensitivity test, or a shape test, the peak area is added to the background for the MDA calculation unless the MDA defines the background separately. If the background is 0, it is set to 1 for the MDA calculation. The background will still be reported as 0 on the report. By reviewing the individual MDA values (which are printed on the nuclide/peak matrix) we can determine how relevant the selected MDA value is to the physical situation. The MDA reported for the nuclide is the value for the first peak in the library.

The MDA reported might be any one of the following MDA formalisms. The type used was printed on our report. In the following definitions, the peak count and peak count rate are calculated according to the various formulas. These are then converted to an MDA with all the corrections performed for the relevant library peak.

- **Method 1 - Traditional ORTEC**

  The peak count is equal to the square root of the sum of twice the uncertainty in the background and 2500 over the sensitivity squared plus 50 over the sensitivity,

all multiplied by 100 over the sensitivity. The peak count rate is the peak count divided by the live time.

$$Peak\ Area\ Rate = \frac{\frac{100}{SENS} \times \sqrt{2 \times BKG + \frac{2500}{SENS^2}} + \frac{50}{SENS}}{LiveTime} \tag{4.16}$$

where,

$SENS$ = the user-set sensitivity in percent (peak cutoff),

BKG = the peak background,

$LiveTime$ = the spectrum live time.

- **Method 2 - ORTEC Critical Level**

  The critical level is 2.33 times the square root of the background. If the peak area exceeds this level, bit 2 of the nuclide flag is set to 1.

- **Method 3 - Suppress MDA Output**

  The MDA is not calculated and is set to 0.0. For nuclides not present, there is no printout on the nuclide report. The individual peaks are included in the other parts of the report.

- **Method 4 - KTA Rule**

  The peak count is equal to the square root of average channel contents in a region equal to 2.5 times the calculated FWHM times the number of channels in the FWHM. This value is scaled by the sigma value of 1, 2, or 3 and divided by the live time to give the peak count-rate ,P, sigma for the selected value.

$$P = \frac{(\sqrt{B \times W}) \times \sigma}{LT} \tag{4.17}$$

where,

B = average background/channel at peak energy,

W = FWHM in channels,

σ = confidence level (1, 2, or 3).

4.2.9 Correction

Decay during acquisition

The decay during acquisition correction is used to correct the activity of nuclides whose half-life is short compared to the spectrum real time. The correction performed using the following equation:

$$DDA = \frac{ln\,2 \times \frac{Real\,time}{half\,-life}}{1 - e^{-(ln2 \times \frac{Real\,time}{half\,-life})}} \tag{4.18}$$

where,

DDA = the decay correction factor,

$Real\,time$ = the spectrum real time,

$half\,-life$ = the half-life of the nuclide of interest,

$ln2$ = the natural log of 2.

This can be viewed as scaling up the activity measured to the value of the activity at the start of the measurement. The correction goes to 1 (no change) as acquisition time becomes much smaller than the half-life. The decay during acquisition technique is superior to making use of a hardware dead-time correction. For example, suppose a sample contains two nuclides, one with a short half-life and one with a long half-life. The count rate of the short half-life nuclide will be higher at the beginning of the count time than at the end of the count. This means more counts per unit time will be accepted at the beginning of the count time than at the end. So even if the count

time is extended by the hardware to compensate for the lost counts at the beginning of the counting period, the count rate is so low at the end of the count that not enough counts will be added in. For the long half-life nuclide, the count rate does not change during the count time, so the livetime correction will correctly account for the lost counts during the count time.

Decay correction

If the half live of the radionuclide is short as in our case, decay correction are necessary. The decay correction projects the activity at the time of count back to the time the sample was collected. If the time is greater than 12 half-lives, the correction is not made and the message is printed out. Twelve half-lives corresponds to a decay factor of about 4000. Both the time of count and decay-corrected values are presented on the report. The total activity was the decay-corrected activity.

Decay During Collection (DDC)

If the sample was collected over an extended time, this correction will account for the buildup or increase of activity in the sample during the collection time. The correction is given by:

$$DDC = \frac{ln2 \times \frac{Elapes\,time}{half-life}}{1 - e^{-(ln2 \times \frac{Real\,time}{half-life})}} \tag{4.19}$$

Peaked Background Correction (PBC)

The PBC is used to correct for the presence of an isotope in the background spectrum that also occurs in the sample. If the isotope is not of interest in the analysis results,

there is no need to make this correction. The correction subtracts peak counts in the background spectrum from the peak counts in the sample.

The PBC values in the PBC table are the counts-per-second at each library energy and these values are subtracted from the counts-per-second values of the sample spectrum before the above corrections. The PBC value is added to the background and the new error is calculated by multiplying the percent error by the ratio of the uncorrected area to the corrected area.

This method improves on older PBC methods because the peak count rates are stored in the PBC table for each energy in the spectrum and not the average rate for an isotope. This removes the dependence on the efficiency calibration in the PBC table, yielding more accurate results because the nuclides in the background are not in the same geometry as the sample, meaning that the efficiency calibration is not the one to be used.

The subtraction of the PBC area and the recalculation of the percent error can result in the new net peak area being below the sensitivity cutoff and thus eliminating this peak from being used in the activity calculation. If the first library peak is rejected, the MDA is reported.

Geometry correction

The geometry correction is used to adjust the activities reported in a sample of a given source detector geometry when the system was calibrated using a different source-detector geometry.

This is useful when many different geometries are used in a laboratory and calibrated sources are not available for all the geometries used.

The correction factor multiplies the peak intensity for each peak in the library as shown in equation 4.20. The factors are stored as a function of energy.

$$A_C = A \times GeoFac \tag{4.20}$$

where,

A_C = corrected intensity for a given energy,

A = uncorrected intensity for a given energy,

$GeoFac$ = the correction factor for that energy.

The correction is not applied to unknown peaks. The peak values in the isotope/peak list in the output report are uncorrected values. The peak uncertainty is maintained as a constant percentage. The factor is linearly interpolated between the points in the table and linearly extrapolated outside the energy range of the table points.

As an example of the geometry correction, two spectra were taken of the same point source (see Fig. 4.6). In case 1, the source was about 4 cm from the end cap and on-axis of the detector. The second geometry (case 2) is with the source about 7.5 cm from the center of the detector in a position in the plane of the end cap of the detector.

The ratio of the peak count rates between case one and two are entered into the geometry table.

Random summing

If more than one gamma-ray photon signal is absorbed by the detector during a pulse sampling cycle, the sum of the energies of the two (or more) is recorded in

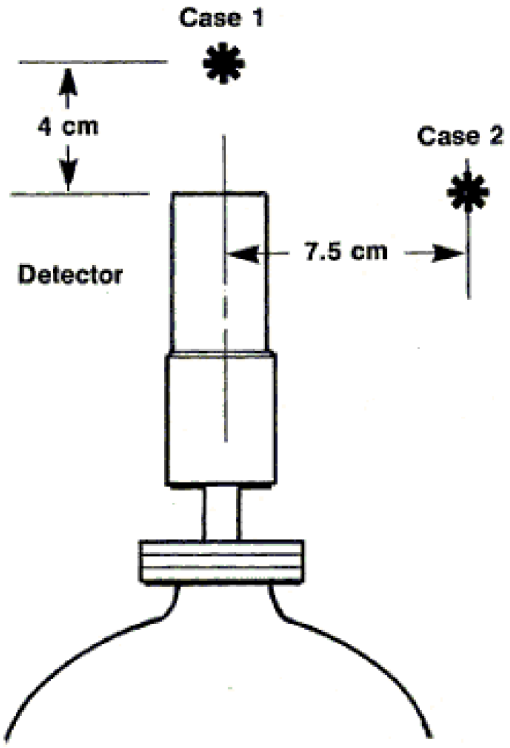

Figure 4.6: An example of the geometry correction.

the spectrum. Since the two gamma rays are not related in any way, this is random coincidence. Random coincidence sum peaks can be formed at double the energy of the primary peaks. Any full-energy photon that is summed with another pulse is not recorded in the single photon peak and represents a loss of counts or efficiency. This loss is count-rate dependent.

The random summing correction factor (RSF) was calculated using the following equation:

$$RSF = \frac{1}{1 - \frac{\sum Ct}{F \times T_l}} \tag{4.21}$$

where,

Ct = the contents of all channels,

F = the user-entered slope of the correction curve,

T_l = the live time.

4.2.10 Reported uncertainty

The uncertainty which was printed on our reports can be either counting or total uncertainty. The counting uncertainty is the uncertainty of the peak area due to statistical uncertainty. For a peak net area, the counting uncertainty can be expressed in percent of the peak area. This same percent is used to express the percent counting uncertainty in the activity values.

The total uncertainty value ,σ_t, is composed of the random and systematic errors in all of the factors involved in producing the final nuclide concentration result. The error is given by the following equation:

$$\sigma_t = \sqrt{\sum \sigma_{ri}^2 + 1/3 \Sigma \sigma_{si}^2} \tag{4.22}$$

where,

σ_{ri} = the individual random error.

σ_{si} = the individual systematic error.

The random uncertainties are: counting, additional, random summing, and absorption correction. While the systematic uncertainties are: nuclide uncertainty from library, efficiency fitting uncertainty from calibration, calibration source uncertainty, geometry correction, and additional.

The random summing uncertainty is estimated to be 10% of the square root of the correction. The efficiency uncertainty, both above and below the knee is calculated in the calibration section program. These values are printed on the calibration report.

The calibration source uncertainty we have entered was the 1-sigma uncertainty in the source values used in the efficiency calibration. This value was usually supplied with the calibration standard. It is the uncertainty calculated by the supplier for the values given for the standard.

Table 4.4 and 4.5 present the summary about correction used and setup of GammaVision software parameters respectively.

4.2.11 Reference experimental setup

All experiments were conducted using an electron linear accelerator manufactured by Varian Company "Clinac 2100C" and producing 6 and 15 MV photon beams. The air inside the treatment room were activated by means of 15 MV and dose of 400 MU was delivered for 10 x 10 cm^2 field size. The point of interest ,A, was used in our experiments shown in Fig 4.1. After the end of delivering the dose we enter the treatment room quickly and start the air pumping process (air pollution monitoring)

by power on the vacuum pump which including the filter paper at the interest point. Setup of this measurements was shown in Fig 4.7.

Whatman filters (filter papers) are manufactured from high quality cotton linters which have been treated by manufacture to be used for general filtration and exhibit

Table 4.4: Summary about correction used by GammaVision software

Corrections	Status
Decay correct to date	YES
Decay during acquisition	NO
Decay during collection	NO
True coincidence correction	NO
Peaked background correction	NO
Absorption (Internal)	NO
Geometry correction	NO
Random summing	YES

Table 4.5: Summary of setup GammaVision software parameters.

Error	Values
Random error	1.00E+00
Systematic error	3.00E+00
Fraction Limit	0.000
Background width	best method (based on spectrum)
Half lives decay limit	12
Activity range factor	2
Min. step backg. Energy	0

Figure 4.7: Filter paper and vacuum pump device setup in the linear accelerator "Clinac 2100C".

particle retention levels down to 2.5 μm.

The unique features of these filters make them the optimum choice for many filtering techniques. The filters are tested by manufacture for basis weight, thickness, air flow and mechanical strength. Air inside the treatment room (radioactive dust) is collected from airflow of vacuum pump and the filter paper was quickly removed from the treatment room and the radionuclides of air have been identified by their half lives using gamma spectrometer.

Before starting our routine daily measurements, we monitored the background exposure rate for possible abnormally high residual activity in the treatment room using calibrated ionization chamber survey meter (Model 450P, Victoreen, Inc.; Cleveland, OH).

In order to minimize the influence of the accumulated induced activity on our measurements and according to routine daily clinical work most experiments carried out in early morning hours of Friday and Monday before the routine daily clinical work began on the machine.

4.3 Portable Spectrometer method

The type of portable spectrometer used in our experiment is Intrinsic Germanium Coaxial Detector p-Type. The detector type is PR6C1519 and the crystal diameter is 57 mm. The other technical specifications can be shown in Table 4.6. Fig 4.8 shows the components of Intrinsic Germanium Coaxial Detector p-Type.

The ratio of the absolute germanium detector efficiency to a 3 x 3 NaI (TI) scintillation detector was calculated. The ratio expressed as a percentage, is given as the relative efficiency of the detector as mentioned in equation 4.10.

Table 4.6: Technical specifications of portable spectrometer.

Specification	**Values**
Detector Model	PR6C1519
Crystal diameter	57 mm
Crystal length	33 mm
Crystal volume	76 cm^3
Detector window distance	10 mm
Leakage current	< 50 pA
Relative efficiency using Co-60	3.9 %

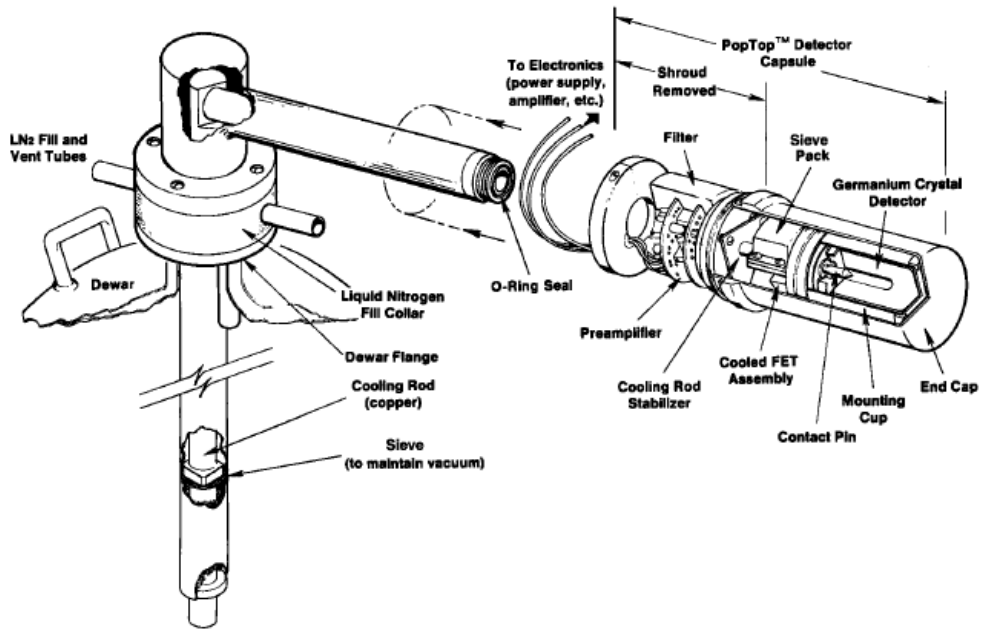

Figure 4.8: The components of Intrinsic Germanium Coaxial Detector p-Type.

4.3.1 Experimental setup

The main part of the experimental work consisted in the usage of a portable high resolution gamma spectrometer, consisting of a high purity germanium detector (PR6C1519, SILENA, USA, 10% relative efficiency, FWHM = 1.82 keV at 1.33 MeV) and battery-driven spectrometer hardware. An energy-dependent efficiency calibration of the detector had been obtained previously by acquiring a spectrum from two calibrated point sources containing ^{133}Ba and ^{152}Eu. The sources had been placed at 1 m distance vertically from the detector and perpendicular to the detector surface. Fig 4.9 shows the typical experimental setup.

The spectrometer was installed on the patient table inside the treatment room of Varian Clinac 2100C. The accelerator was programmed according to our reference and relative experimental setup to deliver various monitor units (MU) (400-20000 MU) using high energy photon beam (15 MV) at the maximum output rate (240 MU/min) and a gantry angle of 0 degree. The sensitive volume of the detector was placed at the isocenter of the linac at point A (see Fig 4.1) and put in operational mode as quickly as possible after the termination of the beam. The geometry of machine provides a focus-isocenter distance (FID) of 100 cm.

The time span between termination of the beam and start of the recording of the first spectrum was around 2 minutes, depending on the local situation. The field size during and after irradiation was set to 10 x 10 cm^2, assumed to be an average treatment field size. Spectra were collected during 2 hours and for varying times: 1 min in the first part of the experiment, increasing to 15 min in the later part. These experiments were done on Friday afternoons directly after the end of the weekly clinical routine. Two days later, one or several spectra were collected in the

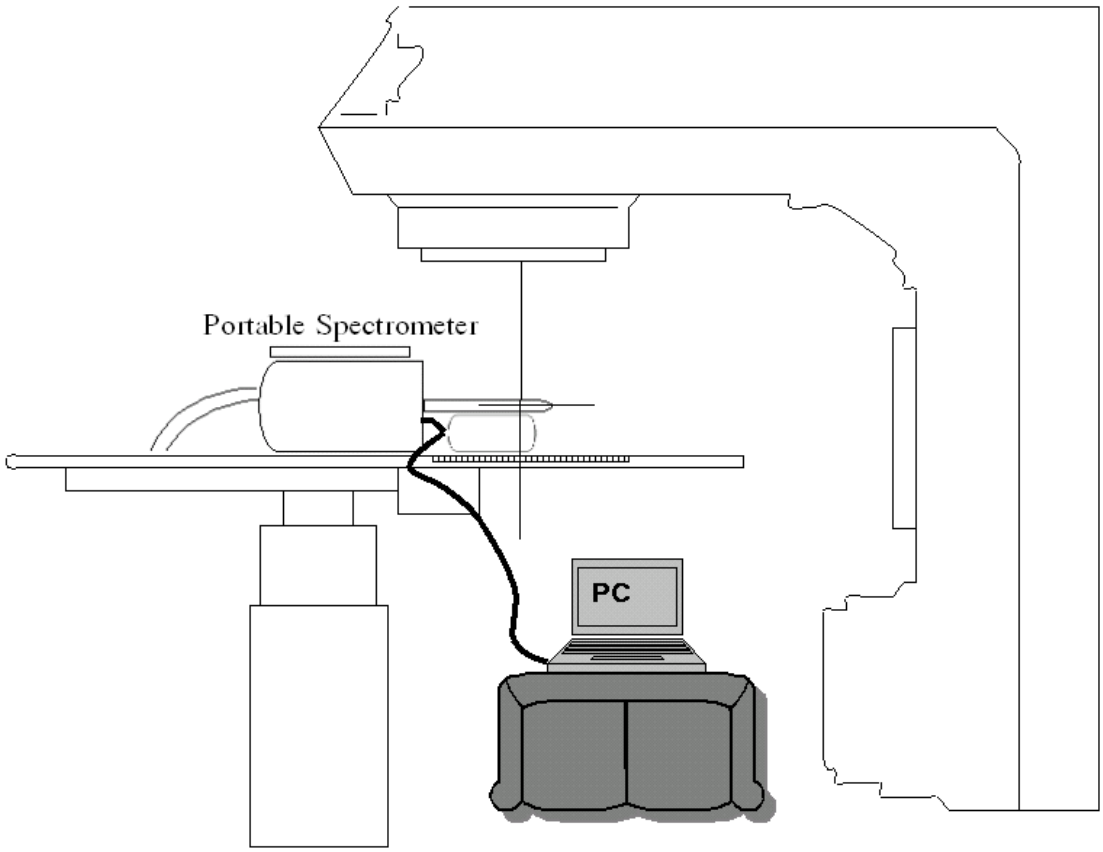

Figure 4.9: Experimental setup of Intrinsic Germanium Coaxial Detector p-Type.

same geometry and for longer times, in order to identify longer-lived radioisotopes after decay of the shorter-lived ones. The accelerators were not used and left in the stand-by state between the two measurement cycles.

4.4 Mathematical model

From section 3.2 of chapter three, the number of nuclide of each of activation and decay process at any time t can be obtain by solving a system of differential equations (see Appendix A) that relates each product. The activation and decay process of nuclides can be represented by the following relationship:

$$N_1 \rightarrow N_2 \rightarrow N_3 \tag{4.23}$$

In medical linear accelerators the stable parent nuclide, P, transformed through activation process of neutron or photons to radioactive nuclide, T. This radioactive nuclide decay into a granddaughter nuclide through ,G, internal conversion by emits photon, neutron or beta. The activation and decay process of nuclides can be represented by the following relationship:

$$P \rightarrow T \rightarrow G \tag{4.24}$$

After solving the system of differential equations, the activation dose rate, $\dot{D}_c$, at decay time , t, can be given by

$$\dot{D}_c = \dot{D}_m(1 - e^{-\lambda t_r})e^{-\lambda t} \tag{4.25}$$

where $\dot{D}_m$ is the dose rate, which represents the maximum dose rate, given as the dose rate $\dot{D}_c$ when the activation time t_r approaches infinity.

Due to the radionuclides with long half-lives, the activity will build up during the five working days and then decrease somewhat over the weekend. In addition, if we want to calculate all dose rate of radioactive nuclides and we assume there is n species of radionuclides produced in linac room, then equation (4.25) can be given as the sum of all possible radioactive transformation, i.e.,

$$\dot{D}_c = \sum_{i=1}^{n} (\dot{D}_m)_i (1 - e^{-\lambda_i t_r}) e^{-\lambda_i t} \tag{4.26}$$

where $(\dot{D}_m)_i$ and λ_i are the maximum dose rate and decay constant, respectively, for the nuclear species i.

If we want to calculate the activation dose, D, for 5 days, equation (4.26) can be written as follows:

$$D_c = \sum_{i=1}^{n} (\dot{D}_m)_i (1 - e^{-\lambda_i t_r}) e^{-\lambda_i t} .5 \ \ days \tag{4.27}$$

The activation dose rate due to the radionuclides with long half-lives at the isocenter of Clinac 2100C linac after irradiation can be approximated as follows:

$$\dot{D} = \dot{D}_B + \dot{D}_C \tag{4.28}$$

where $\dot{D}_B$ is the background dose rate in linac room and $\dot{D}_C$ is the total dose rate calculated as the sum of all dose rate from radionuclides with long half-lives, that is contribute to most of the induced activity at the point A (see Fig 4.1) of Clinac 2100C linac.

4.5 Monte Carlo simulation

Geant4 as one of Monte Carlo simulation codes was used in this study to estimate the equivalent dose due to induced activity received by technologist and patients. The induced activity commonly comes from the photodisintegration and neutron capture reactions as mentioned before. In the photodisintegration or photoneutron reaction, the target nuclide producing a neutron and daughter nuclide, the resulting nucleus (daughter nuclide) may be radioactive and may subsequently undergo β^+ and γ decay. Similarly, as a result of neutron capture, the target nucleus transforms into new nuclide that may be radioactive and may subsequently decay through β^- and γ decay.

Our work on the simulation of Clinac 2100C activation problem was focused on the determination of equivalent dose received by technologist from neutron produced by photodisintegration reaction and estimation of equivalent dose variation due to relative measurements setup explained in section 4.1.

4.5.1 Geant4 overview

The acronym 'Geant' was invented in the 1970's to name a code that simulated 'Ge'ometry 'an'd 't'racking for particle physics experiments. The first widely-used released version of the code, GEANT3, was written in FORTRAN and used several, at the time well-established, physics routines to model the physics of the interactions. As the complexity of the code kept increasing, object-oriented techniques were opted for instead, as this seemed to be the most efficient way to maintain the transparency of the code without compromising its performance. At that point it was also decided that the program would be given the form of a toolkit allowing the user to easily

extend the components of all domains. This new phase of development led, in 1998, to the first production release of Geant4 [11], a C++ program that nowadays begins to be adopted by fields other than particle physics, such as space science and medical physics [18].

A Geant4 simulation run can be thought of as proceeding through the following steps (schematically shown in the appendix B):

- the particles to be used are specified,
- the processes a particle is allowed to undergo are specified,
- the model describing each process is chosen,
- the materials to be used in the run are defined,
- the geometry of the system is defined,
- materials are assigned to the components of the geometry,
- external electromagnetic fields are defined,
- the geometry of the detectors is defined,
- the primary events are generated (by e.g. an interface to an event generator),
- the primary particles are transported through the system and the production of secondary particles is simulated as they interact with matter,
- the event data (as 'measured' by the 'detectors') are stored for further analysis (e.g. in the form of histograms).

In the present application, there are no external electromagnetic fields. The remaining components of the simulation are discussed in the following sections.

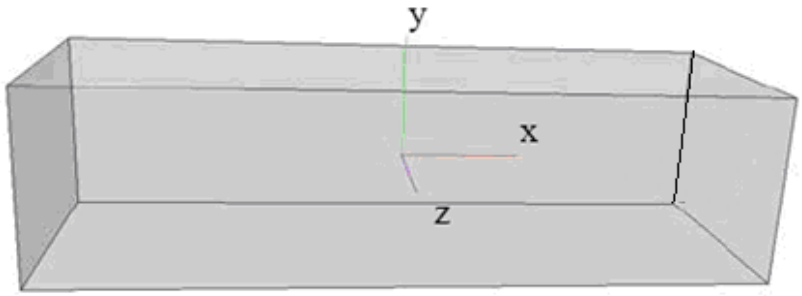

Figure 4.10: Example of a geometry in Geant4. The axes of the internal reference system are shown.

4.5.2 The definition of the geometry

There are two landmarks used in defining the geometry of the setup in Geant4: the 'World' volume and the internal reference frame of the simulation. The 'World' volume is conceived as the volume that includes all the three-dimensional space that the simulation has to consider. The internal reference frame of Geant4 is a Cartesian system that has its origin at the center of the 'World', as shown in Fig 4.10. Each component of the system is defined as a geometrical volume whose center is placed at a point in the reference frame of another volume.

When all volumes are thus placed, they are assigned materials. These are defined as elements or compounds. Compounds are defined by their atomic composition as given by a chemical formula or weight fractions, their density at a given temperature and pressure and their mean excitation energy. Example of geometries for our simulation and for the head of linear accelerator 2100C, are shown in Fig 4.11.

In general, the term 'geometry' in Geant4 refers to the volumes built in the simulation, whether these are sensitive components registering hits or merely pieces of

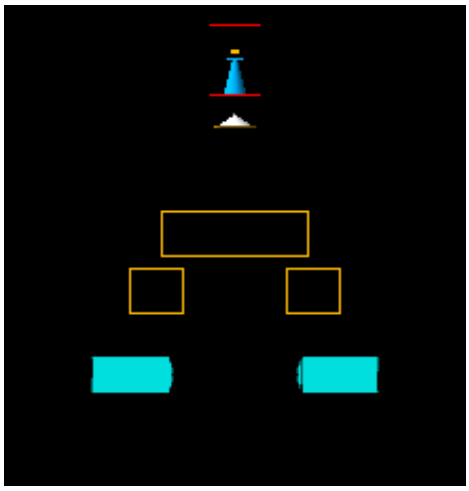

Figure 4.11: Example of geometries for head of linear accelerator 2100C in Geant4.

material the particles traverse. The part of the system that generates the primary particles is not included in the 'geometry' definition but in the 'primary event definition'.

In the present application, the geometry consists of a air sample volume "detector" whose components percentage shown in Table 4.7. The geometry of air sample volume can be shown in Fig 4.12 as sphere. In other hand the x and y jaws, scatter foil, target, multileaf collimator (MLC) and flattening filter are represent the geometry of Clinac 2100C head as shown in Fig 4.13. In addition Fig 4.14 show the hole geometries including the room volume.

4.5.3 Generating the primary events

This part of the simulation consists in defining the initial state of the simulation, i.e. the 'primary particles'. Once this is done, Geant4 will track the particles through the system (following the definition of physics processes) until they stop, decay or are

Table 4.7: The percentage of Air Abundances of the most prominent stable nuclides in the atmosphere at sea level.

Temp (C^0)	**Air density** (**kg/m**^{3})	^{14}**N**	^{16}**O**	^{40}**Ar**	^{15}**N**	^{18}**O**
				(%)		
25	1.184	78.16	20	0.467	0.29	0.04

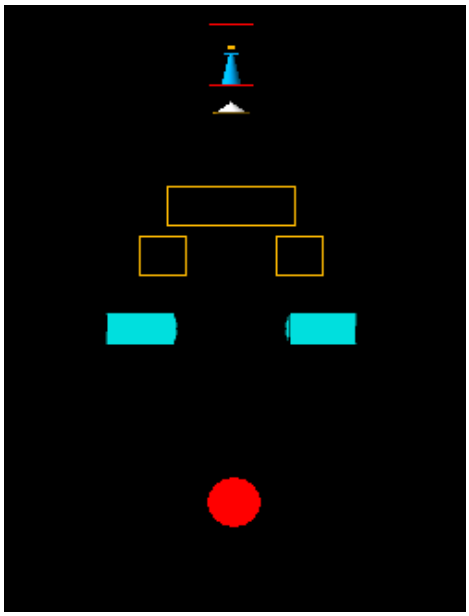

Figure 4.12: The geometries for head of linear accelerator with air sample volume shown as sphere in Geant4.

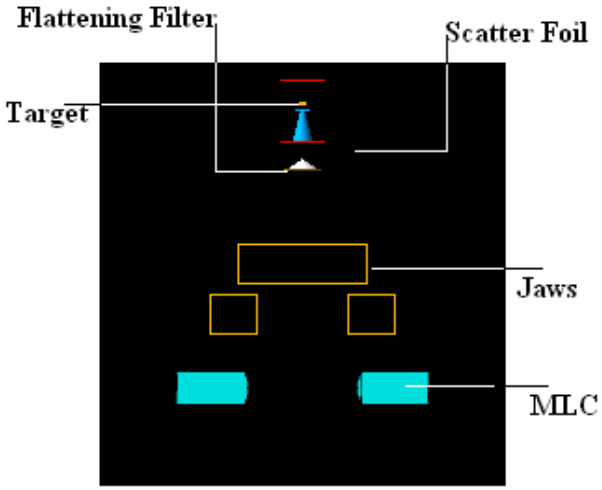

Figure 4.13: The details of geometries for head of linear accelerator (Clinac 2100C) in Geant4.

transported beyond the limits of the World.

The generation of the primary event can be done using an interface to an event generator or the particle gun class, which creates a beam of particles by defining their type, position, direction of motion and kinetic energy. The generation of the primary event in the present application was done by using the latter option.

Our primary particles was assumed to be electrons hit the target of Tungsten with options for users to select there kinetic energies.

4.5.4 Electromagnetic physics

The simulation proceeds by steps and the purpose of the implementation of the physics is to decide where these steps take place and which interactions are to be invoked at

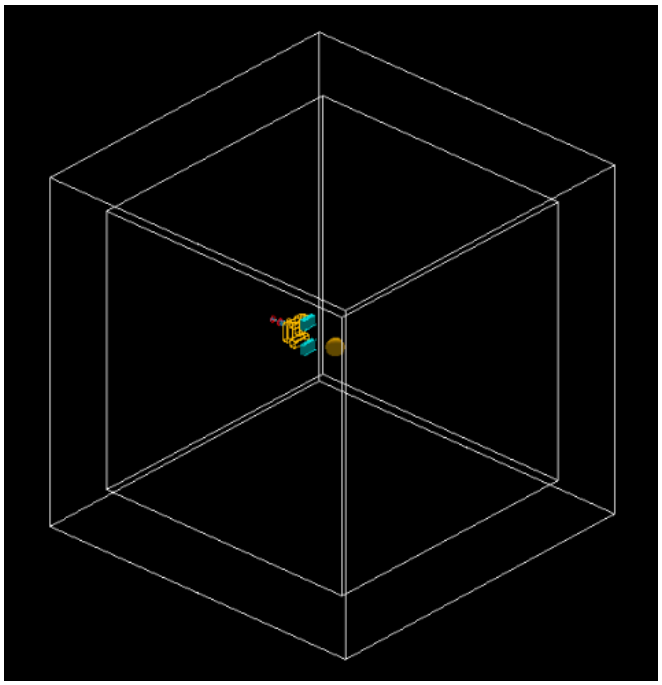

Figure 4.14: Geometry of Clinac 2100C head in the treatment room are shown using OpenGl visualization driver.

each step. This is done by using pseudorandom numbers which are uniformly distributed in the interval (0,1) to calculate the 'mean free path' or 'interaction length' for each interaction that the particle is allowed to undergo. The interaction that proposes the shortest mean free path is chosen. The step length can also be restricted to preserve precision or to prevent the particle from crossing a boundary in the geometry in a single step.

The processes taken into account in the present application were the electromagnetic and nuclear reactions, since above energy of 10 MeV electron beam can induce nuclear reactions. There are two models for electromagnetic physics in Geant4: the 'standard' model and the 'low-energy' model. By 'low-energy' is meant the regime below 100 GeV, in which respect both models are, in principle, applicable in the present context. A complete description of the physics used in Geant4 can be found in Geant4 physics reference manual [24]. Overview reports of the physics models and their validation are given literature [55, 56, 57, 58].

4.5.5 Production cuts

Geant4 does not use tracking cuts, i.e. all particles are tracked to zero kinetic energy unless they reach the limits of the World. Photons and secondary electrons are, however, generated only above a given kinetic energy threshold ('production cut-off'). This is done as to avoid the production of a large number of secondary particles, which would deteriorate the performance of the simulation without enhancing the accuracy of the calculations.

In principle, production cuts can be applied to all processes but this is not done in practice. Instead, they are used to restrict only the generation of secondary particles

by ionization and bremsstrahlung. In the present study, all particles, both photons and electrons, are tracked to the end of their path, while the cutoff range for the production of secondary particles was set according to the dimension of the detector geometries employed.

4.5.6 Determination of the interaction point

The mean free path, λ, of a particle for a given process depends on the medium and cannot be used directly to sample the probability of an interaction in a heterogeneous detector. The number of mean free paths which a particle travels is:

$$n_\lambda = \int_{x_1}^{x_2} \frac{dx}{\lambda(x)} \tag{4.29}$$

which is independent of the material traversed. If n_r is a random variable denoting the number of mean free paths from a given point to the point of interaction, it can be shown that n_r has the distribution function:

$$P(n_r < n_\lambda) = 1 - e^{-n_\lambda} \tag{4.30}$$

The total number of mean free paths the particle travels before reaching the interaction point, n_λ, is sampled at the beginning of the trajectory as:

$$n_\lambda = -\log(\eta) \tag{4.31}$$

where η is a random number uniformly distributed in the range $(0, 1)$. n_λ is updated after each step Δx according the formula:

$$n_{\lambda}^{'} = n_{\lambda} - \frac{\Delta x}{\lambda(x)} \tag{4.32}$$

In principle one must use very small steps in order to insure an accurate simulation, but computing time increases as the stepsize decreases. A good compromise is to limit the stepsize in Geant4 by not allowing the stopping range of the particle to decrease by more than 20 % during the step. This condition works well for particles with kinetic energies > 0.5 MeV, but for lower energies it can give very short step sizes. To cure this problem a lower limit on the stepsize is also introduced.

4.5.7 Standard electromagnetic physics

In general, the standard electromagnetic physics model of Geant4 covers the energy range from 10 keV to several PeV and is mainly used for high-energy and nuclear physics applications. In the standard electromagnetic physics model, the photon induced processes are Compton scattering, photon conversion and photoelectric effect. The electron/positron induced processes are ionization, bremsstahlung and positron-electron annihilation. The 'ionization' class for electrons and positrons calculates the continuous energy loss due to ionization and simulates the 'discrete' part of the ionization, i.e. Moller scattering, Bhabha scattering and γ-ray production. The bremsstrahlung class calculates the continuous energy loss due to soft bremsstrahlung and simulates 'discrete' bremsstrahlung.

The multiple scattering model is based on the Lewis theory [70]. This model is a condensed multiple scattering algorithm which is invoked at the end of the step to compute a correction to the mean path length and also the lateral displacement of the track. The model uses functions to determine the angular and spatial distributions

after the step. The functions are chosen as to give the same moments of the angular and spatial distributions as the Lewis theory. Section 4.5.14 explain more details about multiple scattering.

A special case of 'process' in Geant4 is the 'transportation' process. This class is responsible for determining the geometrical limits of a step and handles the crossing of geometric boundaries. It calculates the distance to the next volume in the geometry and proposes this distance as a possible step length in the same way as the physics processes propose the 'physical' step lengths using their cross sections. The transportation process requires that the particle should always stop at a boundary, thus setting an additional restriction on the step length.

4.5.8 Low-energy electromagnetic physics

The low-energy electromagnetic physics package is an extension to the standard physics code and uses shell cross section data rather than their parametrizations (as they are used in the standard model). The model covers the interactions of photons and electrons in materials with atomic number between 1 and 100. This package does not provide a new implementation of processes induced by positrons. They are treated by the same classes as in the standard electromagnetic physics package. The extended classes of the model treat the following interactions: Compton scattering, Rayleigh scattering, photoelectric effect, ionization and bremsstrahlung. Photon conversion has also been implemented with the same methodology for the total cross section calculation as the processes above. The model also provides implementations for atomic relaxation (fluorescence and Auger electrons).

The implementation of all processes is done in two phases: (a) calculation of the

total cross sections and (b) generation of the final state. Both phases are based on data from the following libraries: Evaluated Photon Data Library (EPDL) [71], Evaluated Electron Data Library (EEDL) [72] and Evaluated Atomic Data Library (EADL) [73].

The energy dependence of the total cross section is derived for each process from the evaluated data libraries. Since the libraries provide cross sections for a set of discrete incident energies, the total cross section at a given energy, E, is obtained by interpolation according to the formula [74]:

$$log(\sigma(E)) = log(\sigma_1)\frac{log(E_2) - log(E)}{log(E_2) - log(E_1)} + log(\sigma_2)\frac{log(E) - log(E_1)}{log(E_2) - log(E_1)} \tag{4.33}$$

where E_1 and E_2 are respectively the closest lower and higher energy for which data (σ_1 and σ_2) are available.

For each process a production threshold energy is defined; by default it is set to the low end of the energy validity range of the process (250 eV in the current implementation), but a higher or lower value can be set by the user.

For a particle of energy E, the mean free path for interacting via a given process is calculated as:

$$\lambda = \frac{1}{\sum_i \sigma_i(E).n_i} \tag{4.34}$$

where $\sigma_i(E)$ is the microscopic integrated cross-section of the process considered at energy E, and n_i is the atomic density of the $i - th$ element contributing to the material composition. The sum runs over all the elements of which the material is composed. The cross sections are determined as described in this section.

4.5.9 Compton scattering

When simulating the Compton scattering of a photon from an atomic electron, an empirical cross section formula is used, which reproduces the cross section data down to 10 keV:

$$\sigma(Z, E_\gamma) = P_1(Z)\frac{\log(1+2X)}{X} + \frac{P_2(Z) + P_3(Z)X + P_4(Z)X^2}{1 + aX + bX^2 + cX^3} \tag{4.35}$$

where,

Z = atomic number of the medium,

E_γ = energy of the photon,

$X = E_\gamma/mc^2$,

m = electron mass,

$P_i(Z) = Z(d_i + e_i Z + f_i Z^2)$.

In a given material the mean free path, λ, for a photon to interact via Compton scattering is given by equation 4.41.

The quantum mechanical Klein-Nishina differential cross section per atom is [59]:

$$\frac{d\sigma}{d\epsilon} = \pi r_e^2 \frac{m_e c^2}{E_0} Z \left[\frac{1}{\epsilon} + \epsilon\right]\left[1 - \frac{\epsilon \sin^2\theta}{1+\epsilon^2}\right] \tag{4.36}$$

where,

r_e = classical electron radius,

$m_e c^2$ = electron mass,

E_0 = energy of the incident photon,

E_1 = energy of the scattered photon,

$\epsilon = E_1/E_0$.

Assuming an elastic collision, the scattering angle θ is defined by the Compton formula:

$$E_1 = E_0 \frac{m_e c^2}{m_e c^2 + E_0(1 - \cos\theta)} \tag{4.37}$$

The value of ϵ corresponding to the minimum photon energy (backward scattering) is given by

$$\epsilon_0 = \frac{m_e c^2}{m_e c^2 + 2E_0} \tag{4.38}$$

After the successful sampling of ϵ, the polar angles of the scattered photon with respect to the direction of the parent photon are generated. The azimuthal angle, ϕ, is generated isotropically and θ is defined. The momentum vector of the scattered photon, $\overrightarrow{P_{\gamma 1}}$, is then transformed into the World coordinate system.

4.5.10 Rayleigh scattering

The total cross section for the Rayleigh scattering process is determined using equation 4.33.

The coherent scattered photon angle θ is sampled according to the distribution obtained from the product of the Rayleigh formula $(1 + \cos^2\theta)\sin\theta$ and the square of Hubbel's form factor $FF^2(q)$ [60, 61]

$$\Phi(E, \theta) = [1 + \cos^2\theta]\sin\theta \times FF^2(q) \tag{4.39}$$

where $q = 2E\sin(\theta/2)$ is the momentum transfer.

Form factors introduce a dependency on the initial energy E of the photon that is not taken into account in the Rayleigh formula. At low energies, form factors

are isotropic and do not affect angular distribution, while at high energies they are forward peaked.

The sampling procedure is as follows [62]:

1. $\cos\theta$ is chosen from a uniform distribution between -1 and 1
2. the form factor FF is extracted from the data table for the considered element, using logarithmic data interpolation, for $q = 2E \cdot \sin(\theta/2)$
3. if the value obtained for $\Phi(E, \theta)$ is larger than a random number uniformly distributed between 0 and Z^2, the procedure is repeated from step 1, otherwise θ is taken as the photon scattering angle with respect to its incident direction.
4. the azimuthal direction of the scattered photon is chosen at random.

4.5.11 Photoelectric effect

The photoelectric effect is the ejection of an electron from a material after a photon has been absorbed by that material. It was simulated by using a parameterized photon absorption cross section to determine the mean free path, atomic shell data to determine the energy of the ejected electron, and the K-shell angular distribution to sample the direction of the electron.

The parameterization of the photoabsorption cross section proposed by Biggs et al. [63] was used :

$$\sigma(Z, E_\gamma) = \frac{a(Z, E_\gamma)}{E_\gamma} + \frac{b(Z, E_\gamma)}{E_\gamma^2} + \frac{c(Z, E_\gamma)}{E_\gamma^3} + \frac{d(Z, E_\gamma)}{E_\gamma^4} \tag{4.40}$$

Geant4 using the least-squares method, a separate fit of each of the coefficients a, b, c, d to the experimental data was performed in several energy intervals [64].

In a given material the mean free path, λ, for a photon to interact via the photoelectric effect is given by :

$$\lambda(E_\gamma) = \left(\sum_i n_{ati}.\sigma(Z_i, E_\gamma) \right)^{-1} \tag{4.41}$$

where n_{ati} is the number of atoms per volume of the i^{th} element of the material.

The binding energies of the shells depend on the atomic number Z of the material. In compound materials the i^{th} element is chosen randomly according to the probability:

$$Prob(Z_i, E_\gamma) = \frac{n_{ati}\sigma(Z_i, E_\gamma)}{\sum_i [n_{ati}.\sigma_i(E_\gamma)]}$$

A quantum can be absorbed if $E_\gamma > B_{shell}$ where the shell energies are taken from G4AtomicShells data: the closest available atomic shell is chosen. The photoelectron is emitted with kinetic energy :

$$T_{photoelectron} = E_\gamma - B_{shell}(Z_i) \tag{4.42}$$

The polar angle of the photoelectron is sampled from the Sauter-Gavrila distribution (for K-shell) [65], which is correct only to zero order in αZ :

$$\frac{d\sigma}{d(\cos\theta)} \sim \frac{\sin^2\theta}{(1-\beta\cos\theta)^4} \left\{ 1 + \frac{1}{2}\gamma(\gamma-1)(\gamma-2)(1-\beta\cos\theta) \right\} \tag{4.43}$$

where β and γ are the Lorentz factors of the photoelectron.

$\cos\theta$ is sampled from the probability density function :

$$f(\cos\theta) = \frac{1-\beta^2}{2\beta} \frac{1}{(1-\beta\cos\theta)^2} \quad \Rightarrow \cos\theta = \frac{(1-2r)+\beta}{(1-2r)\beta+1} \tag{4.44}$$

The rejection function is :

$$g(\cos\theta) = \frac{1-\cos^2\theta}{(1-\beta\cos\theta)^2}[1+b(1-\beta\cos\theta)] \tag{4.45}$$

with $b = \gamma(\gamma-1)(\gamma-2)/2$

4.5.12 Bremsstrahlung

The class *G4eBremsstrahlung* provides the energy loss of electrons and positrons due to the radiation of photons in the field of a nucleus.

$d\sigma(Z,T,k)/dk$ is the differential cross section for the production of a photon of energy k by an electron of kinetic energy T in the field of an atom of charge Z. If k_c is the energy cut-off below which the soft photons are treated as continuous energy loss, then the mean value of the energy lost by the electron is

$$E^{brem}_{Loss}(Z,T,K_c) = \int_0^{k_e} k\frac{d\sigma(Z,T,K))}{dk}dk \tag{4.46}$$

The total cross section for the emission of a photon of energy larger than k_c is

$$\sigma_{brem}(Z,T,K_c) = \int_{k_c}^{T} \frac{d\sigma(Z,T,K))}{dk}dk \tag{4.47}$$

The cross section and energy loss due to bremsstrahlung have been parameterized using the EEDL (Evaluated Electrons Data Library) data set [66] as input.

4.5.13 Photonuclear reactions

The photonuclear cross sections parameterized in the G4PhotoNuclearCrossSection class cover all incident photon energies from the hadron production threshold upward.

The parameterization is subdivided into five energy regions, each corresponding to the physical process that dominates it.

- The Giant Dipole Resonance (GDR) region, depending on the nucleus, extends from 10 Mev up to 30 MeV. It usually consists of one large peak, though for some nuclei several peaks appear.
- The "quasi-deuteron" region extends from around 30 MeV up to the pion threshold and is characterized by small cross sections and a broad, low peak.
- The Δ region is characterized by the dominant peak in the cross section which extends from the pion threshold to 450 MeV.
- The Roper resonance region extends from roughly 450 MeV to 1.2 GeV. The cross section in this region is not strictly identified with the real Roper resonance because other processes also occur in this region.
- The Reggeon-Pomeron region extends upward from 1.2 GeV.

The cross section in the GDR region can be described as the sum of two peaks,

$$GDR(e) = th(e, b_1, s_1).exp(c_1 - p_1.e) + th(e, b_2, s_2).exp(c_2 - p_2.e) \tag{4.48}$$

The exponential parameterizes the falling edge of the resonance which behaves like a power law in E_γ. This behavior is expected from the CHIPS model, which includes the nonrelativistic phase space of nucleons to explain evaporation. The function

$$th(e, b, s) = \frac{1}{1 + exp(\frac{b-e}{s})} \tag{4.49}$$

describes the rising edge of the resonance. It is the nuclear-barrier-reflection function and behaves like a threshold, cutting off the exponential. The exponential powers p_1 and p_2 are

$$\begin{aligned} p_1 = 1,\, p_2 = 2 \quad \text{for} \qquad & A < 4 \\ p_1 = 2,\, p_2 = 4 \quad \text{for} \qquad & 4 \leq A < 8 \\ p_1 = 3,\, p_2 = 6 \quad \text{for} \qquad & 8 \leq A < 12 \\ p_1 = 4,\, p_2 = 8 \quad \text{for} \qquad & A \geq 12 \end{aligned}$$

4.5.14 Multiple scattering

Geant4 uses a new multiple scattering (MSC) model to simulate the multiple scattering of charged particles in matter. This model does not use the Moliere formalism [67], but is based on the more complete Lewis theory [68]. The model simulates the scattering of the particle after a given step, and also computes the path length correction and the lateral displacement.

MSC simulation algorithms can be classified as either "detailed" or "condensed". In the detailed algorithms, all the collisions/interactions experienced by the particle are simulated. This simulation can be considered as exact; it gives the same results as the solution of the transport equation. However, it can be used only if the number of collisions is not too large, a condition fulfilled only for special geometries (such as thin foils), or low enough kinetic energies. For larger kinetic energies the average number of collisions is very large and the detailed simulation becomes very inefficient. High energy simulation codes use condensed simulation algorithms, in which the global effects of the collisions are simulated at the end of a track segment. The global effects generally computed in these codes are the net displacement, energy loss, and change

of direction of the charged particle. These quantities are computed from the multiple scattering theories used in the codes. The accuracy of the condensed simulations is limited by the approximations of the multiple scattering theories.

Most particle physics simulation codes use the multiple scattering theories of Molire [67], Goudsmit and Saunderson [69] and Lewis [68]. The theories of Molire and Goudsmit-Saunderson give only the angular distribution after a step, while the Lewis theory computes the moments of the spatial distribution as well. None of these MSC theories gives the probability distribution of the spatial displacement. Therefore each of the MSC simulation codes incorporates its own algorithm to determine the spatial displacement of the charged particle after a given step. These algorithms are not exact, of course, and are responsible for most of the uncertainties in the MSC codes. Therefore the simulation results can depend on the value of the step length and generally one has to select the value of the step length carefully.

The MSC process in Geant4

The step length of the particles is determined by the physics processes or the geometry of the detectors. The tracking/stepping algorithm checks all the step lengths demanded by the (continuous or discrete) physics processes and determines the minimum of these step lengths.

Then, this minimum step length must be compared with the length determined by the geometry of the detectors and one has to select the minimum of the 'physics step length' and the 'geometrical step length' as the actual step length.

This is the point where the MSC model comes into the game. All the physics processes use the true path length t to sample the interaction point, while the step

limitation originated from the geometry is a geometrical path length z. The MSC algorithm transforms the 'physics step length' into a 'geometrical step length' before the comparison of the two lengths. This 't'→'z' transformation can be called the inverse of the path length correction.

After the actual step length has been determined and the particle relocation has been performed the MSC performs the transformation 'z'→'t', because the energy loss and scattering computation need the true step length 't'.

The scattering angle θ of the particle after the step of length 't' is sampled according to the model function given in equation 4.50. The azimuthal angle ϕ is generated uniformly in the range $[0, 2\pi]$.

$$g(u) = p[qg_1(u) + (1-q)g_3(u)] + (1-p)g_2(u) \tag{4.50}$$

where $0 \leq p, q \leq 1$, and the g_i are simple functions of $u = cos\theta$, normalized over the range $u \in [-1,\ 1]$. The functions g_i have been chosen as

$$g_1(u) = C_1 \quad e^{-a(1-u)} \qquad\qquad -1 \leq u_0 \leq u \leq 1 \tag{4.51}$$

$$g_2(u) = C_2 \quad \frac{1}{(b-u)^d} \qquad\qquad -1 \leq u \leq u_0 \leq 1 \tag{4.52}$$

$$g_3(u) = C_3 \qquad\qquad -1 \leq u \leq 1 \tag{4.53}$$

where $a > 0$, $b > 0$, $d > 0$ and u_0 are model parameters, and the C_i are normalization constants. It is worth noting that for small scattering angles, θ, $g_1(u)$ is nearly Gaussian ($exp(-\theta^2/2\theta_0^2)$) if $\theta_0^2 \approx 1/a$, while $g_2(u)$ has a Rutherford-like tail for large θ, if $b \approx 1$ and d is not far from 2 .

After the simulation of the scattering angle, the lateral displacement is computed using equation 4.54. Before doing this a check is performed to ensure that the relocation of the particle with the lateral displacement does not take the particle beyond the volume boundary.

The square of the mean lateral displacement is

$$\langle x^2 + y^2 \rangle = \frac{4\lambda_1^2}{3} \left[\tau - \frac{\kappa + 1}{\kappa} + \frac{\kappa}{\kappa - 1} e^{-\kappa\tau} - \frac{1}{\kappa(\kappa - 1)} e^{-\kappa\tau} \right] \tag{4.54}$$

Chapter 5

Results and Discussion

5.1 Introduction

In this chapter the results of induced activity measurements using the following methods will be presented: Filter paper, portable spectrometer, mathematical model, and Monte Carlo simulation. The results will be discussed, and the mean of equivalent dose to the radiotherapy technologist (RTT) will be estimated. In addition, the results of additional dose received by neutron particles for patients will be estimated.

5.2 Filter paper results

The estimation of the dose induced by activation products in medical linear accelerator to patients and technologist was based on determination of the ambient dose equivalent. Two types of filter paper were used for purpose of comparison and estimation of dose. The first type was Whatman filter manufactured from high quality cotton linters and the second type was made from Carbon.

Fig 5.1 shows the results of energy calibration curve using multiple gamma solution source. The activation of the treatment room of linear accelerator Varain 2100C was carried out by means of delivering 400 MU using 15 MV photon beam for field size

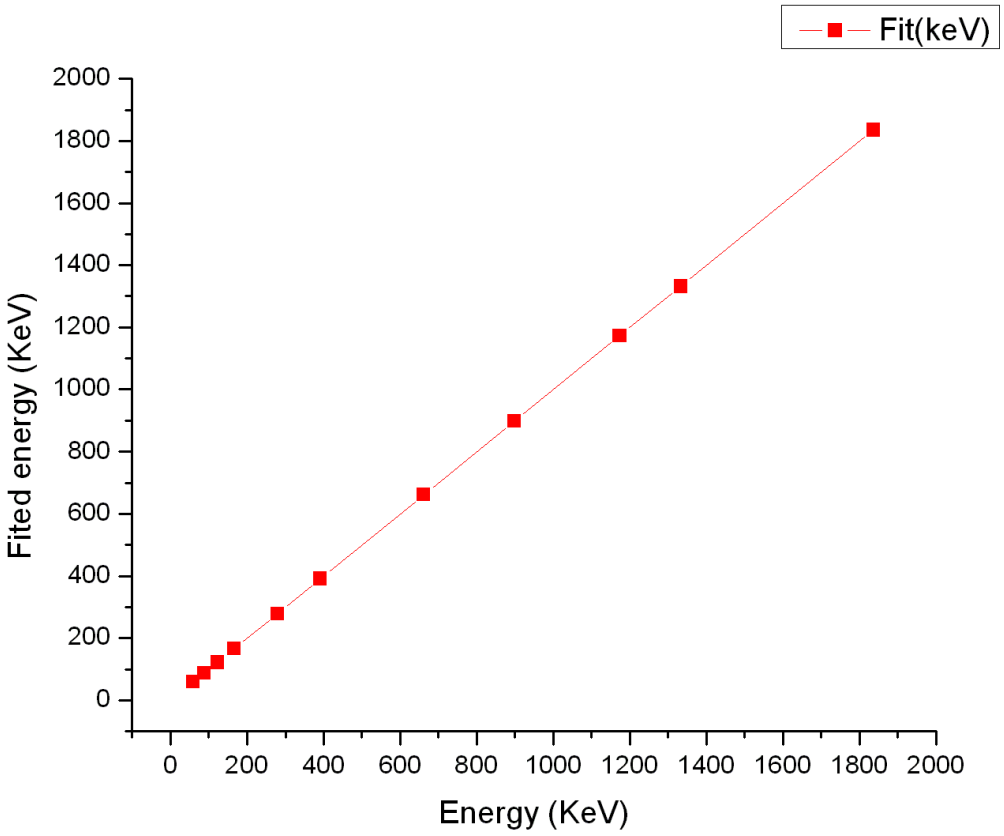

Figure 5.1: Energy calibration curve using Multigamma solution standard source.

10x10 cm^2. Fig 5.2 shows the components of high purity Germanium coaxial detector, where the measurements of filter papers were carried out. Table 5.1 presents the results of radioactive nuclides achieved by spectrometry using cotton filter paper after complete 10 min of air filtering process inside the treatment room. While, Table 5.2 presents same results for carbon filter paper.

The total activity detected by the cotton filter paper was found to be 0.23 MBq, while the total activity detected using the carbon filter paper was found to be 5.65

Figure 5.2: The components of High Purity Germanium Coaxial Detector.

MBq.

Table 5.1: The results of spectrometry using cotton filter paper after activation the treatment room with 15 MV photon beam for field size 10x10 cm^2 and deliver dose of 400 MU (dose rate = 240 MU/min).

Nuclide	Code	Activity (MBq)	Sigma Total (%)	Γ mSv m^2 h^{-1} GBq^{-1}	Dose rate (μSv h^{-1})
Na-24	<	0.0011		0.087	4.94E-08
Cr-51	<	0.0080		0.001	3.35E-09
Mn-54	<	0.0013		0.11	1.44E-04
Mn-56	”	0.0056	0.218	0.23	1.29E-03
Co-57	<	0.0009		0.0133	1.13E-05
Co-58	<	0.0013		0.129	1.69E-04
Co-60	<	0.0010		0.307	3.07E-04
Zn-65	<	0.0030		0.073	2.17E-04
Br-82	<	0.0017		0.343	5.87E-04
W-187	”	0.0065	0.319	0.073	4.75E-04
Au-196	<	0.0010		0.071	6.84E-05
Cu-64	<	0.0020		0.029	5.92E-05
Mo-99	<	0.0006		0.005	1.28E-09
Sb-122	<	0.0025	0.365	0.069	1.73E-04
Sb-124	<	0.0012		0.26	3.20E-04
Al-28	<	0.0006		0.222	1.42E-04
Fe-59	<	0.0028		0.147	4.12E-04
Ni-57	”	0.0065	0.209	0.255	1.65E-03
Re-184	<	0.0800		0.129	1.03E-02
Pb-203	<	0.1030		0.0001	4.43E-09
O-14	”	0.0010	0.379	0.028	1.45E-08

” - All peaks for activity calculation had bad shape.
< - MDA value printed.

The gamma dose rates shown in Table 5.1 and 5.2 were calculated from obtained activity data and by using gamma dose rate constant Γ for each isotope. We assume that these dose rates are representative for the absorbed dose rate at the isocenter

Table 5.2: The results of spectrometry using Carbon filter paper after activation the treatment room with 15 MV photon beam for field size 10x10 cm^2 and deliver dose of 400 MU (dose rate = 240 MU/min).

Nuclide	Code	Activity (MBq)	Sigma Total (%)	Γ mSv m^2 h^{-1} GBq^{-1}	Dose rate (μSv h^{-1})
Na-24	<	0.0081		0.087	7.02E-04
Cr-51		0.0770	0.428	0.001	6.43E-05
Mn-54	”	0.0101	0.428	0.11	1.11E-03
Mn-56	”	0.0203	0.216	0.23	4.66E-03
Co-57	<	0.0038		0.0133	4.99E-05
Co-58	”	0.0105	0.420	0.129	1.35E-03
Co-60	<	0.0067		0.307	2.04E-03
Zn-65	<	0.0145		0.073	1.06E-03
Br-82	<	0.0081		0.343	2.76E-03
W-187	<	0.0213		0.073	1.55E-03
Au-196	<	0.0049		0.071	3.50E-04
Cu-64	<	0.0102		0.029	2.96E-04
Mo-99	<	0.0030		0.005	1.37E-05
Sb-122	<	0.0036		0.069	2.48E-04
Sb-124	<	0.0062		0.26	1.61E-03
Al-28	<	0.0038		0.222	8.39E-04
Fe-59	<	0.0092		0.147	1.35E-03
Ni-57		0.0231	0.251	0.255	5.89E-03
Re-184	”	5.4000	0.279	0.129	6.97E-01
Pb-203	<	0.0065		0.0001	5.60E-07
O-14	<	0.0030		0.028	8.29E-05

” - All peaks for activity calculation had bad shape.
< - MDA value printed.

of the Clinac 2100C. The total dose rate given by cotton and carbon filter papers respectively are 0.016 and 0.72 μSv/h. From table 5.1 and 5.2 the most important isotopes for clinical routine, are Al-28 and O-14, while the dose rate generated by Cu-64, W-187, Na-24 and Mn-56 isotopes ($1h \leq T1/2 < 24$) are lower than that of short lived one.

Fig 5.3 shows comparison between the activity detected using the two types of filter papers. The results present deviation of 95.9 % for the total activity between the two types of filter papers used. This result of deviation verify the ability of carbon filter type in detecting the yield activity and express the suitability for using carbon rather than cotton filter papers in these measurements. In addition, choosing of carbon filter return to surpass the cotton filter paper in the physical characteristics of filtration.

The results of filter paper method present very low dose rate due to the delay cause by filtration process time (10 min) and the additional time of removing the sample from linear accelerator room to the spectrometry. The total delay time was assumed to be 12 min and from the results presented in section 5.3 the total dose rate decrease up to 73% after beam-off in 12 min with deviation of 13.3 %.

5.3 Portable spectrometer results

Data resulting from spectrometry measurements are summarized in Table 5.3 and typical spectrum from these measurements was shown in Fig 5.4 for maximum and minimum field sizes. The activity data from different times delay between times of beam off and spectrum acquisition were used to calculate the decay curve.

From Table 5.3 the most important isotopes are ^{28}Al, ^{62}Cu, ^{56}Mn, ^{64}Cu, ^{187}W,

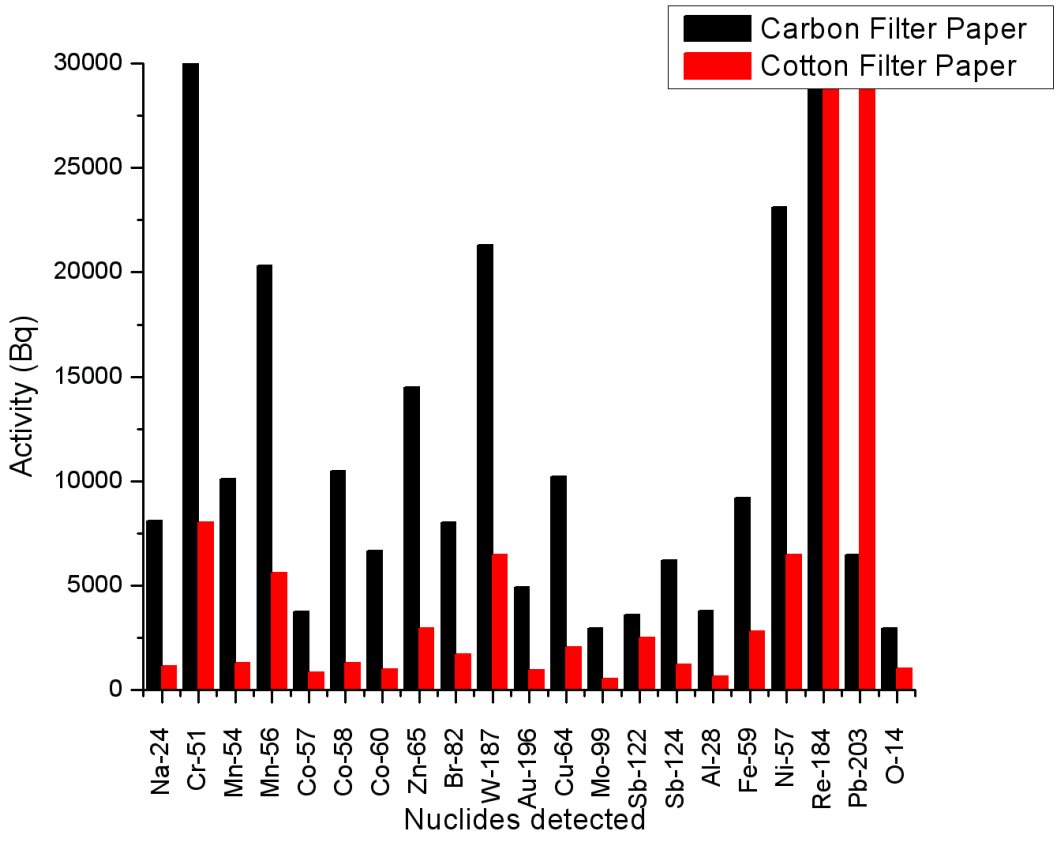

Figure 5.3: Comparison between filter paper results.

^{57}Ni, ^{196}Au, ^{54}Mn, ^{60}Co and ^{124}Sb. The criterion to select these isotopes was dominant in an interval of the dose rate vs. time plot as shown from Fig 5.5. The list is in good agreement with previously published data [12, 20, 49, 50].

In order to determine the effect of time, dose rate sum values were calculated using non linear least-square curve-fitting method for different time delays, and results are given in Table 5.4. The calculation of curve-fitting method was performed using the following equation:

$$y = A_1 \times \exp(\frac{-x}{t_1}) + A_2 \times \exp(\frac{-x}{t_2}) + A_3 \times \exp(\frac{-x}{t_3}) + y_0$$

where,

$y_0 = 0.04141 \pm 0.03811$,

$A_1 = 1.24419$,

$t_1 = 4.25137 \pm 6574.93586$,

$A_2 = 0.60985 \pm 0.1131$,

$t_2 = 213.39672 \pm 127.27516$,

$A_3 = 1.2494$,

$t_3 = 4.25078 \pm 6546.35835$.

The data reflect a clinical situation as encountered by RTT entering the treatment room after a high MU, high energy beam on a Friday afternoon. The situation will be slightly different on a Monday morning (as the room medium-lived isotopes will have decayed over the weekend and did not have time to build up again) or for a low-MU high energy beam (less short-lived isotopes will have been generated).

Due to the radionuclides with long half-lives, the activity will build up during the five working days and then decrease somewhat over the weekend.

Table 5.3: Identified isotopes for Varian Clinic 2100C, their dosimetric properties, apparent activities obtained from the spectra and the resulting dose rate at isocenter at the time of termination of the beam. Errors (Sigma) are derived from counting statistics and efficiency calibration error. Only data above the minimum detectable activity (MDA) have been considered.

Nuclide	$T_{1/2}$	Γ mSv m^2 h^{-1} GBq^{-1}	Activity (MBq)	Error (%)	Dose Rate (μSv h^{-1})
Fe-59	45.1 d	0.147	0.0065	9.1	0.001
Co-60	5.3 y	0.307	0.0097	8.2	0.003
Mn-56	2.6 h	0.23	0.69	3.3	0.16
Co-57	271.8 d	0.0133	0.012	9.5	0.0002
Cu-62	9.7 m	0.151	3.21	3.3	0.48
Cu-64	12.7 h	0.029	5.4	9.4	0.16
Zn-65	244.3 d	0.073	0.0127	9.1	0.0009
W-187	23.7 h	0.073	1.09	3.6	0.08
Au-196	6.2 d	0.071	0.005	2.1	0.0004
Ni-57	36.0 h	0.255	0.144	3	0.037
Co-58	70.9 d	0.129	0.025	4.8	0.0032
Na-24	15.0 h	0.429	0.036	4.7	0.0156
Al-28	2.3 m	0.222	9.8	8.2	2.17
Mn-54	312.3 d	0.11	0.0058	6.1	0.0006
Br-82	35.5 h	0.343	0.105	3.4	0.036
Sb-122	2.7 d	0.069	0.081	4.5	0.0056
Sb-124	60.2 d	0.26	0.024	6.3	0.0061
Re-184	38.0 d	0.129	0.077	7.1	0.01

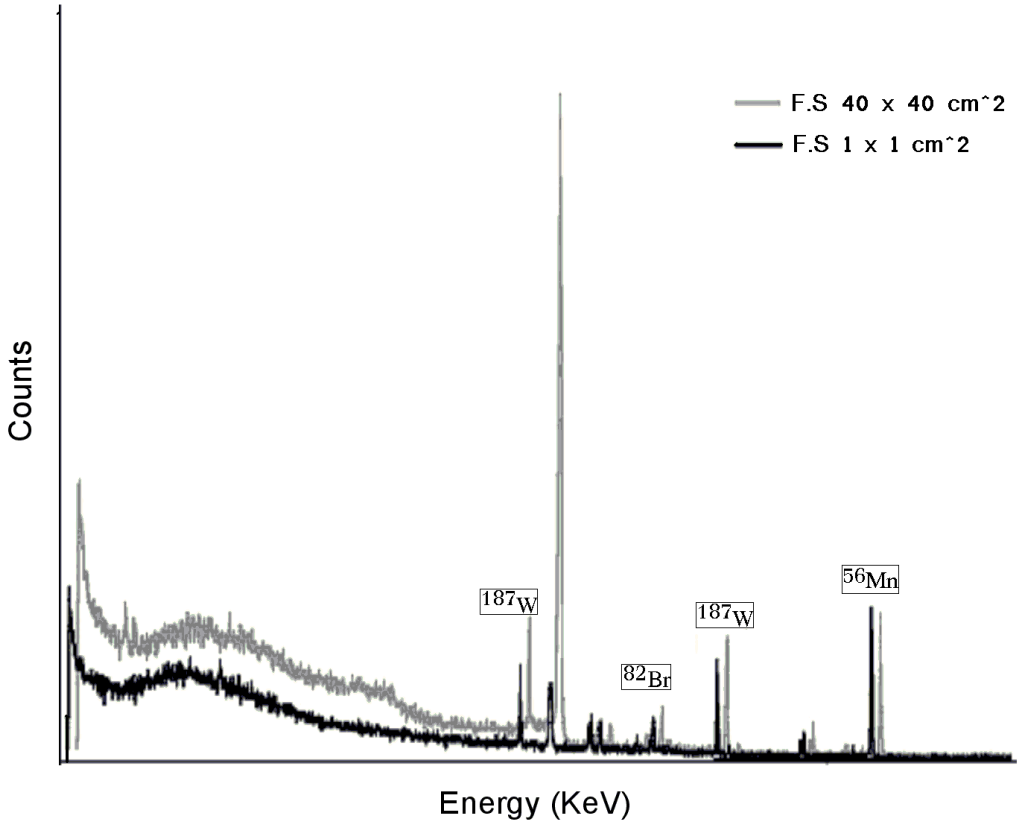

Figure 5.4: Typical spectrum from portable spectrometry at isocenter of Clinac 2100C after delivering 400 MU.

The gamma dose rates shown in Table 5.3 were calculated from the obtained activity data and using the gamma dose rate constant Γ for each isotope, obtained from the online Rad Pro Calculator [48] and calculated using the data develop by Unger L M and Trubey D K [51]. It is assumed that these dose rates are representative for the absorbed dose rate at the isocenter of the accelerator. The total activity and dose rate was found to be 20.8 MBq and 3.17 μSv/h respectively, with maximum error of 9.5 %.

Using calibrated ionization chamber survey meter (Model 450P, Victoreen, Inc.; Cleveland, OH) the average environmental background was found to be 0.1 $\mu Sv/h$. This environmental background was added to the measured dose rates using the following equation:

Table 5.4: Calculated dose rate for Varian Clinic 2100C and estimation of long time effects.

Time after beam-off	Dose Rate ($\mu Sv/h$)
0 min	3.16
1 min	2.55
2 min	2.24608
3 min	1.94249
5 min	1.34
10 min	0.85
20 min	0.69336
30 min	0.54
60 min	0.46
120 min	0.41
24 hour	0.15
1 week	0.018
1 month	0.012
1 year	0.0036
10 year	0.0008

$$\dot{D}_{tot} = \dot{D}_{meas} + \dot{D}_{back} \tag{5.1}$$

where,

$\dot{D}_{meas}$ = Measured dose rate.

$\dot{D}_{back}$ = Average environmental background dose rate.

The calculation of annual doses for the staff for RTTs was carried out using equation 5.2. According to equation 5.1 the total dose rate was change to 3.26 $\mu Sv/h$. In this study, we assumes the RTT performed one shift for 10 patients and entering the treatment room for 5 min after beam off per patient. So, the RTT entering the treatment room with total time of 12000 min per year. For one shift per day the RTT received 2.73 μSv. An estimation of long time effects and number of patients effects can be show in Table 5.5.

$$D_{anu} = D_{tot} \times T_p \times S \times T_d \times T_s \tag{5.2}$$

where,

D_{anu} = annual dose received by RTT,

T_p = total time required the RTT to setup the patient in the treatment room,

S = the number of patients treated in one shift,

D_{tot} = total dose rate per minute,

T_d = treatment day per year per one shift,

T_s = treatment shift of RTT.

Very short-lived (T1/2 $<$ 1 min) or pure beta-emitting nuclides was not involve in this study. In view of the good agreement of the list of identified isotopes at

Table 5.5: Calculated dose rate for radiotherapy technologist and estimation of long time and no of patients effects.

$mSv/year$	Setup Time / patient	No of patients
0.655	5 min	10
0.916	7 min	10
1.309	10 min	10
0.982	5 min	15
1.375	7 min	15
1.964	10 min	15

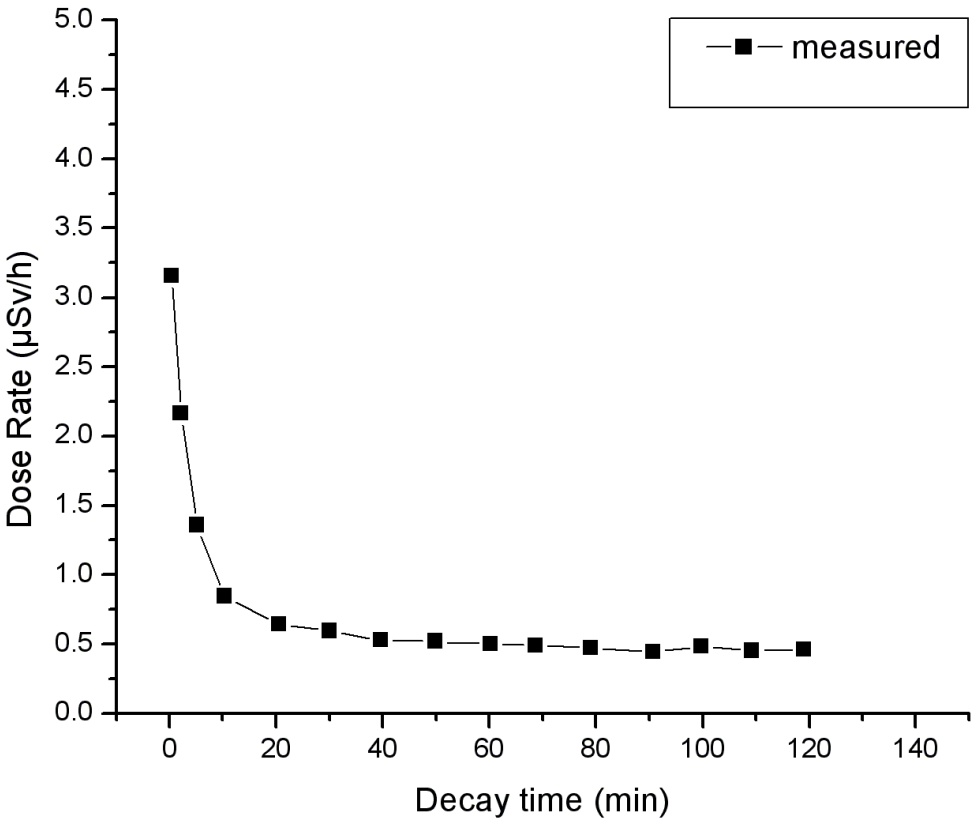

Figure 5.5: The results of measured dose rates for Varian 2100C.

higher energies, additional effects such as type of the material and design of the main components of the Linac head may affect the results of induced activity.

The short-lived isotopes ^{28}Al and ^{62}Cu (T1/2 $<$ 1 h) will be of importance for clinical routine; the activity level will follow the high energy photon output of the accelerator on a short time scale. As the experiments of this study involved a 400 MU beam, in clinical routine the results may slightly shift and increase by dose increment, this will explained in details later in section 5.5.

The activity of the medium-lived isotopes ^{56}Mn, ^{64}Cu and ^{187}W (1 h $\leq T_{1/2} <$ 24 h) will increase during a working day and decay, at least partially, over night. The induced dose rates generated by these isotopes are lower than that of the short lived ones. As the experiments in this study were carried out after a working day, the activity can be expected to be at or close to its maximum. The activities should reflect the clinical situation, whereas water phantom measurements or mechanical checks could significantly increase them.

^{196}Au, ^{57}Ni, ^{82}Br, ^{122}Sb (1 d $\leq T_{1/2} <$ 7 d) will contribute to the activity and resulting dose rate, which build up during the week and decrease over the weekend.

The long-lived isotopes ^{54}Mn, ^{60}Co and ^{124}Sb ($T_{1/2} \geq$ 7 d) can be expected to be in equilibrium and constant with time. From the calculated dose rate levels, these isotopes will be of no importance in a clinical environment. On the other hand, as ^{60}Co ($T_{1/2}$ = 5.3 y) has been found in the Clinic 2100C, a problem may arise during decommissioning of accelerator or part of it.

Several effects might alter the obtained results, among them absorption and scattering in the patient, use of different gantry angles and field sizes, installation of accessories and the application of intensity-modulated radiation therapy (IMRT) techniques. In particular, IMRT involves a series of small fields, to obtain a specific treatment, with a complex dose distribution, for an individual patient. Some of these issues was studied and the results presented in details using Monte Carlo simulation in section 5.5.

5.4 Mathematical model results

Based on mathematical model in section 4.4, and by using equation 4.26, the decay behavior at the isocenter of Clinac 2100C linac after irradiation can now be approximated as follows:

$$\begin{aligned}
\dot{D}_c = {} & \dot{D}_{59Fe}(1-e^{-\lambda_{59Fe}.t_r})e^{-\lambda_{59Fe}.t} + \dot{D}_{60Co}(1-e^{-\lambda_{60Co}.t_r})e^{-\lambda_{60Co}.t} \\
& + \dot{D}_{56Mn}(1-e^{-\lambda_{56Mn}.t_r})e^{-\lambda_{56Mn}.t} + \dot{D}_{57Co}(1-e^{-\lambda_{57Co}.t_r})e^{-\lambda_{57Co}.t} \\
& + \dot{D}_{62Cu}(1-e^{-\lambda_{62Cu}.t_r})e^{-\lambda_{62Cu}.t} + \dot{D}_{64Cu}(1-e^{-\lambda_{64Cu}.t_r})e^{-\lambda_{64Cu}.t} \\
& + \dot{D}_{65Zn}(1-e^{-\lambda_{65Zn}.t_r})e^{-\lambda_{65Zn}.t} + \dot{D}_{187W}(1-e^{-\lambda_{187W}.t_r})e^{-\lambda_{187W}.t} \\
& + \dot{D}_{196Au}(1-e^{-\lambda_{196Au}.t_r})e^{-\lambda_{196Au}.t} + \dot{D}_{57Ni}(1-e^{-\lambda_{57Ni}.t_r})e^{-\lambda_{57Ni}.t} \\
& + \dot{D}_{58Co}(1-e^{-\lambda_{58Co}.t_r})e^{-\lambda_{58Co}.t} + \dot{D}_{24Na}(1-e^{-\lambda_{24Na}.t_r})e^{-\lambda_{24Na}.t} \\
& + \dot{D}_{28Al}(1-e^{-\lambda_{28Al}.t_r})e^{-\lambda_{28Al}.t} + \dot{D}_{54Mn}(1-e^{-\lambda_{54Mn}.t_r})e^{-\lambda_{54Mn}.t} \\
& + \dot{D}_{82Br}(1-e^{-\lambda_{82Br}.t_r})e^{-\lambda_{82Br}.t} + \dot{D}_{122Sb}(1-e^{-\lambda_{122Sb}.t_r})e^{-\lambda_{122Sb}.t} \\
& + \dot{D}_{124Sb}(1-e^{-\lambda_{124Sb}.t_r})e^{-\lambda_{124Sb}.t} + \dot{D}_{184Re}(1-e^{-\lambda_{184Re}.t_r})e^{-\lambda_{184Re}.t}
\end{aligned} \tag{5.3}$$

Where the decay constants of the above isotopes are calculated from the standard relationship of these half-life. From the results of portable spectrometry, we assume that, only five isotopes ^{28}Al,^{56}Mn,^{62}Cu,^{64}Cu, and ^{187}W contribute to most of the induced activity at the isocenter, whereas the activation of other materials is negligible or will be of no importance in clinical environment due to it is long life. Furthermore, equation 5.3 can rewritten as following:

$$\begin{aligned}\dot{D}_c = \dot{D}_{56Mn}(1-e^{-\lambda_{56Mn}.t_r})e^{-\lambda_{56Mn}.t} + \dot{D}_{62Cu}(1-e^{-\lambda_{62Cu}.t_r})e^{-\lambda_{62Cu}.t} \\ +\dot{D}_{64Cu}(1-e^{-\lambda_{64Cu}.t_r})e^{-\lambda_{64Cu}.t} \\ +\dot{D}_{187W}(1-e^{-\lambda_{187W}.t_r})e^{-\lambda_{187W}.t} \\ +\dot{D}_{28Al}(1-e^{-\lambda_{28Al}.t_r})e^{-\lambda_{28Al}.t} \qquad (5.4)\end{aligned}$$

Similarly to the method used by other physicists,[12, 13, 22], we applied a nonlinear least-square curve-fitting method to the decay curves measured at the isocenter of the Clinac 2100C linac in the time interval from 2 to 15 min after giving various amounts of MUs (1000, 5000, 9000, 12000, and 20000 MU, corresponding to irradiation times of 1.7 , 4.17, 37.5, 50, 62.5, and 83.3 min at a dose rate of 240 MU/min).

Since the decay curves were typically followed only for 15 min and thus do not provide enough information for the long-term component (such as ^{187}W and ^{64}Cu), the mean values of these components extracted from curve-fitting as mention above.

For example, the maximum dose rates at irradiation dose of 20000 MU for ^{28}Al, ^{62}Cu, ^{64}Cu, ^{56}Mn and ^{187}W were determined to be $(\dot{D}_{max})_{28Al} = 22\mu Sv/h$, $(\dot{D}_{max})_{56Mn} = 26\mu Sv/h$, $(\dot{D}_{max})_{62Cu} = 34\mu Sv/h$, $(\dot{D}_{max})_{64Cu} = 23.3\mu Sv/h$, and $(\dot{D}_{max})_{187W} = 1.9\mu Sv/h$. While, the contribution from naturally occurring background radiation

was measured in a room far away from the treatment room using calibrated ionization chamber survey meter (Model 450P, Victoreen) and the background dose rate was found to be 0.1 $\mu Sv/h$. By substituting the maximum dose rates and adding the background, the general decay equation written as following:

$$\begin{aligned}\dot{D} = 0.1 + [26(1 - e^{-0.0044.t_r})e^{-0.0044.t} + 34(1 - e^{-0.07142.t_r})e^{-0.07142.t} \\ +23.3(1 - e^{-0.00091.t_r})e^{-0.00091.t} \\ +1.9(1 - e^{-0.00049.t_r})e^{-0.00049.t} \\ +22(1 - e^{-0.30141.t_r})e^{-0.30141.t}] \qquad (5.5)\end{aligned}$$

where $\dot{D}$ was given in $\mu Sv/h$ and the activation time t_r as well as the decay time t were given in minutes.

The accuracy of the model equation 5.4 is affected by the following factors: (1) only five radionuclides chosen to represent all the radionuclides in a linac room to describe the induced activity; (2) the curve-fitting method; (3) the relatively short 15 min measurement time of the decay curves; and (4) the assumption that the background activation level is constant. However, the model provides a reasonable approximation and predicts well the actual activation levels in the treatment room under various experimental.

This mathematical model of the activation level of Clinac 2100C room was verified and compared by the decay curves measured at the isocenter using the standard experimental setup after giving 1000 MU (t_r=4.17 min), 5000 MU (t_r=37.5 min), 9000 MU (t_r =50 min), 12 000 (t_r=62.5 min), and 20 000 MU (t_r =83.3 min). Fig 5.6 show the comparison between mathematical model and the data calculated from equation 5.4. The calculated curves agree well with measured data within our measurement

uncertainty. We thus conclude that the simple model given by equation 5.4 can be used to estimate reasonably well the pattern of induced activity at the machine isocenter (or point A, see Fig 4.1) following a given radiation dose produced by linac.

The model can be used to estimate the relative contributions to the induced activity from the ^{56}Mn, ^{28}Al, ^{62}Cu, ^{64}Cu and ^{187}W radionuclides. Table 5.6 shows the dose rates from these isotopes immediately (t=0) after delivering doses of 1000 MU, 5000 MU, 9000 MU, 12 000 MU, and 20 000 MU at a dose rate of 240 MU/min. For a single irradiation of at least up to 20 000 MU, the exposure rates from the short-lived radionuclides (^{28}Al and ^{62}Cu) are much higher than that from the long-lived ^{187}W and ^{64}Cu.

Table 5.6: Exposure rates immediately (t=0) after delivering doses of 1000 MU, 5000 MU, 9000 MU, 12 000 MU, and 20 000 MU at a dose rate of 240 MU/min measured for the ^{56}Mn, ^{28}Al, ^{62}Cu, ^{64}Cu and ^{187}W radionuclides.

Dose delivered (MU)	Activation time (min)	$\dot{D}_{28Al}$	$\dot{D}_{56Mn}$	$\dot{D}_{62Cu}$	$\dot{D}_{64Cu}$	$\dot{D}_{187W}$
1000	4.17	11.6	3.2	5.7	3.1	0.1
5000	37.5	22	10.3	12.36	9.6	0.6
9000	50	22	25	28	26	0.8
12000	62.5	22	25	30.9	26.1	1.1
20000	83.3	22	26	34	23.3	1.9

Fig 5.7 show the results of dose rate vs. monitor unit (MU) used during the irradiation of Clinac 2100C room. The results show increase of dose rate with the increment of MU. In the other hand, the results of determination the effect of long time using nonlinear curve-fitting method for dose rate was shown in Fig 5.8. The calculated decay curves show the dose rate for a given irradiation (activation) dose of 1000 MU; 5000 MU; 9000 MU; and 12000 MU. The dose rate is plotted against the decay time; measured data are shown with data points; nonlinear curves-fitting are

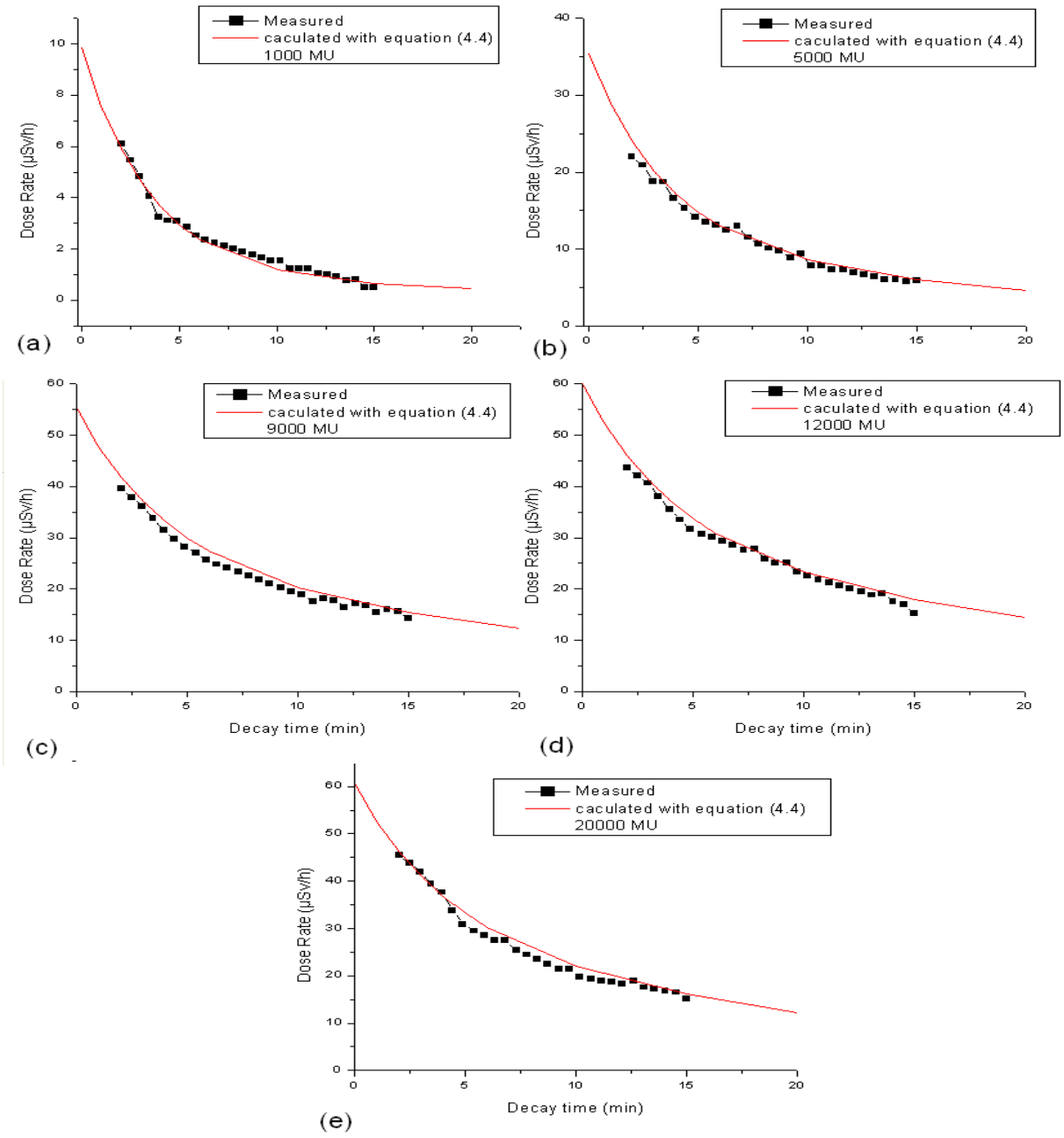

Figure 5.6: A comparison of measured and calculated decay curves after a given irradiation (activation) dose of 1000 MU in (a); 5000 MU in (b); 9000 MU in (c); 12000 MU in (d); and 20000 MU in (e). The dose rate is plotted against the decay time; measured data are shown with data points; decay curves are calculated from equation 4.4 with solid curves.

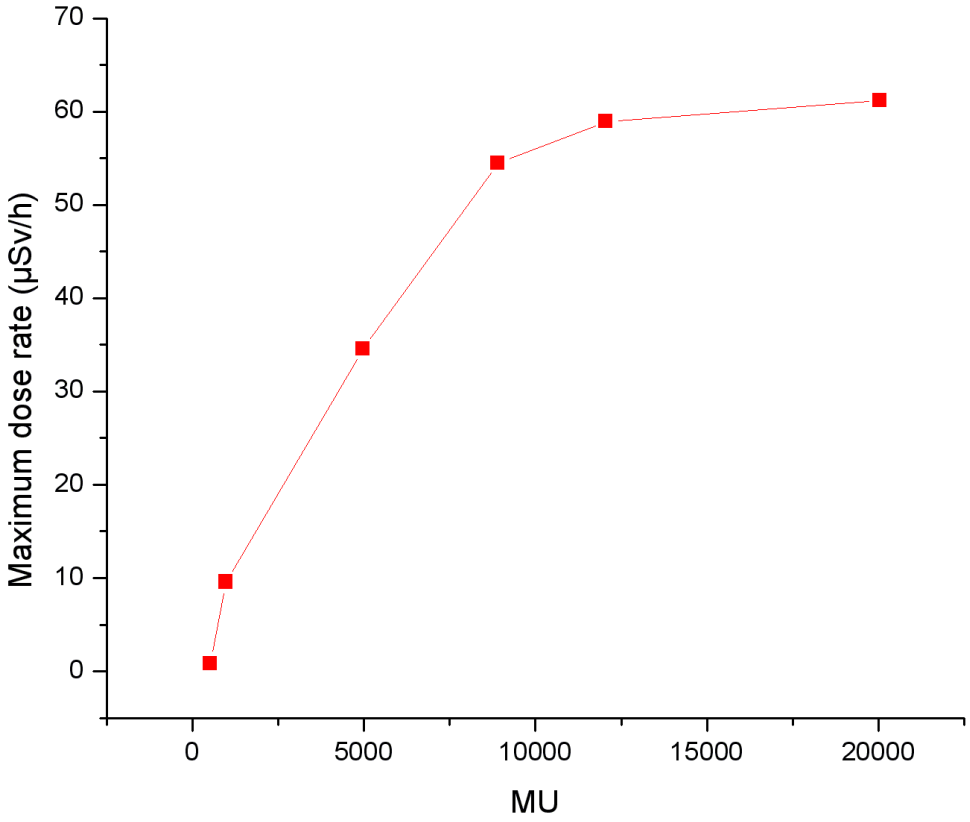

Figure 5.7: A comparison between monitor units (MU) used during the activation time vs. the maximum calculated dose rate after beam-off.

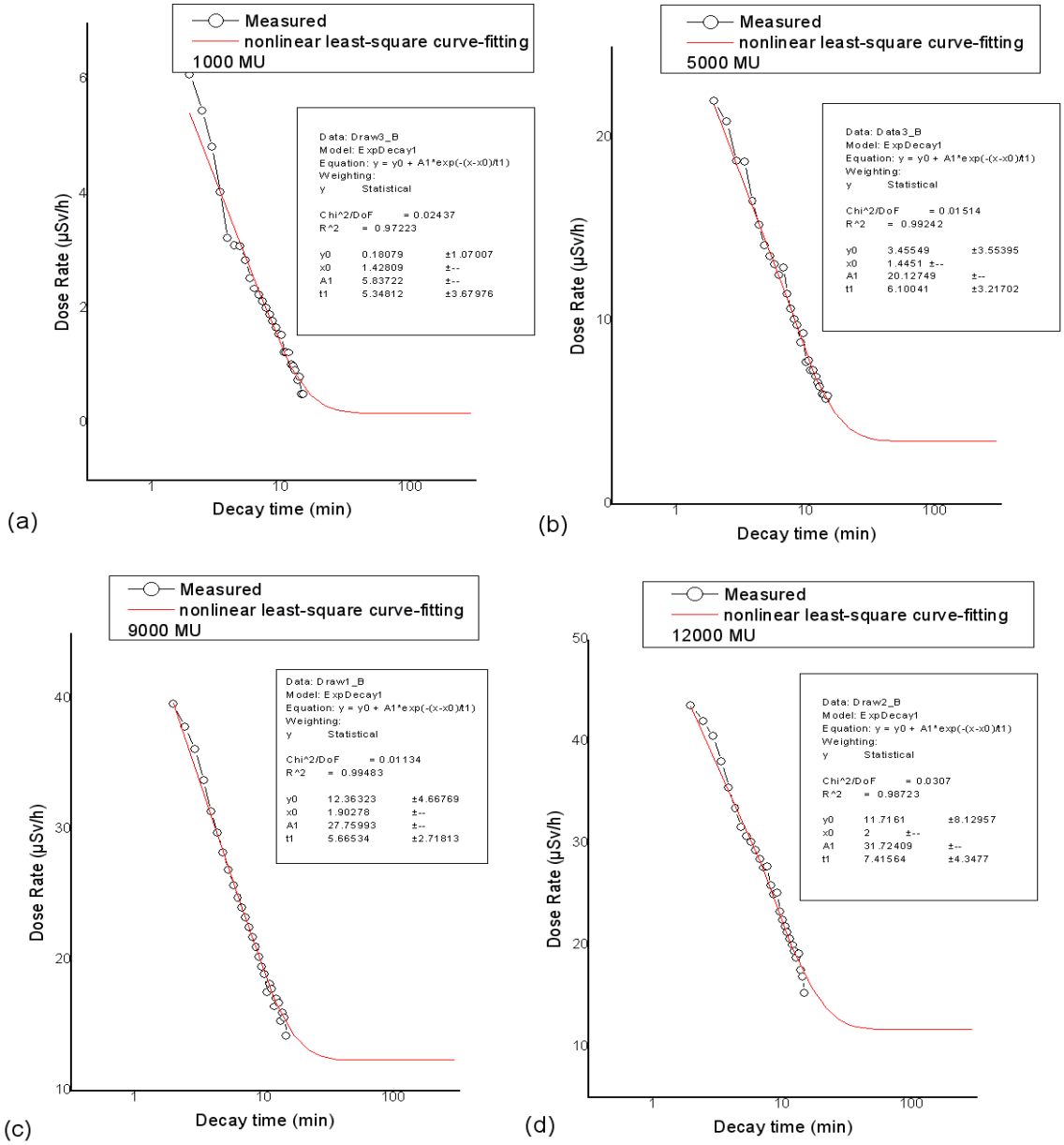

Figure 5.8: Results of using nonlinear curve-fitting method for dose rate for long time. The calculated decay curves show a given irradiation (activation) dose of 1000 MU in (a); 5000 MU in (b); 9000 MU in (c); and 12 000 MU in (d). The dose rate is plotted against the decay time; measured data are shown with data points; nonlinear curves-fitting are shown with solid curves.

shown with solid curves and calculated from the following equation:

$$y = Y_0 + A_1 \times \exp(-(X - X_0)/t_1)$$

where, the values of A_1, Y_0, X_0, and t_1 were attached in the Fig 5.8.

5.5 Monte carlo simulation results

Monte Carlo calculations of the photoneutrons around the Varian Clinac 2100C medical accelerator heads were made using the Geant4 code. The Varian Clinac 2100C, operating in our simulation in four x-ray modes at 10, 15, 18 and 20 MV. In this section the results of induced activity measured using Geant4 code will be presented.

5.5.1 Neutron production and transport with Geant4 in Linac head

A neutron history file was generated, which contained the parameters of number, position, direction, energy and track length for those neutrons generating from photons interactions. These neutron histories were then analyzed by OriginPro ver7.5 SR0 software.

Geant4 calculate the total number of neutron yield (including both the evaporation and direct components) by multiplying the corresponding photoneutron yield cross section with the photon track length.

The results of neutron yields in the components of the head (target, flattening filter, primary collimator and jaws) with jaw closed, i.e., 1 x 1 cm^2 field size, are shown in Fig 5.9.

The fluence at 1 m from the target estimated as the neutron yield divided by area of the detector ($4\Pi(1)^2$). Results given in Fig 5.9 present the neutrons yields for

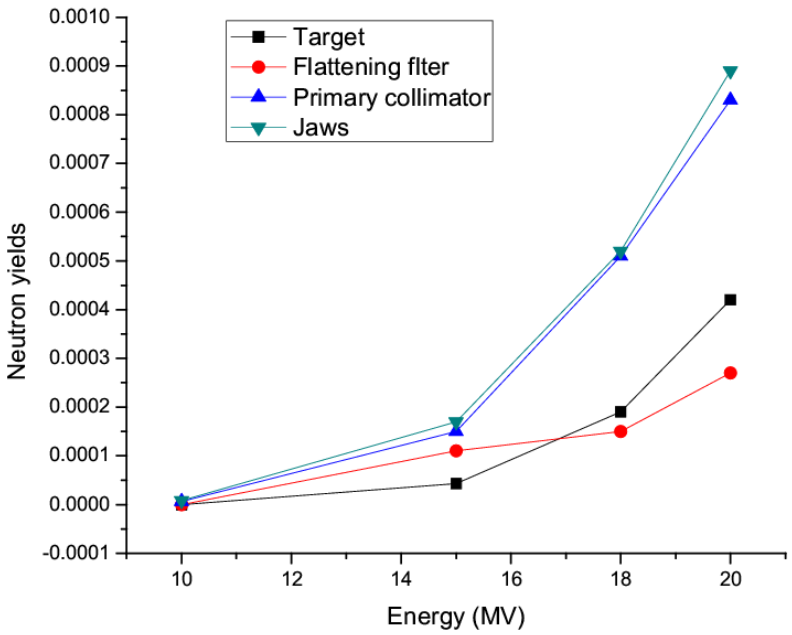

Figure 5.9: Geant4-calculated neutron yields in the Varian Clinac 2100C head (minimum field size).

different x-ray energy. Furthermore, the maximum neutrons yields was found in the jaws, with increase of neutrons number by increment of the energy.

Fig 4.1 in chapter four shows the three positions around the head at which the neutron fluence and average energy ,E_a, were calculated using Geant4 code. The corresponding fluence and average energy values are shown in Fig 5.10.

The disadvantageous of Geant4 it's inability to calculate the equivalent dose produced by neutron yields. The calculation of the fluence was carried out by dividing the total number of neutron yield in the volume of detector (sphere, see Fig 4.12) by the cross-sectional area of the sphere, (1 cm^2). Furthermore, all calculation of fluence in the head component was carried out by the same calculation method. Since we

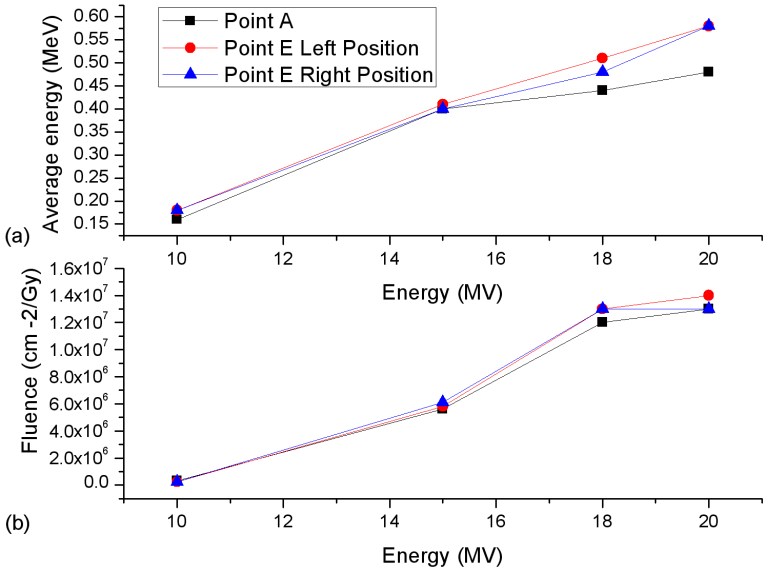

Figure 5.10: (a) Average energy E_a and (b) fluence ϕ (cm^{-2} Gy^{-1}) of the leakage neutrons around the Varian Clinac 2100C head (minimum field size), calculated with the Geant4 code.

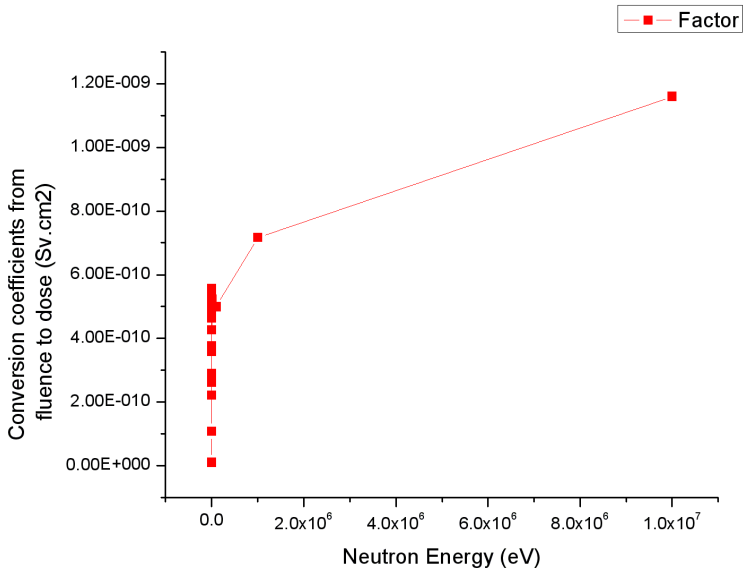

Figure 5.11: Conversion coefficients from fluence to dose for neutron energies.

have neutrons of various energies in the sphere we deal with these in appropriate energy groups in order to estimate the dose. Using conversion coefficients from fluence to ambient dose equivalent as shown in Fig 5.11 [52] for different energy neutrons the dose was estimated. The ambient dose equivalent using minimum field size, at point A and x-ray modes 20, 18, 15 and 10 MV, was found 1.79, 1.60, 0.62, and 0.02 mSv Gy^{-1} respectively. The mean energy of neutrons were 0.48, 0.44, 0.40, and 0.16 MeV at 20, 18, 15, and 10 MV respectively.

5.5.2 Measurements of activation as a function of air density in the treatment room

The changes occur in the pressure and temperature inside the treatment room of linear accelerator leads to effect the air density. Table 3.3 show the abundances of

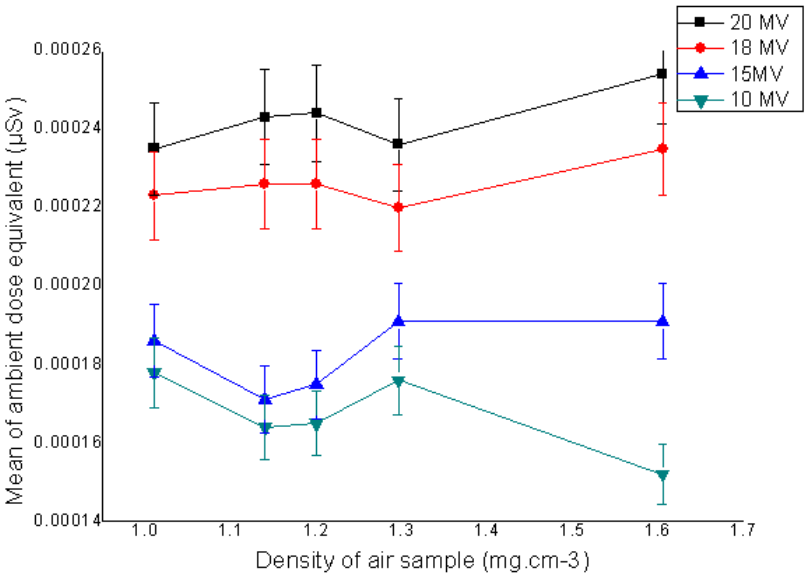

Figure 5.12: Mean of ambient dose equivalent in comparison with different air density mediums (error bar is ±5%).

the most prominent stable nuclides in the atmosphere at different densities.

Geant4 was used to study the effect of changing the air density and Fig 5.12 show the mean values of ambient dose equivalent in comparison with different air density for filed size 10×10 cm^2 and target to skin distance of 100 cm^2. Furthermore, Fig 5.12 show additional comparison for x-ray modes 20, 18, 15 and 10 MV, where the ambient dose equivalent at all x-ray modes represent fluctuation in its values vs. air density, while it's clear the increase of ambient dose with the increase of energy.

5.5.3 Calculation of electron kinetic energy and dose per Monitor Unit

Generally, in clinical mode, the linear accelerators calibrated to deliver one cGy per one MU. There is many protocols such as IAEA TRS-398 [76] used for the determination the absorbed dose in water and IAEA TRS-277 [77] for determination the absorbed dose in air. In this section the results and calculation of the electron kinetic energy for Tungsten target with thickness of 0.5 cm will be presented. In addition, the simulation of 1 cGy/MU will be explained.

Table 5.7 show the calculated electron kinetic energy for different x-ray energy. The calculation was performed using Geant4 by convert the geometry of target itself to detector. The photon history file was generated, which contained the parameters of number, position, direction, energy and track length for those photons generating from electrons entering the target. Where we have not any idea about the required number of electrons to produce the required x-ray energy, we start by increase the electron number randomly and observe the photon history file to know the energy. Finally, we classify the electron kinetic energy according to the required electrons number and resulted energy of x-rays.

Table 5.7: Calculated electron beam kinetic energy for different x-ray energy from Tungsten target with thickness of 0.5 cm.

X-ray Energy (MV)	Electron beam kinetic energy (MeV)
20	22.3
18	18.8
15	14.9
10	10.3

The calculations of the dose in air at the specific volume in our simulation was performed by using the following equation:

$$D = C \sum_i M_i E_i (\mu_{en}/\rho)_i \tag{5.6}$$

where, the index i defines a particular energy interval, M_i is the fluence for the ith group, E_i is the average energy of the ith group, and $(\mu_{en}/\rho)_i$ is the mass energy absorption coefficient for the photons energy E_i, and the summation is over all of the energy intervals that was selected; the constant C is a conversion constant to convert dose to the desired units.

The geometry of the detector was placed with distance of 100 cm from the target and from photon history file generated, and the energy intervals that extend between two different energies was selected. Then uniform energy intervals that are 0.5 MeV in width was used. In such an instance, if the photons of concern ranged in energy from 0 to 20 MeV, 40 energy intervals will be used. The midpoint of a given energy interval is the value of E_i for that interval, and $(\mu_{en}/\rho)_i$ is the mass energy absorption coefficient at that energy.

Table 5.8 show the the mass energy-absorption coefficient used in equation 5.6. This table is available in the database of the National Institute of Standards and Technology [78], and these data are calculated by Hubbell 1982 [79] and updated again by J. H. Hubbell and S. M. Seltzer in 1996 [80].

Using OriginPro Ver 7.5 SR0 software the calculation of the dose in air was performed at 100 cm (target to skin distance) in the isocenter for field size 10×10 cm^2 using equation 5.6. The criterion to determination the dose by equation 5.6 was dominance in many factors in Geant4 such as: (1) setting the electrons particle momentum direction, (2) setting the electrons particle position, where the G4PrimaryParticle class represents a primary particle with which Geant4 starts simulating an event.

Table 5.8: Photon mass attenuation coefficients and the mass energy-absorption coefficients from 1 keV to 20 MeV for Air, Dry [78].

Energy (MeV)	$\mu/\rho(cm^2/g)$	$\mu_{en}/\rho(cm^2/g)$
1.00E-03	3606	3599
0.0015	1191	1188
0.002	527.9	526.2
0.003	162.5	161.4
0.0032	134	133
0.0032	148.5	146
0.004	77.88	76.36
0.005	40.27	39.31
0.006	23.41	22.7
0.008	9.921	9.446
0.01	5.12	4.742
0.015	1.614	1.334
0.02	0.7779	0.5389
0.03	0.3538	0.1537
0.04	0.2485	0.06833
0.05	0.208	0.04098
0.06	0.1875	0.03041
0.08	0.1662	0.02407
0.1	0.1541	0.02325
0.15	0.1356	0.02496
0.2	0.1233	0.02672
0.3	0.1067	0.02872
0.4	0.09549	0.02949
0.5	0.08712	0.02966
0.6	0.08055	0.02953
0.8	0.07074	0.02882
1	0.06358	0.02789
1.25	0.05687	0.02666
1.5	0.05175	0.02547
2	0.04447	0.02345
3	0.03581	0.02057
4	0.03079	0.0187
5	0.02751	0.0174
6	0.02522	0.01647
8	0.02225	0.01525
10	0.02045	0.0145
15	0.0181	0.01353
20	0.01705	0.01311

This class object has information on particle type and its three momenta. The positional and time information of primary particle(s) are stored in the G4PrimaryVertex class, (3) setting the electrons number of particles to be generated.

In the other hand, variable of equation 5.6 change by user according to above factors, while the verification of Geant4 calculation in section 5.5.9 help us to estimate the correct factors.

In the most of the results of ambient dose equivalent the dose used in our simulation is 1 cGy or 1 Gy. Some times in clinical mode the 1 cGy dose conceder low dose, and due to this one can observe the small values in the results of ambient dose equivalent calculated from neutrons yields.

5.5.4 Simulation cycle and accuracy

The major aim throughout all measurements of induced activity is to achieve a high degree of accuracy for estimation the dose for each of worker and patients. To realize this, mainly in Geant4 calculation, the number of event generated by the simulation process was been sufficiently large. Fig 5.13 show plot of the efficiency rate versus the number of simulation cycles (events number). The efficiency, ε, calculated using the following equation:

$$\varepsilon = \frac{1}{S^2 T} \tag{5.7}$$

where,

S = The variance of sample group.

T = Computer time.

The variance of sample group calculated using the following equation:

$$S = \sigma^2 = \frac{1}{n}\sum_{i=1}^{n}(\mu - \overline{\mu})^2 \tag{5.8}$$

where,

μ = The mean value.

n = number of samples.

The number of simulation cycle can be set at any integer. If we suppose n monte carlo simulation test have been conducting, then the neutron number or energy efficiency generating in the history file can be evaluate vs. event number as shown in Fig 5.13. Fig 5.13 show the rate of efficiency increase with the increase the number of simulation events and fluctuation was shown clear within the small numbers of simulation events.

5.5.5 Measurements of activation as a function of accelerator energy

Activation levels at the isocenter were determined using the standard setup for different x-ray modes (20, 18, 15 and 10 MV) and for two filed sizes 1x1 and 40x40 cm^2. The results of ambient dose equivalent from neutron yield for this experiment on the Clinac 2100C linac are shown in Fig 5.14. After 10 MV, the calculated ambient dose equivalent curve for both field sizes start to increase with the increase of energy, and the results of ambient dose equivalent per 1 cGy represent high values in the curve for field size 40 x 40 cm^2 rather than filed size of 1x1 cm^2.

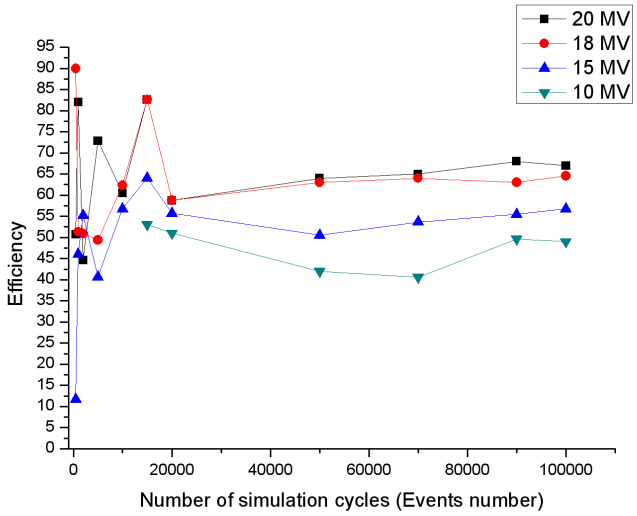

Figure 5.13: Plot of the rate of efficiency versus the number of simulation cycles (Events number).

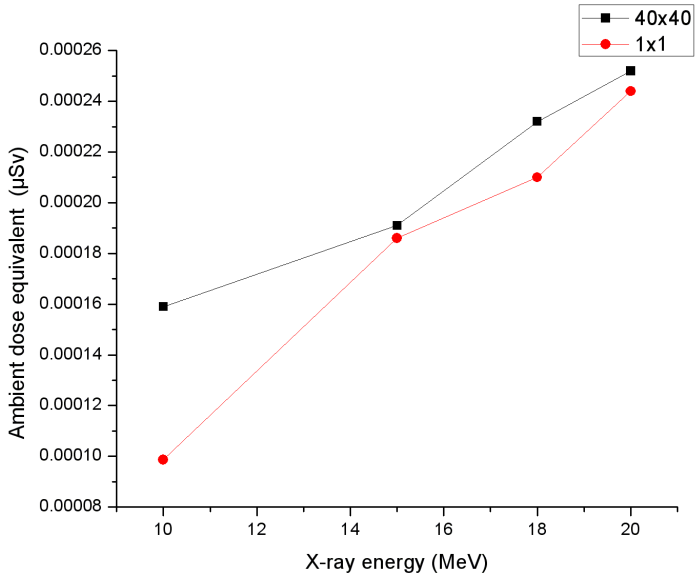

Figure 5.14: Ambient dose equivalent for patients in comparison with different photon energies.

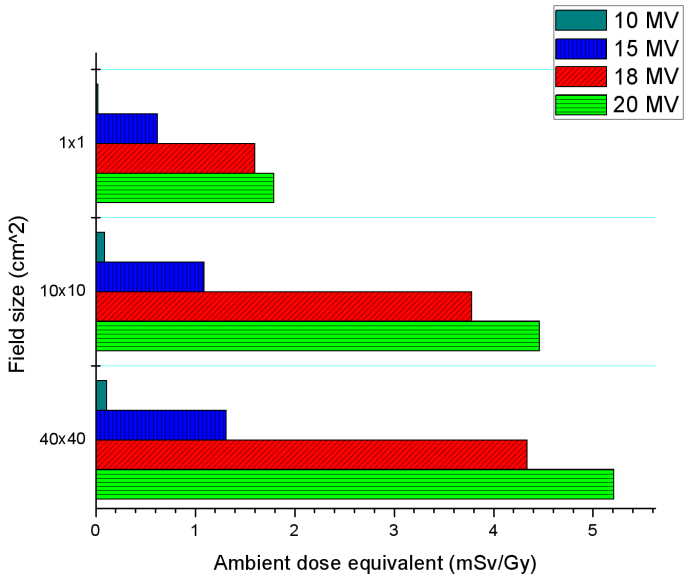

Figure 5.15: Mean of ambient dose equivalent in comparison with different filed sizes.

5.5.6 Measurements of activation as a function of filed size

Different x-ray modes (20, 18, 15 and 10 MV), and three field sizes (1 x 1, 10 x 10 and 40 x 40 cm^2) were used for determination the ambient dose equivalent at the isocenter, point A (see Fig 4.1) to study the effect of field size change. When the collimator jaws were used to define the field, MLC leaves were fully opened as prescribed for the operation of the linac. The results of ambient equivalent dose are shown in Fig 5.15. It is evident from that as the size of the radiation beam increases, so does the photoneutron fluence, with the difference between the smallest and the largest field size being in the order of 23.5 $\pm$ 1.5 %. The results of ambient dose equivalent calculated for these filed sizes from neutron yield is per 1 Gy of x-ray generated.

5.5.7 Measurements of activation as a function of target thickness

Choosing the materials and thickness for target in medical linear accelerator design was been studies by many authors. The radionuclides yield from different targets thickness, having different atomic number ,Z, have been studied by Cohen in 1978 [5]. The theory of Cohen represent that the target thickness exceeds the range of the incident ions and that the irradiation period greatly exceeds the half-life of the radionuclide of interest.

In this section, the results of ambient dose equivalent vs. different targets thicknesses will presented to study the effect of thickness and material of target by means of MC method.

The geometry of target used in the simulations was shown in Fig 4.13. As an electron beam hits the target surface and bremsstrahlung photons are created and emitted in all directions with a predominance in the forward direction. These photons pass through the the flattening filter, the monitor chamber and the collimators.

Fig 5.16 show plotted curve for target thickness vs. average anergy ,$\overline{E}$, (MeV) for x-ray produced by electron energy of 22.3 MeV for Al, W and Ni target materials. One would expect to see a decrease in $\overline{E}$ as the target thickness is increase from the thin to the thick target. Other things to note in Fig 5.14 are that initially $\overline{E}$ is slightly larger for W than for Al and Ni and that, as the thickness increase, all three materials harden the beam. In other words Al which has a harding effect on a photon spectrum generated in Al, would have a very similar effect on the photon spectrum generated in Ni.

The quantity of average energy ,$\overline{E}$, are calculated by Geant4 using the following

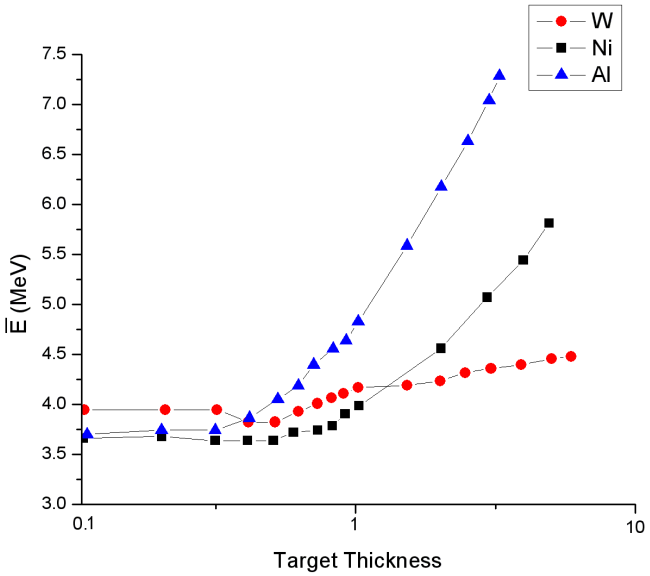

Figure 5.16: The variation of average energy $\overline{E}$ of the x-ray spectrum produced by 22.3 MeV electron on various target thickness and various materials (W, Al, and Ni) . The value of $\overline{E}$ are obtained from Geant4 calculation.

equation:

$$\overline{E} = \frac{\int_0^{E_{max}} E(dN/dE)dE}{\int_0^{E_{max}} (dN/dE)dE} \tag{5.9}$$

where, dN/dE is the number of phtons/cm^2 in an energy interval dE and E_{max} is the kinetic energy of the primary electros.

The quantity of ambient dose equivalent was calculated using the the conversion coefficients from fluence to dose show in Fig 5.11 for RTT and Fig 5.17 show the results of these quantity vs. target thickness per 1 cGy at point A. The mean ambient dose equivalent increase with the increment of the target thickness.

5.5.8 Total dose to the RTT

In addition to the dose received by RTT due to the induced activity, the RTT can also received additional dose during the treatment time from particles penetrating the treatment room wall. Neutrons produced in photonuclear reactions, mainly in the accelerator head, penetrate the radiation shield in the walls and contribute to the irradiation of the RTT.

The calculation of total dose equivalent ,D_t, was performed using the following equation:

$$D_t = (D_{in} + D_{tr})_n + (D_{in} + D_{tr})_p \tag{5.10}$$

where, $(D_{in}+D_{tr})_n$ is the total dose from the contribution of neutrons, $(D_{in}+D_{tr})_p$ is the total dose from the contribution of photons. D_{in} is dose from induced activity and D_{tr} is the dose from radiation transmitted through the walls of the treatment room. Each of these doses have been estimated separately.

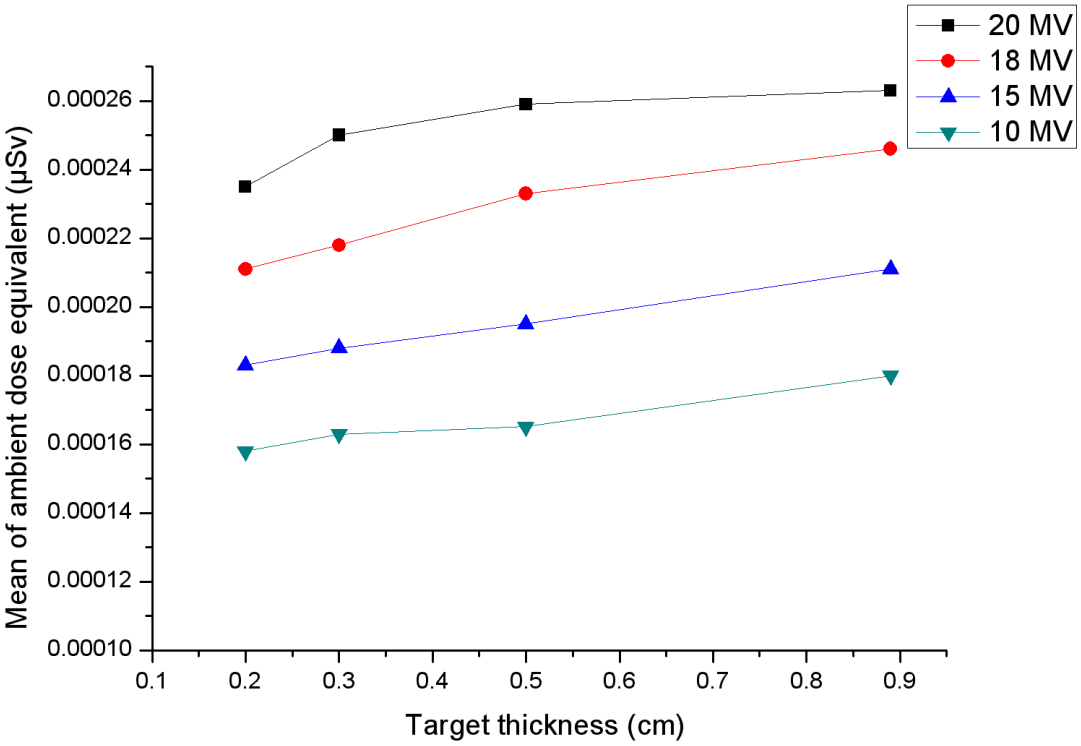

Figure 5.17: Mean of ambient dose equivalent in comparison with different target thickness.

The dose from the contribution of induced activity was calculated and measured using Geant4 simulation and Thermoluminescent dosimeters (TLDs). Where in the case of Geant4 simulation, the estimation of induced activity for RTT was carried out by placing the detector geometry out side the treatment room to the console room. The history files generated separately contain the neutrons number and photons number penetrate the wall of the treatment room. Fulence to dose conversion factors for neutrons (see Fig 5.11) and for photons (see Fig 5.18) was used in calculation of equivalent dose received by RTT.

The contribution from radiation penetrating the walls of the treatment room was also measured with fifteen thermoluminiscence dosimeters (LiF:Mg,Cu,P (GR200A)) placed at the control console of the accelerator over a period of two weeks (10 working days). The contribution from naturally occurring background radiation was measured using ten dosimeters placed in a room far away from the treatment room. This assumes that the radiation transmitted through the walls measured at the control console is representative of the absorbed dose which the technologist receive outside the treatment room during the treatment of the patient. Table 5.9 show the results of normalized photon flunence to the maximum. The results of TLDs of $(D_{tr})_p$, for wall made from concrete with thickness of 112 cm, was found to be 0.179 $\pm$ 13.12 % μSv/h. While the results calculated by Geant4 present 0.0875 $\pm$ 6.02 % μSv/h and 4.166E-06 μSv/h for $(D_{tr})_n$.

The calculation of effective dose for RTT inside the treatment room and in the console control room was performed using the fluence to effective dose conversion coefficients. Fig 5.18 show the fluence to effective dose conversion coefficients for photon energies [81].

Table 5.9: Results of normalized photon flunence to the maximum.

Photon energy (MeV)	Photon fluence (normalize to max)	error (%)
1	0.244	0.084
2	0.7	0.072
3	0.938	0.093
4	1	0.052
5	0.967	0.051
6	0.887	0.061
7	0.801	0.039
8	0.709	0.077
9	0.627	0.082
10	0.549	0.046
11	0.485	0.036
12	0.4305	0.06
13	0.375	0.062
14	0.331	0.081
15	0.292	0.091
16	0.258	0.102
17	0.23	0.096
18	0.202	0.114
19	0.178	0.092
20	0.151	0.136

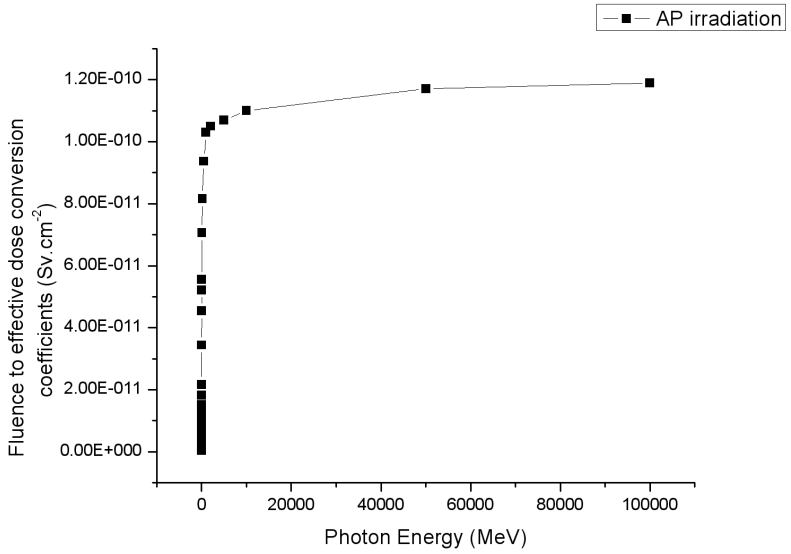

Figure 5.18: Fluence to effective dose conversion coefficients for photon energies.

5.5.9 Verification of Geant4 simulation

The validity of the geometries and ability of Geant4 calculations was been verified after adding water phantom geometry as shown in Fig 5.19 to calculate the percentage depth dose (PDD) for photon with energy of 6 MV. Comparison between the measurements and Geant4 results was shown in Fig 5.20. The measurements was performed using Cylindrical Type Chamber (CC13) and Computerized water phantom (Blue water Phantom). The CC13 is cylindrical chamber consists of inner and outer electrode made of Shonka C552. The chamber has a leakage current less than 4 x 10^{-15}A and chamber sensitivity of 3.8 x 10^{-9} C/Gy for calibration factor (^{60}Co) of 26.01 x 10^{7} Gy/C. The maximum polarising voltage was used is +300 Volt. The Blue water phantom is a measuring device for the measurement and analysis of

the radiation field of medical linear accelerators and is part of the OmniPro-Accept system [82]. It consists of a three-dimensional servo (the Blue Phantom tank with mechanics), a control unit with integrated two-channel electrometer (CU500E), and two single ionization chambers (CC13). The Blue phantom has motors capable to scan in three dimensions and this phantom has dimensions 48 x 48 x 48 cm^3. The phantom material is Acrylic plastic (Perspex) and the weight is 45 kg without water. The accuracy of the position is 0.5 mm per axis. The phantom tank is placed on a trolley for the convenient moving of the assembly and the water is stored in water reservoir. A ligament cap has been used for the final adjustment of the CC13 chamber. The CC13 chamber (reference chamber) was mounted in reference detector holder and the reference detector holder was clamped to the front or rear metal tube of the Blue phantom's aluminum frame. The movement of the CC13 Chamber was controlled by computer using OmniPro-Accept system. The system perform the measurements of PDD and comparison was made for PDD results achieved by Geant4. The results present a good agreement between Geant4 and Blue water phantom, which verify the validity of the geometries and ability of Geant4 calculations.

5.5.10 Methods comparison

The results of comparison between filter paper, portable spectrometer, and mathematical model methods are given in Table 5.10 and show a good agreement. On the other hand, comparison with measurements values using a Bonner sphere system based on passive gold activation detectors published for a Varian Clinac 2100C [85] are given in Table 5.11 for x-ray mode of 18 MV and 10 x 10 cm^2 field sizes. This comparison showed differences greater than factor of 2 and accordingly some indication of reliability definitely need to be given. In order to understand and evaluate

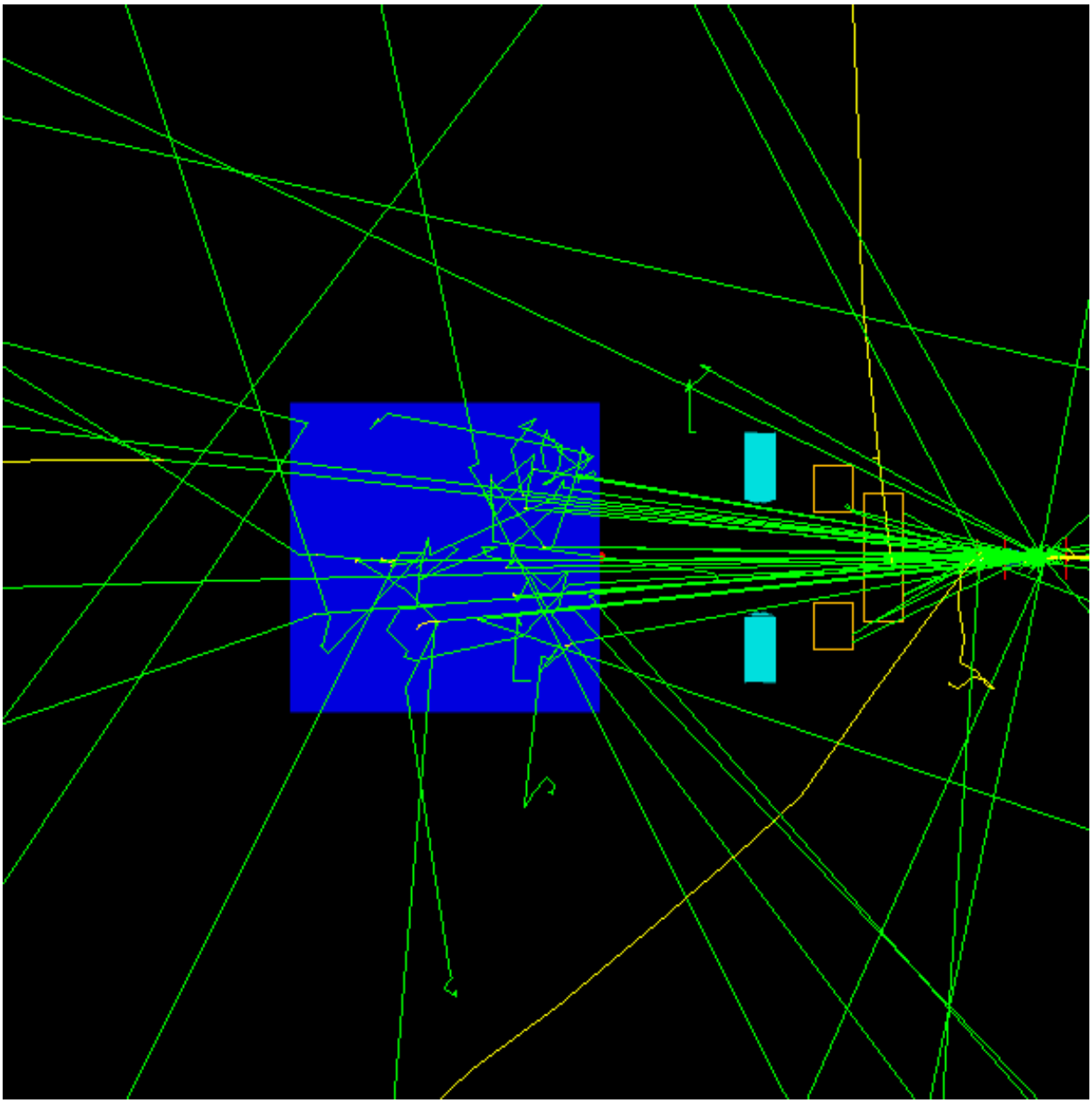

Figure 5.19: Water phantom added to geometries of linear accelerator for purpose of verification Geant4 calculation by percentage depth dose measurements. The green lines present the photon particles interactions and the yellow lines present the electron particles interactions.

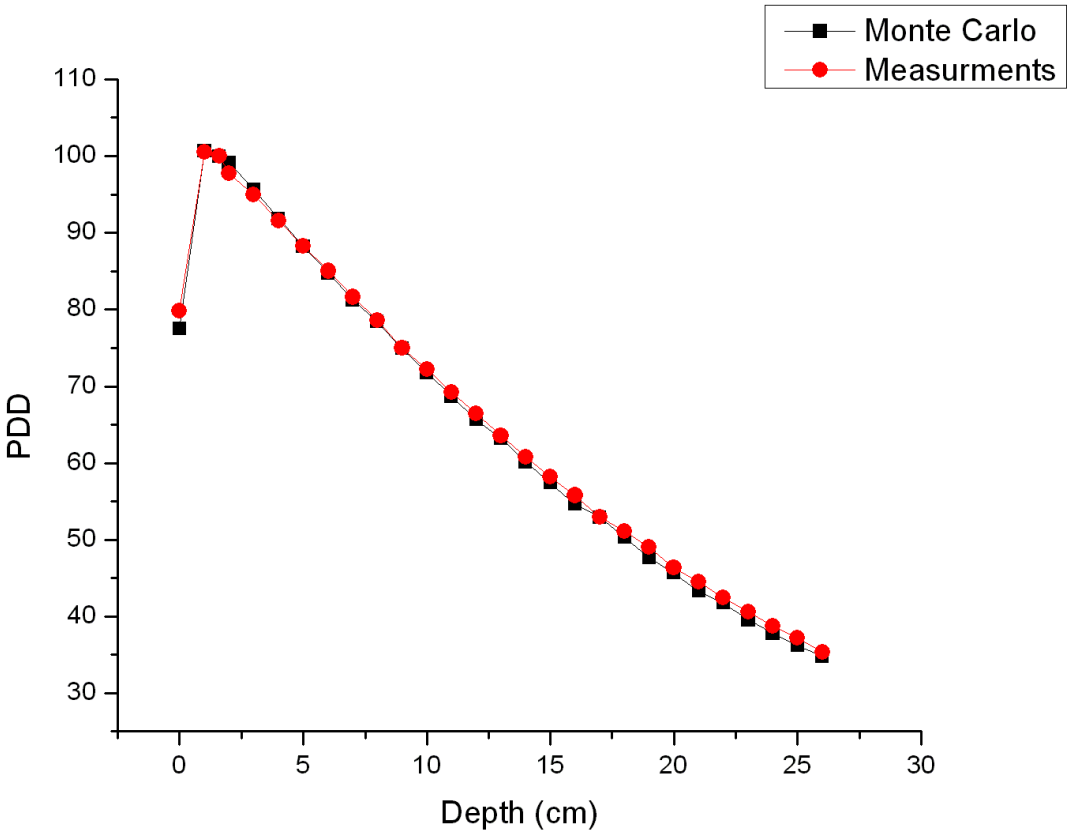

Figure 5.20: Comparison of Monte Carlo and measured results for percentage depth dose (PDD).

these results it must be noted that the radiation field causing photoneutrons production at electron accelerator is very complex and therefore, the difference showed in this comparison are of complex nature. The quality of measurement results is influenced by the errors in the measurement and uncertainty witch was estimated by authors to be in range of 10-20%. On the other hand, the statistical uncertainty of the calculated results was usually below 2% except for bins with very few particles where it was below 10% (by 'statistical uncertainty' is meant one standard deviation of all energy depositions in one bin), however the basic geometrical components of Monte Carlo simulation shown in Fig. 4.13, wasn't include the head shielding and bending magnet. The exact details of the material around the target could change the calculated neutron fluence at the isocenter. Comparing two geometries, one with complete head geometry and the other without head shielding and bending magnet changed the neutron fluence by a factor of 1.8 when scored at the isocenter. Tacking this factor into account the agreement between measured and calculated results of ambient dose equivalent can be considered to be acceptable.

Table 5.10: Comparison of the results for different three methods for 15 MV and decay time of 12 min.

	Filter paper	Portable spectrometer	Mathematical model
Dose rate (μSv/h)	0.72	0.82	0.79

Table 5.11: Comparison of neutron fluence, ϕ, and ambient dose equivalent, H$*$(10), for field sizes 10 x 10 cm^2 for 18 MV.

Author	ϕ ($cm^{-2}.Gy^{-1}$)	H$*$(10) ($mSv.Gy^{-1}$)
This work	1.4 x 10^7	4.4
Fernández *et al* [85]	3.3 x 10^7	6.0

Chapter 6

Conclusion and Recommendations

6.1 Conclusion

This work aims at presenting a study using filter paper, portable spectrometry, mathematical model and Monte Carlo simulation of a linac System (Varian Clinac 2100C) for estimation of the equivalent dose for the patients who undergo radiotherapy treatment and for radiotherapy technologist (RTT). From the results presented in chapter five, conclusion in the following paragraphs can be drawn.

The annual dose received by RTT was found to range between 0.6 to 1.96 mSv, which represents very low dose according to the exposure limits recommended by International Commission on Radiological Protection (ICRP) and International Atomic Energy Agency (IAEA) [3, 83]. On the other hand, one cannot ignore the dose for other workers such as medical engineers dealing with linear accelerator for maintenance purpose.

The total measurement error Δ was found to be ± 6.02 % calculated according to the following equation:

$$\Delta = \sqrt{e^2 + \sigma^2} \tag{6.1}$$

where, e^2 is the systematic error (produced by instrument errors in the experiment of portable spectrometry) and σ^2 is the random error.

The instrument uncertainty e for the portable spectrometry is known to be 4 %; however, the random error σ^2 is difficult to assess because of the varying signals of the induced activity and varying effects of the residual induced activity that results from previous radiation exposures. The estimation of the random error σ^2 was performed by measuring a specific decay curve several times under reference conditions (radiation dose given: 1000 MU; point of interest was isocenter). The average value of these random errors was determined to be 4.5 %. Therefore, the total error Δ is estimated as follows:

$$\Delta = \sqrt{0.04^2 + 0.045^2} = 0.0602 = 6.02\%$$

More than one method was carried out to estimate the dose for RTT and patients. The accuracy of selecting these methods is affected by the following: (a) Setting the electrons particle momentum direction, position, and number to be generated in geant4 and calibration of 1 cGy per 1 MU as mentioned in section 5.5.3. (b) Consideration of chosen five radionuclides to represent all the radionuclides; using the curve-fitting method; and the assumption that the background activation level is constant can affect the accuracy of mathematical model as mentioned in section 5.4. (c) The delay caused by filtration process time (10 min) in filter papers method and the additional time of removing the sample of filter paper from linear accelerator room to the spectrometry can affect the dose and present very low dose rate.

In this study, the theory of Cohen [5] was verified by Monte Carlo simulation

(Geant4 code) using three types of target materials. No comparison was made between our results and Cohen results but in general this study showed that if target thickness exceeds the range of the incident ions and that the irradiation period greatly exceeds the half-life of the radionuclide of interest.

The deviation in radiotherapy from the planned total dose of patient is more than 25 % [84]. This limit applies both to overdoses and underdoses, even though underdoses are often easier to correct. The neutron dose equivalent, greater than 5 mSv Gy^{-1} for 20 MV in the isocenter, can represent a risk for healthy tissues and contribute to secondary malignancy insurgence. Neutron field evaluation is therefore necessary to optimize the treatment, and this new method, consisting of Monte Carlo simulation, can represent a reliable tool.

One of the objectives of this study was to make comparison between induced activity produced by different linear accelerators. The goal of this objective is to answer the question "which type of medical accelerator is useful to be used for safety protection". The estimation of answer was performed using Geant4 by studying the effect of different target materials. Relatively, this estimation was not enough but can give the reader simple idea for selection of the type of linear accelerator according to the type of target.

6.2 Comments and recommendations

In future, further work can be carried out for the determination of the dose received by other workers dealing with medical linear accelerators, such as medical engineers and medical physicists.

Some of isotopes detected have short half-life decay with one to three minutes, so

it is recommended to prevent the RTT from entering the treatment room before three minutes of beam-off after using above of 10 MV in the treatment of x-ray mode.

Medical physicists dealing with medical linear accelerators for purpose of daily mechanical check, MU check, or for acceptance test and commissioning should be aware by using personal detectors and also it is recommended to prevent from entering the treatment room before three minutes of beam-off, when using the above conditions.

Very short half-life nuclides or pure beta-emitter nuclides were not involved in this study, and in the future work can be carried out for the determination of the dose received from these nuclides.

APPENDIX A

ACTIVATION DOSE RATE FORMULA

The activation dose rate formula was derived as follows:

If the nuclear reaction is designated as follows:

$$P \longrightarrow T \longrightarrow G$$

the irradiation period time ,t_i, followed by a decay period denoted by t_c, "a period of time that begins at $t = t_i$ and ends at $t = t_i + t_c$" then the number of density of atoms ,$n(t)$, of radionuclides at time t can written as following:

$$\frac{dn(t)}{dt} = -\lambda n(t) + N\sigma\phi \tag{.2}$$

then,

$$\frac{dn(t)}{dt} + \lambda n(t) = N\sigma\phi \tag{.3}$$

By multiplying both sides of equation (.3) by $e^{\lambda t}$

$$\frac{dn(t)}{dt}e^{\lambda t} + \lambda n(t)e^{\lambda t} = N\sigma\phi e^{\lambda t} \tag{.4}$$

then,

$$\frac{d(n(t)e^{\lambda t})}{dt} = N\sigma\phi e^{\lambda t} \tag{.5}$$

By integrating equation (.5) ,

$$n(t)e^{\lambda t} = \frac{N\sigma\phi}{\lambda}e^{\lambda t} + c \tag{.6}$$

at $t = 0$, $n(t) = 0$ then,

$$c = -\frac{N\sigma\phi}{\lambda}$$

$$\therefore n(t)e^{\lambda t} = \frac{N\sigma\phi}{\lambda}e^{\lambda t} - \frac{N\sigma\phi}{\lambda} \tag{.7}$$

By multiply equation (.7) by $e^{-\lambda t}$,

$$n(t) = \frac{N\sigma\phi}{\lambda}(1 - e^{-\lambda t}) \tag{.8}$$

The specific activity $a(t_i) = \lambda n(t_i)$, for $t = t_i$. Then equation (.8) can be written as follows:

$$a(t_i) = N\sigma\phi(1 - e^{-\lambda t_i}) \tag{.9}$$

After the irradiation has ended ($t > t_i$) the specific activity as a function of the t_c will decay exponentially and be given by activation equation:

$$a(t_c) = a(t_i)e^{-\lambda t_c}$$

$$= a_s(1 - e^{-\lambda t_i})e^{-\lambda t_c} \tag{.10}$$

where , $a_s = N\sigma\phi$.

Similar to equation (.9) one can express the activation dose rate as follows:

$$\dot{D}_c = \dot{D}_m(1 - e^{-\lambda t_r})e^{-\lambda t}$$

where $\dot{D}_m$ is the maximum dose rate, $\dot{D}_c$ is the activation dose rate, t_r is the activation time and t is the decay time.

APPENDIX B

APPLICATION DIAGRAMS

The following classes were defined in the present application:

- DetectorConstruction (volume and material definitions)
- PrimaryGeneratorAction (primary electron generation)
- SteppingAction (step information handling/energy scoring)

The structure of the program is illustrated in the diagrams in Fig B.1 and B.2.

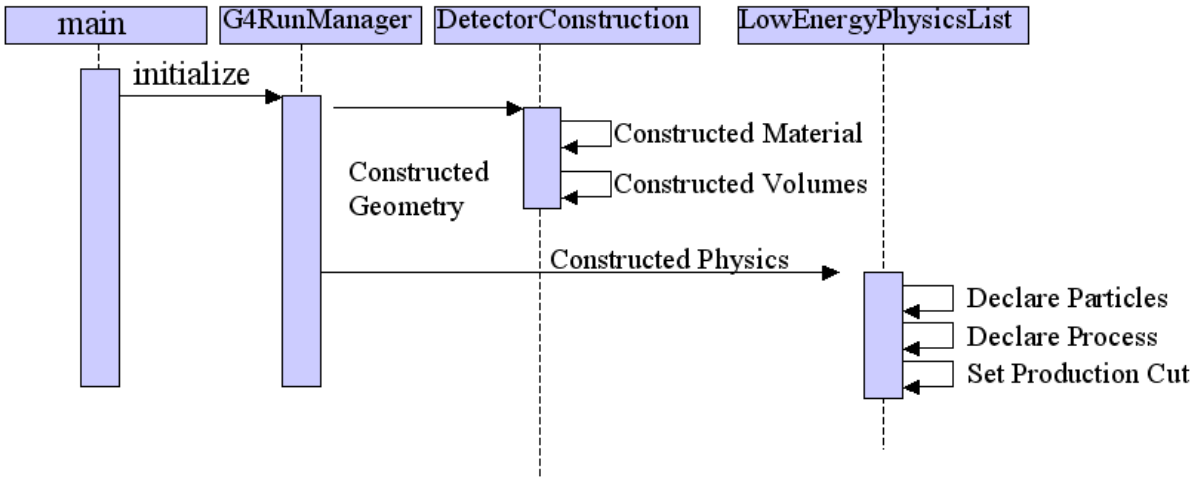

Figure B.1: Initialization of the run.

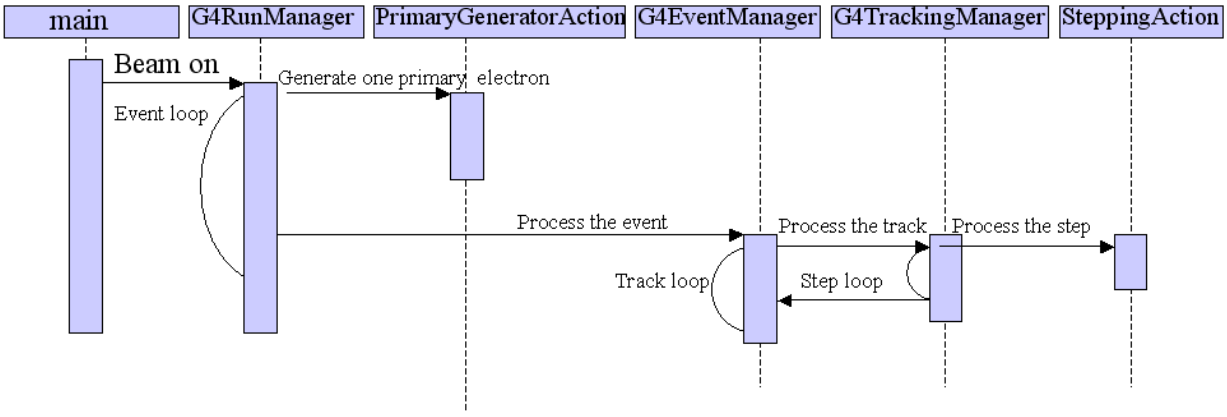

Figure B.2: How the run proceeds. The energy depositions are saved in histograms in the SteppingAction class.

Bibliography

[1] Radiological Training for Accelerator Facilities, Instructor's Guide, Coordinated and Conducted for Office of Environment, Safety and Health, U.S. Department of Energy, http://www.eh.doe.gov/techstds/standard /hdbk1108/hdbk11082002.pdf (2002)

[2] Barbier, M "Induced Radioactivity," Elsevier Ccience, New York (1969).

[3] IAEA, "Radiological Safety Aspect of the Operation of Electron Linear Accelerators," Technical Reports Series No. IAEA-**188**, International Atomic Energy Agency, Vienna, Austria (1979).

[4] Swanson, W.P. and Thomas, R.H. "Dosimetry for radiological protection at high-energy particle accelerators." The Dosimetry of Ionization Radiation, Volume **111**, Kase, K.R., Bjarngard, B. and Attix, F.H., Eds. , Academic Press, New York , 1-161 (1990).

[5] Cohen, B.L. "Nuclear cross sections." CRC Handbook of Radiation Measurement and Protection, Section A: Volume **1**. Physical Science and Engineering Data, Brodsky, A.,Ed. ,CRC Press, Inc., Boca Raton, Florida , 91 - 212 (1978).

[6] ICRP, Recommendations of the International Commission on Radiological Protection, ICRP Publication 26, Annals of ICRP **1**, International Commission on Radiological Protection, Elsevier Science, New York (1977).

[7] ICRP, Recommendations of the International Commission on Radiological Protection, ICRP Publication 60, Annals of ICRP **21**, International Commission on Radiological Protection, Elsevier Science, New York (1991).

[8] NCRP, Limitation to Exposure to Ionization Radiation, NCRP Report No. **116**, National Council on Radiation Protection and Measurements, Bethesda, Maryland (1993).

[9] NCRP, Radiation Protection for Particle Accelerator Facilities, Report No. **144**, National Council on Radiation Protection and Measurements,132-145, (2003).

[10] Bennet, D.J. and Thomson, J.R. "The element of nuclear power", Third edition, Longman Scientific and Technical, New York (1989).

[11] Agostinelli, S., Allison, J., Amako, K., Apostolakis, J., Araujo, H., Arce, P., Asai, M., Axen, D., Banerjee, S., Barrand, G., Behner, F., Bellagamba, L., Boudreau, J., Broglia, L., Brunengo, A., Burkhardt, H., Chauvie, S., Chuma, J., Chytracek, R., Cooperman, G., Cosmo, G., Degtyarenko, P., DellAcqua, A., Depaola, G., Dietrich, D., Enami, R., Feliciello, A., Ferguson, C., Fesefeldt, H., Folger, G., Foppiano, F., Forti, A., Garelli, S., Giani, S., Giannitrapani, R., Gibin, D, Gomez Cadenas, J.J., Gonzalez, I., Gracia Abril, G., Greeniaus, G., Greiner, W., Grichine, V., Grossheim, A., Guatelli, S., Gumplinger, P., Hamatsu, R., Hashimoto, K., Hasui, H., Heikkinen, A., Howard, A., Ivanchenko, V., Johnson, A., Jones, F.W., Kallenbach, J., Kanaya, N., Kawabata, M., Kawabata, Y., Kawaguti, M., Kelner, S., Kent, P., Kimura, A., Kodama, T., Kokoulin, R., Kossov, M., Kurashige, H., Lamanna, E., Lampen, T., Lara, V., Lefebure, V., Lei, F., Liendl, M., Lockman, W., Longo, F., Magni, S., Maire, M., Medernach, E., Minamimoto, K., Mora de Freitas, P., Morita, Y., Murakami, K., Nagamatu, M., Nartallo, R., Nieminen, P., Nishimura, T., Ohtsubo, K., Okamura,

M., ONeale, S. , Oohata, Y., Paech, K., Perl, J., Pfeiffer, A., Pia, M.G., Ranjard, F., Rybin, A., Sadilov, S., Di Salvo, E., Santin, G., Sasaki, T., Savvas, N., Sawada, Y., Scherer, S., Sei, S., Sirotenko, V., Smith, D., Starkov, N., Stoecker, H., Sulkimo, J., Takahata, M., Tanaka, S., Tcherniaev, E., Safai Tehrani, E., Tropeano, M., Truscott, P., Uno, H., Urban, L., Urban, P., Verderi, M., Walkden, A., Wander, W., Weber, H., Wellisch, J.P., Wenaus, T., Williams, D.C., Wright, D., Yamada, T., Yoshida, H., Zschiesche D. "Geant4 - a simulation toolkit", *Nucl. Instr. and Meth. Phys. Res.* A **506**, 3, 250-303 (2003).

[12] Alan Rawlinson, J., Mohammed, K., Galbraith, D.M. "Dose to radiation therapists from activation at high-energy accelerators used for conventional and intensity-modulated radiation therapy" *Med. Phys.* **29**, 598-608 (2002).

[13] Wang, Y.Z., Evans, M.D.C., Podgorsak, E.B. "Characteristics of induced activity from medical linear accelerators," *Med. Phys.* **32**, 2899-2910 (2005).

[14] Greene, D. "Linear accelerators for radiation therapy," Medical physics handbooks **17**, Adam Hilger Ltd Techno House, England, P1-17 (1986).

[15] Martin, J.E. "Physics for radiation protection," John Wiley and Sons, Inc., USA, 145-188 (2000).

[16] Podgorsak, E.B."Review of Radiation Oncology Physics: A Handbook for Teachers and Students," , International Atomic Energy Agency (IAEA), VIENNA, AUSTRIA, 14-125 (2003).

[17] Cossairt, J.D. "Topics in radiation at accelerators: Radiation physics for personnel and environment protection,", Fermi National Accelerator Laboratory, Batavia, US, 1-5 (1996).

[18] Beaulieu, L., Archambault, L., Carrier, J.F., Castrovillari, F., Chauvie, S., Foppiano, F., Ghiso, G., Guatelli, S., Incerti, S., Lamanna, E., Larsson, S.,

Lopes, M.C., Peralta, L., Pia, M.G., Rodrigues, P., Tremblay, V.H., Trindade, A. Overview of Geant4 applications in medical physics, Proceedings of IEEE-NSS, Portland, (2003).

[19] Stranden, E. "Activity Induced in X-ray Therapy Patients by High Energy" *Phys. Med. Biol.* **22**, 348-352 (1977).

[20] Ahlgren, L., and Olsson, L.E. "Induced activity in a high-energy linear accelerator" *Phys. Med. Biol.* **33**, 351-354 (1988).

[21] Loi, G., Dominietto, M., Cannillo, B., Ciocca, M., Krengli, M., Mones, E., Negri, E., Brambilla, M. "Neutron production from a mobile linear accelerator operating in electron mode for intraoperative radiation therapy" *Phys. Med. Biol.* **51**, 695-702 (2006).

[22] AlmCn, A., Ahlgren, L., Mattsson, S. "Absorbed dose to technicians due to induced activity in linear accelerators for radiation therapy" *Phys. Med. Biol.* **36**, 815-822 (1991).

[23] Traneus, E., private communication (2007).

[24] Geant4 physics reference manual, http://geant4.web.cern.ch/geant4/G4UsersDocuments/UsersGuides/PhysicsReferenceManual/html/PhysicsReferenceManual.html (2004).

[25] Perrin, B., Walker, A., Mackay, R. "A model to calculate the induced dose rate around an 18 MV ELEKTA linear accelerator" *Phys. Med. Biol.* **48**, N75-N81 (2003).

[26] Powell, N.L., Newing, A., Bullen, M.A., Sims, C., Leaton, S.F. "A radiation safety survey on a Clinac-20 linear accelerator" *Phys. Med. Biol.* **32**, 707-718 (1987).

[27] LaRiviere, P.D. "Radiotherapy technologist dose from high-energy medical accelerators" *Health Phys.* **49**, 1105-1114 (1985).

[28] O'Brien, P., Michaels, H.B., Gillies, B., Aldrich, J.E., Andrew, J.W. "Radiation protection aspects of a new high-energy linear accelerator" *Med. Phys.* **12**, 101-107 (1985).

[29] NCRP Report No. **79**, "Neutron Contamination from Medical Accelerators," National Council on Radiation Protection and Measurements, Washington, DC, (1984).

[30] McGinley, P.H., Wright, B.A., Meding, C.J. "Dose to radiotherapy technologist from air activation" *Med. Phys.* **11**, 855-858 (1984).

[31] McGinley, P.H. "Shielding Techniques for Radiation Oncology Facilities," expanded 2nd ed., Medical Physics Publishing, Madison, WI, (2002).

[32] McGinley, P.H. and White, Jr.T.A., "Air activation produced by high-energy medical accelerators" *Med. Phys.* **10**, 796-800 (1983).

[33] Garnica-Garza, H.M. "Characteristics of the photoneutron contamination present in a high-energy radiotherapy treatment room" *Phys. Med. Biol.* **50**, 531-539 (2005).

[34] McGinley, P.H. and Landry, J.C. "Neutron contamination of x-ray beams produced by the Varian Clinac 1800" P*hys. Med. Biol.* **34**, 777-783 (1989).

[35] Kliauga, P. and Amols, H. "Photoneutrons from high-energy medical linear accelerators: measurement of the spectrum and dose using a miniature proportional counter" *Int. J. Radiat. Oncol. Biol. Phys.* **31**, 629-33 (1995).

[36] Agosteoa, S., Magistrisb, M., Silarib, M. "Radiological considerations on multi-MW targets. Part I: Induced radioactivity" *Nucl. Instrum. Methods. Phys. Res.* **545**, 813-822 (2005).

[37] Cossairt, J.D. "Topics in radiation at accelerators: Radiation physics for personnel and environment protection" Fermilab report Tm-1‘4, Fermi National Accelerator Laboratory, Batavia, US, 206-219 (2005).

[38] Thomas R.H. and Stevenson, G.R. "Radiological safety aspects of the operation of proton accelerators" IAEA Technical Report No. **283**, International Atomic Energy Comission, Vienna (1988).

[39] Swanson, W.P. and Thomas, R.H. "Dosimetry for radiological protection at high energy particle accelerators" Chapter 1 in the dosimetry of ionizing radiation, Volume **III**, Kase, K.R., Bjrngard, B.E. and Attix, F.H., editors, Academic Press (1990).

[40] Patterson, H.W. and Thomas, R.H. "Accelerator health physics" Academic Press, New York (1973).

[41] Schopper, H., Fass, A., Goebel, K., Hfert, M., Ranft, J., Stevenson, L.G. "nuclear and particle physics" Volume **II**: Shielding against high energy radiation, O. Madelung, Editor in Chief, Springer-Verlag, Berlin, Heidelberg (1990).

[42] Swanson, W.P. "Improved calculation of photoneutron yields released by incident electrons" *Health Phys.* **37**, 347-335 (1979).

[43] LAnnunziata, M.F. "Birth of a unique parent-daughter relation: secular equilibrium" *J. Chem. Educ.* **48**, 700703 (1971).

[44] Rutherford, E., and Soddy, F. "The cause and nature of radioactivity" *Philos. Mag.* **4**, 370396 (1902).

[45] L'Annunziata, M.F. "Radioactivity: Introduction and history" First edition, Montague Group, USA, ELSEVIR, 539-544 (2007).

[46] L'Annunziata, M.F. "Handbook of radioactivity analysis" Second Edition, Montague Group, USA, ELSEVIR (2003).

[47] Knoll G.F. "Radiation Detection and Measurments" John Wiley and Sons, Inc., Third Edition, chapter 12 (2000).

[48] Oneline Rad Pro Calculator. http://www.radprocalculator.com/Gamma.aspx. Ionactive Consulting Ltd , UK (2000).

[49] Fischer, H.W., Peick, K. "Activation Products in a Medical Linear Accelerator" *Radiotherapy and Oncology* **51**:230 (1999).

[50] Roig, M., Panettieri, V., Ginjaume, M., Sanchez-Reyes, A. "Photonuclear isotope characterization of a Siemens KDS 18 MV linac head" *Phys. Med. Biol.* **49**, N243 N246 (2004).

[51] Unger, L. M. and Trubey, D.K. "Specific Gamma-Ray Dose Constants for Nuclides Important to Dosimetry and Radioloical Assessment" OAK Ridge National Laboratory (1982).

[52] Ferrari, A. and Pelliccioni, M. "Conversion coefficients from fluence to ambient dose equivalent, Fluence to dose equivalent conversion data and effective quality factors for high energy neutrons" *Radiation Protection Dosimetry* **76** (4) 215-224 (1998).

[53] Skaggs, L.S., Almy, G.M., Kerst, D.W. and Lanzl, L.H. "Removal of the electron beam from the Betatron" *Phys. Rev.* **70**, 95 (1946).

[54] Adams, G.D, Almy, G.M., Dancoff, S.M., Hanson, A.O., Kerst, D.W., Koch, H.W., Lanzl, E.F., Lanzl, L.H., Laughlin, J.S., Quastler, H., Riesen, D.E., Robinson, C.S., and Skaggs, L.S. " Techniques for the application of Betatron to medical therapy" *Am. J. Roentgenol. Radium Ther.* **60**, 2, 153 (1948).

[55] Chauvie, S., Grichine, V., Gumplinger, P., Ivanchenko, V., Kokoulin, R., Magni, S., Maire, M., Nieminen, P., Pia, M.G., Rybin, A., Urban, L. Geant4 electromagnetic physics, INFN/AE-00/07 (2000).

[56] Chauvie, S., Guatelli, S., Ivanchenko, V., Longo, F., Mantero, A., Mascialino, B., Nieminen, P., Pandola, L., Parlati, S., Peralta, L., Pia, M.G., Piergentili, M., Rodrigues, P., Saliceti, S., Tnndade, A. Geant4 low energy electromagnetic physics, Proceedings of CHEP2001, Beijing, (2001).

[57] Amako, K., Guatelli, S., Ivanchencko, V., Maire, M., Mascialino, B., Murakami, K., Pandola, L., Parlati, S., Pia, M.G., Piergentili, M., Sasaki, T., Urban, L. Validation of Geant4 electromagnetic physics versus protocol data, Proceedings of IEEE-NSS, Rome, (2004).

[58] Cirrone, G.A.P., Cuttone, G., Donadio, S., Grichine, V., Guatclli, S., Gumplinger, P., Ivanchenko, V., Maire, M., Mantero, A., Mascialino, B., Nieminen, P., Pandola, L., Parlati, S., Pfeiffer, A., Pia, M.G., Urban, L. Precision validation of Geant4 electromagnetic physics, Proceedings of IEEE-NSS, Portland, (2003).

[59] Klein, O. and Nishina, Y. *Z. Phys.* **52** 853 (1929).

[60] Hubbell, J.H. and Overbo, I. "Relativistic Atom Form Factors and Photon Coherent Scattering Cross Sections" *J.Phys.Chem.* **8** 69 (1979).

[61] Cullen, D.E. "A simple model of photon transport" *Nucl. Instr. Meth. in Phys. Res. B* **101** 499-510 (1995).

[62] Stepanek, J. "New Photon, Positron and Electron Interaction Data for Geant in Energy Range from 1 eV to 10 TeV", Draft SLAC-265, UC-32 (1985).

[63] Biggs, F. and Lighthill, R. Preprint Sandia Laboratory, SAND 87-0070 (1990).

[64] Grichine, V.M., Kostin, A.P., Kotelnikov, S.K., Pandola, L., Parlati, S., Pia, M.G., Piergentili, M. Bulletin of the Lebedev Institute no. 2-3, **34** (1994).

[65] Gavrila, M. "Relativistic K-Shell Photoeffect" *Phys.Rev.* **113** 514 (1959).

[66] Tuli, J. "Evaluated Nuclear Structure Data File" BNL-NCS-51655-Rev87 (1987).

[67] Molire, G.Z. "Theorie der Streuung schneller geladener Teilchen. II. Mehrfach- und Vielfachstreuung" *Z. Naturforsch.* **3a** 78 (1948).

[68] Lewis, H.W. "Multiple Scattering in an Infinite Medium" *Phys. Rev.* **78** 526 (1950).

[69] Goudsmit, S. and Saunderson, J.L. "Multiple Scattering of Electrons " *Phys. Rev.* **57** 24 (1940).

[70] Lewis, H.W. "Multiple scattering in an infinite medium" *Phys. Rev.* **78** 526 (1950).

[71] Evaluated Photon Data Library (EPDL), http://www.llnl.gov/cullen1/photon.htm, UCRL-50400, Vol.6, Rev.5, (1997).

[72] Evaluated Electron Data Library (EEDL), http://www.llnl.gov/cullen1/electron.htm, UCRL-ID-117796 (1994).

[73] Evaluated Atomic Data Library (EADL), http://www.llnl.gov/cullen1/atomic.htm, UCRL-ID-110438, (1992).

[74] Apostolakis, J., Giani, S., Maire, M., Nieminen, P., Pia, M.G., Urban, L. Geant4 low energy electromagnetic models for electrons and photons, CERN-OPEN-99-034 and INFN/AE-99/18, (1999).

[75] Tsai, Y.S. "Pair production and bremsstrahlung of charged leptons" *Rev. Mod. Phys.* **46** 815 (1974).

[76] IAEA, Absorbed Dose Determination in External Beam Radiotherapy: An International Code of Practice for Dosimetry based on Standards of Absorbed Dose to Water, International Atomic Energy Agency, Technical Report Series no. 398, Vienna (2003).

[77] IAEA, Absorbed Dose Determination in Photon and Electron Beams: An International Code of Practice, International Atomic Energy Agency, Technical Report Series no. 277, second edittion, Vienna (1997).

[78] X-Ray mass attenuation coefficients http://physics.nist.gov/PhysRefData/XrayMassCoef/Co
(1996).

[79] Hubbell, J.H. "Photon Mass Attenuation and Energy-Absorption Coefficients from 1 keV to 20 MeV" *Int. J. Appl. Radiat. Isot.* **33** 1269-1290 (1982).

[80] Hubbell, J.H. and Seltzer, S.M. Ionizing Radiation Division, Physics Laboratory National Institute of Standards and Technology Gaithersburg, MD 20899, U.S (1996).

[81] Pelliccioni, M. "Overview of Fluence-to-Effective Dose and Fluence-to-Ambient Dose Equivalent Conversion Coefficients for High Energy Radiation Calculated Using the FLUKA Code" *Radiat. Prot. Dosim.* **88**(4) 279-297 (2000).

[82] OmniPro-Accept Ver. 6.1 Manual, Scanditronix Wellhofer, www.scanditronix-wellhofer.com, Schwarzenbruck, Germany, P117-119 (2002).

[83] IAEA, International basic safety standards for protection against ionizing radiation and for the safety of radiation sources. International Atomic Energy Agency, Safety Series No. **115**, IAEA, Vienna (1996).

[84] http://www.stuk.fi/saannosto/ST2-1e.html (2003).

[85] Fernández, F., Domingo, C., Amgarou, K., Castelo, J., Bouassoule, T., Garcia, M.J. and Luguera, E. "Neutrons measurements in A Varian 2100C Linac facility using a Bonner sphere system based on passive gold activation detectors" *Radiat. Prot. Dosim* **126** 361-365 (2007)